



---

# Towards Autonomous Navigation in Endovascular Interventions

---

**Author** Tudor Jianu  
**Submitted** May 5<sup>th</sup> 2025

**Supervisors** Dr. Anh Nguyen<sup>1</sup>  
Dr. Sebastiano Fichera<sup>2</sup>  
Dr. Pierre Berthet-Rayne<sup>3</sup>

<sup>1</sup>Department of Computer Science, University of Liverpool, UK.

<sup>2</sup>Department of Mechanical and Aerospace Engineering, University of Liverpool, UK.

<sup>3</sup>Caranx Medical, Research and Development, FR.

A thesis submitted in fulfilment of the requirements for the degree of *Philosophiae Doctor*

Department of Computer Science,  
University of Liverpool

Department of Computer Science,  
University of Liverpool,  
Brownlow Hill,  
Liverpool,  
L69 7ZX

Tudor Jianu © 2025

*“We are what we repeatedly do. Excellence, then, is not an act, but a habit.”*

---

Will Durant – The Story of Philosophy

---

*I dedicate this thesis to everyone I have ever met, whether for a fleeting moment or a lifetime. Each encounter, no matter how brief, has left a mark on me. I am grateful for the lessons, the memories, and the shared experiences that have shaped who I am today.*

*You have all contributed to my journey, and I carry a part of you with me as I continue to grow. Thank you for inspiring me to become the best version of myself. I hope we keep learning from one another, and that our paths cross again in meaningful ways.*

*This is for all of you. Thank you for being part of my life.*

---

# Declaration

I hereby declare that the research work presented in this Thesis is entirely my own and that it has not been submitted, in whole or in part, for any other academic degree or qualification. I further declare that this Thesis has been submitted solely for the purpose of obtaining the PhD degree.

In each chapter of this Thesis, all published papers and articles that have contributed to the work are properly referenced and linked. Similarly, any illustrations created by me and used in previous versions of this work are appropriately linked and credited.

The formatting of this document was initially based on a template by Rob Robinson [1].

---

# Acknowledgements

This PhD journey has been one of the most challenging yet rewarding experiences of my life, and I could not have completed it without the support, guidance, and encouragement of many incredible people.

First and foremost, I would like to express my deepest gratitude to my primary supervisor, Dr. Anh Nguyen. Your support, patience, and insightful advice have been instrumental in shaping this research and in helping me grow as a researcher. Your encouragement and belief in my abilities sustained me through both the highs and lows of this journey.

I am also deeply grateful to my second supervisor, Dr. Sebastiano Fichera, and my third supervisor, Dr. Pierre Berthet-Rayne. Sebastiano, your invaluable feedback and technical expertise have greatly enriched this work. Pierre, your guidance and steady support have been both reassuring and motivating. I feel truly fortunate to have had such a brilliant and supportive supervisory team.

My sincere thanks also go to the University of Liverpool for providing an excellent academic environment, and to the Engineering and Physical Sciences Research Council (EPSRC) for funding this research. Without which this work would not have been possible.

To my friends, near and far: thank you for being there – celebrating milestones, offering encouragement, and providing welcome distractions when they were needed most. Your friendship has been a constant source of strength.

Finally, to my family, especially to my mom. Your love, sacrifices, and steadfast belief in me have been the foundation of everything I've achieved. I could not have done this without you.

---

# Abstract

*Cardiovascular Diseases (CVDs) remain the leading cause of global mortality, with minimally invasive treatment options offered through endovascular interventions. However, the precision and adaptability of current robotic systems for endovascular navigation are impeded by constraints such as heuristic control, limited autonomy, and the absence of haptic feedback. In this thesis, an integrated AI-driven framework is presented to enable autonomous guidewire navigation within complex vascular environments, addressing critical limitations in data availability, simulation fidelity, and navigational accuracy.*

*A high-fidelity, real-time simulation platform, CathSim, is introduced for Reinforcement Learning (RL)-based catheter navigation, featuring anatomically accurate vascular models and contact dynamics. To leverage the multimodal data generated by CathSim, the Expert Navigation Network is developed—an RL-based policy integrating visual, kinematic, and force feedback for autonomous tool control. To address data scarcity, an open-source, bi-planar fluoroscopic dataset, Guide3D, is proposed, comprising over 8,700 annotated images for 3D guidewire reconstruction. Finally, a transformer-based model, SplineFormer, is proposed, which directly predicts guidewire geometry as continuous B-spline parameters, enabling interpretable, real-time navigation.*

*The findings demonstrate that the integration of high-fidelity simulation, multimodal sensory fusion, and geometric modelling significantly enhances autonomous endovascular navigation. CathSim proves effective for training RL algorithms with realistic interactions, while the Expert Navigation Network shows superior performance in complex anatomical structures. Guide3D successfully addresses data scarcity challenges, and SplineFormer achieves high-precision guidewire prediction with improved interpretability. These contributions establish a comprehensive foundation for advancing autonomous endovascular interventions, offering a pathway toward safer and more precise minimally invasive procedures.*

---

# Contents

|          |                                                         |           |
|----------|---------------------------------------------------------|-----------|
| <b>1</b> | <b>Introduction</b>                                     | <b>14</b> |
| 1.1      | Motivation . . . . .                                    | 15        |
| 1.2      | Thesis Scope and Objectives . . . . .                   | 17        |
| 1.3      | Thesis Contributions . . . . .                          | 19        |
| 1.3.1    | CathSim . . . . .                                       | 20        |
| 1.3.2    | Expert Navigation Network . . . . .                     | 21        |
| 1.3.3    | 3D Reconstruction with stereo X-Ray . . . . .           | 22        |
| 1.3.4    | SplineFormer . . . . .                                  | 23        |
| 1.4      | List of Publications . . . . .                          | 24        |
| 1.5      | Outline . . . . .                                       | 25        |
| <b>2</b> | <b>Background</b>                                       | <b>26</b> |
| 2.1      | Deep Learning Fundamentals . . . . .                    | 27        |
| 2.1.1    | Neural Networks and Learning Representations . . . . .  | 27        |
| 2.1.2    | Perceptron and Multi-Layer Perceptrons (MLPs) . . . . . | 28        |
| 2.1.3    | Convolutional Neural Networks . . . . .                 | 30        |
| 2.1.4    | Sequence Modelling in Deep Learning . . . . .           | 31        |
| 2.1.5    | Backpropagation and Training . . . . .                  | 35        |
| 2.1.6    | Reinforcement Learning Fundamentals . . . . .           | 35        |
| 2.1.7    | Policy Learning in Reinforcement Learning . . . . .     | 38        |
| 2.1.8    | Reinforcement Learning for Robot Control . . . . .      | 41        |
| 2.2      | Applications . . . . .                                  | 44        |
| 2.2.1    | Autonomy in Endovascular Navigation . . . . .           | 44        |
| 2.2.2    | Simulation Environments . . . . .                       | 46        |
| 2.2.3    | Endovascular Tool Segmentation and Tracking . . . . .   | 47        |
| 2.2.4    | 3D Reconstruction . . . . .                             | 49        |
| <b>3</b> | <b>CathSim</b>                                          | <b>51</b> |
| 3.1      | Introduction . . . . .                                  | 52        |
| 3.2      | Related Work . . . . .                                  | 55        |
| 3.3      | The CathSim Simulator . . . . .                         | 57        |
| 3.3.1    | Robot Simulation . . . . .                              | 57        |
| 3.3.2    | Aorta Simulation . . . . .                              | 58        |

|          |                                                                |           |
|----------|----------------------------------------------------------------|-----------|
| 3.3.3    | Catheter Simulation . . . . .                                  | 60        |
| 3.3.4    | Contact Simulation . . . . .                                   | 60        |
| 3.3.5    | Blood Simulation . . . . .                                     | 62        |
| 3.4      | RL for Autonomous Cannulation . . . . .                        | 63        |
| 3.4.1    | Observations . . . . .                                         | 63        |
| 3.4.2    | Actions and Rewards . . . . .                                  | 64        |
| 3.4.3    | Network Architectures . . . . .                                | 64        |
| 3.4.4    | Traditional Path Planning . . . . .                            | 65        |
| 3.5      | Experiments . . . . .                                          | 66        |
| 3.5.1    | CathSim Validation . . . . .                                   | 67        |
| 3.5.2    | Reinforcement Learning Results . . . . .                       | 69        |
| 3.5.3    | Force Analysis . . . . .                                       | 70        |
| 3.5.4    | Quantitative Results . . . . .                                 | 73        |
| 3.5.5    | Rewards Analysis . . . . .                                     | 73        |
| 3.5.6    | CathSim Speed Evaluation . . . . .                             | 75        |
| 3.6      | Discussion and Conclusions . . . . .                           | 76        |
| <b>4</b> | <b>Expert Network for Autonomous Navigation</b>                | <b>77</b> |
| 4.1      | Introduction . . . . .                                         | 78        |
| 4.2      | Related Work . . . . .                                         | 79        |
| 4.3      | Autonomous Navigation with Expert Navigation Network . . . . . | 80        |
| 4.3.1    | Expert Navigation Network . . . . .                            | 80        |
| 4.3.2    | Downstream Tasks . . . . .                                     | 83        |
| 4.4      | Experiments . . . . .                                          | 85        |
| 4.4.1    | Expert Trajectory Analysis . . . . .                           | 85        |
| 4.4.2    | Downstream Task Results . . . . .                              | 89        |
| 4.5      | Conclusion and Discussion . . . . .                            | 91        |
| <b>5</b> | <b>Stereo X-Ray-Based 3D Reconstruction</b>                    | <b>92</b> |
| 5.1      | Introduction . . . . .                                         | 93        |
| 5.2      | Related Works . . . . .                                        | 94        |
| 5.3      | The Guide3D Dataset . . . . .                                  | 97        |
| 5.3.1    | Data Collection Setup . . . . .                                | 97        |
| 5.3.2    | Data Acquisition, Labelling, and Statistics . . . . .          | 98        |
| 5.3.3    | Camera Calibration and Distortion Correction . . . . .         | 98        |
| 5.3.4    | Guidewire Reconstruction . . . . .                             | 99        |
| 5.3.5    | Utility of Gude3D Dataset for the Research Community . . . . . | 101       |
| 5.4      | Guidewire Shape Prediction . . . . .                           | 102       |
| 5.4.1    | Spherical Coordinates Representation . . . . .                 | 102       |

|          |                                                                          |            |
|----------|--------------------------------------------------------------------------|------------|
| 5.4.2    | Network Architecture . . . . .                                           | 103        |
| 5.4.3    | Loss Function . . . . .                                                  | 104        |
| 5.4.4    | Training Details . . . . .                                               | 105        |
| 5.4.5    | Shape Prediction Network . . . . .                                       | 105        |
| 5.5      | Experiments . . . . .                                                    | 107        |
| 5.5.1    | Dataset Validation . . . . .                                             | 107        |
| 5.5.2    | Guidewire Prediction Results . . . . .                                   | 108        |
| 5.5.3    | Segmentation Results . . . . .                                           | 110        |
| 5.6      | Discussion and Conclusion . . . . .                                      | 112        |
| <b>6</b> | <b>SplineFormer</b>                                                      | <b>113</b> |
| 6.1      | Introduction . . . . .                                                   | 114        |
| 6.2      | Related Works . . . . .                                                  | 116        |
| 6.3      | B-Spline Representation for Autonomous Endovascular Navigation . . . . . | 118        |
| 6.3.1    | B-Spline Representation for Guidewire Modelling . . . . .                | 118        |
| 6.3.2    | SplineFormer Network Architecture . . . . .                              | 119        |
| 6.3.3    | Loss Function . . . . .                                                  | 122        |
| 6.3.4    | Policy Training . . . . .                                                | 122        |
| 6.4      | Experiments . . . . .                                                    | 124        |
| 6.4.1    | Endovascular Robot Setup . . . . .                                       | 124        |
| 6.4.2    | Autonomous Navigation Results . . . . .                                  | 125        |
| 6.4.3    | Qualitative Results . . . . .                                            | 128        |
| 6.4.4    | Attention Visualization . . . . .                                        | 128        |
| 6.4.5    | Discussion . . . . .                                                     | 129        |
| 6.4.6    | Limitations . . . . .                                                    | 129        |
| 6.5      | Conclusions . . . . .                                                    | 131        |
| <b>7</b> | <b>Conclusions</b>                                                       | <b>132</b> |
| 7.1      | Summary . . . . .                                                        | 133        |
| 7.2      | Future Work . . . . .                                                    | 135        |
| 7.3      | Final Reflections . . . . .                                              | 137        |
|          | <b>References</b>                                                        | <b>138</b> |

---

# List of Figures

|      |                                                  |    |
|------|--------------------------------------------------|----|
| 1.1  | An overview of CathSim . . . . .                 | 20 |
| 1.2  | Expert Navigation Network . . . . .              | 21 |
| 1.3  | Imitation Learning Network . . . . .             | 21 |
| 1.4  | Guidewire Shape Predictions . . . . .            | 22 |
| 1.5  | B-Spline Guidewire Representation . . . . .      | 23 |
| 2.1  | LSTM Cell . . . . .                              | 32 |
| 2.2  | GRU Cell . . . . .                               | 33 |
| 2.3  | Transformer Architecture . . . . .               | 34 |
| 3.1  | CathSim Overview . . . . .                       | 53 |
| 3.2  | CathBot . . . . .                                | 57 |
| 3.3  | CathBot Follower . . . . .                       | 58 |
| 3.4  | Aortic Collision Properties . . . . .            | 59 |
| 3.5  | Aortic Models. . . . .                           | 59 |
| 3.6  | Catheter Properties . . . . .                    | 61 |
| 3.7  | Blood Flow Simulation . . . . .                  | 61 |
| 3.8  | Path Planning . . . . .                          | 65 |
| 3.9  | Experiment Starting Configuration . . . . .      | 66 |
| 3.10 | Experimental setup of CathBot . . . . .          | 67 |
| 3.11 | Simulated and Real Force Comparison . . . . .    | 69 |
| 3.12 | Force Heatmaps . . . . .                         | 70 |
| 3.13 | Force Distribution . . . . .                     | 71 |
| 3.14 | Training Rewards Plots . . . . .                 | 74 |
| 3.15 | CathSim training speed. . . . .                  | 75 |
| 4.1  | The Expert Navigation Network. . . . .           | 80 |
| 4.2  | Downstream IL Network. . . . .                   | 80 |
| 4.3  | Episode Length Distributions . . . . .           | 85 |
| 4.4  | Experiment Setup . . . . .                       | 85 |
| 4.5  | Navigation Paths Comparison . . . . .            | 86 |
| 5.1  | Dataset Composition Materials . . . . .          | 97 |
| 5.2  | Undistortion and Calibration Procedure . . . . . | 99 |

---

|     |                                                   |     |
|-----|---------------------------------------------------|-----|
| 5.3 | Point Matching Process . . . . .                  | 101 |
| 5.4 | Network Key Components . . . . .                  | 103 |
| 5.5 | Guidewire Reconstruction Error Analysis . . . . . | 107 |
| 5.6 | Guidewire Shape Prediction Comparison . . . . .   | 108 |
| 5.7 | Guidewire Shape Predictions . . . . .             | 109 |
| 5.8 | Reprojection Visualization . . . . .              | 110 |
| 5.9 | Segmentation Examples . . . . .                   | 111 |
| 6.1 | System Overview . . . . .                         | 115 |
| 6.2 | Segmentation Failure Cases . . . . .              | 116 |
| 6.3 | B-Spline Guidewire Representation . . . . .       | 118 |
| 6.4 | SplineFormer Network Architecture . . . . .       | 119 |
| 6.5 | Robot Setup in X-ray Room . . . . .               | 124 |
| 6.6 | Navigation Configuration: . . . . .               | 126 |
| 6.7 | SplineFormer vs. Segmentation . . . . .           | 127 |
| 6.8 | Attention visualization . . . . .                 | 129 |

---

# List of Tables

|     |                                                          |     |
|-----|----------------------------------------------------------|-----|
| 3.1 | Endovascular Simulator Environments Comparison . . . . . | 55  |
| 3.2 | User-study results. . . . .                              | 69  |
| 3.3 | Results Summary . . . . .                                | 72  |
| 3.4 | Comparative training times . . . . .                     | 75  |
| 4.1 | The network architectures for ENN . . . . .              | 82  |
| 4.2 | SAC hyperparameters . . . . .                            | 82  |
| 4.3 | Force prediction results. . . . .                        | 85  |
| 4.4 | Ablation study on input modalities . . . . .             | 86  |
| 4.5 | Imitation Learning Results . . . . .                     | 89  |
| 4.6 | BC Architecture . . . . .                                | 90  |
| 4.7 | BC Hyperparameters . . . . .                             | 90  |
| 5.1 | Endovascular intervention datasets comparison. . . . .   | 95  |
| 5.2 | Dataset Composition Overview. . . . .                    | 98  |
| 5.3 | Shape Comparison . . . . .                               | 108 |
| 5.4 | Segmentation Results. . . . .                            | 108 |
| 6.1 | Endovascular navigation results. . . . .                 | 126 |



## Chapter 1

---

# Introduction

[Cardiovascular Diseases \(CVDs\)](#) remain one of the foremost global health challenges, accounting for a substantial proportion of morbidity and mortality worldwide. Over the past few decades, significant advancements in medical technology and minimally invasive interventions have transformed the clinical landscape, offering improved patient outcomes through endovascular procedures. Nevertheless, despite their clinical efficacy, these interventions continue to present substantial procedural risks, technical challenges, and operational burdens on healthcare providers.

In this thesis, the integration of [Artificial Intelligence \(AI\)](#) into robotic systems is investigated to enhance the precision and autonomy of endovascular interventions. The focus is placed on the development of advanced learning frameworks, high-fidelity simulation environments, and robust modelling techniques that collectively aim to address the persistent challenges of autonomous endovascular tool navigation. By employing cutting-edge methods such as [Reinforcement Learning \(RL\)](#), multimodal sensory integration, and geometric modelling, efforts are directed toward advancing the frontiers of autonomous endovascular robotics, with implications extending beyond navigation to broader domains within surgical robotics and interventional medicine.

The remainder of this chapter is structured as follows. In [Section 1.1](#), the motivation behind pursuing autonomy in endovascular procedures is discussed, highlighting both the clinical significance and current limitations of existing robotic systems. In [Section 1.2](#), the scope and objectives of this thesis are outlined, framing the research questions that guide its contributions. [Section 1.3](#) provides a summary of the key technical innovations and datasets developed throughout this work. Finally, the chapter is concluded with a detailed outline of the thesis organization in [Section 1.5](#).

## 1.1 Motivation

Cardiovascular Diseases (CVDs) are the leading cause of mortality worldwide, impacting millions each year. Conditions like coronary heart disease and cerebrovascular disease are among the most significant contributors to CV-related deaths [2]. Treatment options for these diseases have evolved significantly, with minimally invasive endovascular interventions, such as Percutaneous Coronary Intervention (PCI), Pulmonary Vein Isolation (PVI), and Mechanical Thrombectomy (MT), now forming critical components of care [3, 4, 5]. These procedures allow vascular obstructions or arrhythmias to be treated by navigating *catheters* and *guidewires* from an access point, such as the *femoral artery* or *radial artery*, to specific targets within the vascular system, typically under fluoroscopic guidance [6]. Once the target is reached, interventions like thrombus removal, stent deployment, or tissue ablation can be performed.

However, despite their efficacy, these procedures are associated with risks and complications. Fluoroscopy use, for instance, results in exposure of both patients and healthcare practitioners to ionizing radiation, with cumulative exposure increasing the risk of adverse health effects, including cancer [7]. Furthermore, repeated use of contrast dye during imaging has been associated with nephrotoxicity, particularly in vulnerable patients [8]. From a procedural standpoint, complications such as vessel perforation, thrombosis, or distal embolization continue to present challenges, especially in acute cases where timely and precise intervention is critical [9]. Time remains particularly crucial in stroke interventions, as the benefits of procedures like MT diminish significantly if not performed promptly [10].

In recent years, robotic assistance has been introduced in endovascular procedures to address some of these challenges. The potential of robotics to improve precision, reduce operator fatigue, and lower radiation exposure has been demonstrated by enabling procedures to be controlled from a safer distance [11, 12]. Systems such as the Magellan<sup>TM</sup> and CorPath GRX<sup>®</sup> have shown promise in procedures like PCI and PVI, offering enhanced control and stability for catheter navigation [13, 14]. By eliminating the need for operators to be positioned directly next to patients, robotic systems also reduce reliance on heavy protective lead aprons, which are known to contribute to orthopaedic issues over time for medical staff [15].

Nevertheless, limitations are present in current robotic systems. A *leader-follower* setup is typically employed, in which complete control over the robot's movements is retained by the physician, resulting in *high cognitive demands* and the potential for human error [16]. Additionally, most robotic systems lack haptic feedback, which is critical for enabling the interaction between the catheter and vessel walls to be felt, thereby making navigation more challenging [17]. The interfaces of these systems often rely on input devices (*i.e.*, joysticks or buttons), requiring a skill set distinct from traditional clinical practices and potentially

slowing the adoption of robotic technology in endovascular settings.

To address these limitations, there is growing interest in integrating **AI** with robotic systems to achieve greater autonomy in endovascular tool navigation. **AI**, particularly through **Machine Learning (ML)** and **RL**, has shown promise in enhancing *decision-making*, *data analysis*, and *pattern recognition* in various healthcare applications [18, 19]. **RL**, which enables agents to learn optimal actions through interactions with the environment, is especially relevant for autonomous navigation tasks where the system can adapt through a process similar to human *trial-and-error* learning [20, 21]. In the context of endovascular procedures, **AI**-driven autonomous systems could reduce operator dependence, enhance navigation precision, and ultimately expand the accessibility and safety of these critical interventions.

While **AI**-driven autonomy holds great promise for endovascular tool navigation, the field faces significant challenges due to the limited availability of high-quality data and suitable simulation environments. **ML** algorithms, particularly those used for tasks like segmentation and object recognition, depend heavily on large, annotated datasets to capture the variability in vascular anatomy and pathological states. However, in the medical domain, such datasets are scarce, creating a bottleneck for algorithmic development. In **RL**, which requires extensive sampling to learn optimal navigation strategies, the need for realistic and responsive simulation environments is paramount. Simulation platforms such as SOFA [22], commonly used in medical contexts, are not fully optimized for **RL**, as they lack the flexibility and efficiency necessary for high-throughput sampling and training. This gap underscores the dependency of **RL** on specialized simulation tools that can accurately model the dynamics of catheter interactions within complex vascular structures. These limitations in both data availability for **ML** and suitable simulation environments for **RL** present critical challenges in developing robust, autonomous navigation systems. Bridging these gaps is essential to advancing algorithmic precision and adaptability in autonomous endovascular interventions.

Given these advancements and challenges, this thesis aims to advance autonomous catheter navigation by exploring and developing **AI**-driven methods that improve the precision, adaptability, and overall performance of robotic systems in complex vascular environments. By addressing existing limitations in navigation accuracy, and procedural safety, this work contributes to the foundation for future innovations in minimally invasive, autonomous endovascular procedures.

## 1.2 Thesis Scope and Objectives

The limitations in autonomous catheter navigation primarily arise from heuristic-driven controls, which restrict adaptability in complex vascular conditions, and from RL’s data dependency in endovascular settings. The primary goal of this thesis is to establish a robust, simulation-based framework that allows RL models to train efficiently, achieving real-time, accurate navigation within complex vascular structures.

This thesis proposes a new approach to autonomous endovascular navigation, leveraging high-fidelity simulation, multimodal sensory integration, and advanced geometric modelling. By creating a modular simulation environment, this work improves data accessibility, diversifies sensory inputs, and enables precise navigation. These contributions bridge the gap between simulation and clinical application, promoting safer and more effective minimally invasive procedures.

The following research questions guide this thesis:

- How can high-fidelity simulation environments improve RL training for endovascular navigation and its subproblems?
- In what ways can multimodal sensory integration enhance navigation accuracy and reduce reliance on manual control?
- How can shape inference assist navigation?
- How can advanced geometric modelling improve the robustness and interpretability of guidewire navigation across various imaging conditions?

To address these questions, this thesis pursues several key objectives:

1. Review and analyse existing methods: Conduct an in-depth literature review on autonomous catheter navigation, RL in medical applications, and high-fidelity simulation, identifying current limitations and opportunities.
2. Develop a real-time simulation environment: Create the CathSim simulator, supporting RL training with realistic vascular models, a follower robot, and accurate catheter dynamics.
3. Design a multimodal learning framework: Develop the [Expert Navigation Network \(ENN\)](#) within CathSim, integrating additional sensory inputs, such as force feedback and shape representations, to support efficient learning and real-world applicability.
4. Create a high-resolution endovascular dataset: Develop Guide3D, an open-source dataset for segmentation and 3D reconstruction tasks, addressing data limitations in endovascular imaging and supporting algorithm development.

5. Implement a transformer-based navigation model: Introduce SplineFormer, a B-spline transformer model for real-time prediction of guidewire geometry, enhancing interpretability and enabling navigation across diverse imaging conditions.

Through these contributions, this thesis aims to advance autonomous catheter navigation via high-fidelity simulation, integrated sensory feedback, and refined geometric modelling. Though focused on endovascular navigation, the methods developed here hold promise for broader applications in surgical robotics and other minimally invasive procedures where precision and adaptability are essential.

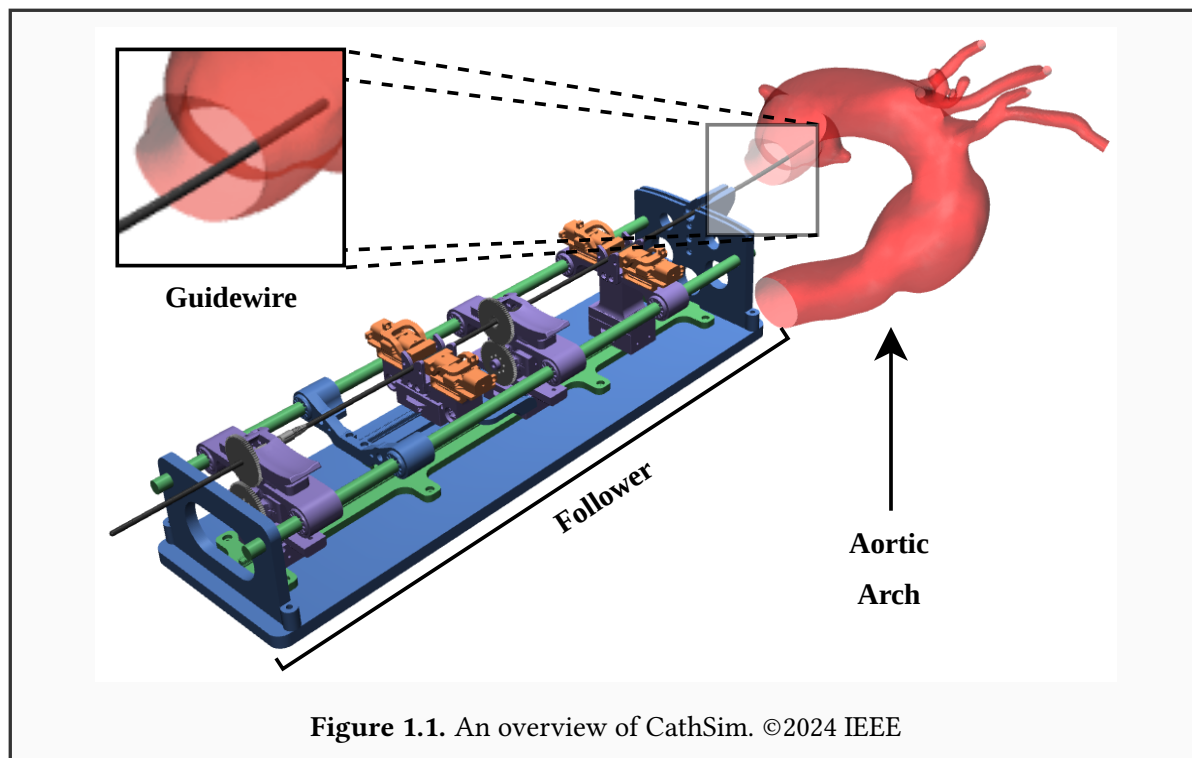
## 1.3 Thesis Contributions

Existing approaches to autonomous catheter navigation often rely on heuristic-driven controls, limiting adaptability to complex vascular environments and leading to suboptimal performance. Additionally, [RL](#) methods require extensive data that is challenging to gather in clinical settings. This thesis addresses these gaps by developing an integrated framework to enhance simulation fidelity, multimodal data availability, and navigational accuracy.

This work introduces CathSim, a real-time simulation environment featuring *anatomically accurate* aortic models and precise contact dynamics, supporting efficient [RL](#) training. Building directly on this simulation infrastructure, the [ENN](#) leverages CathSim-generated multimodal data to enhance navigation precision. To further support algorithm development and validation, Guide3D provides a high-resolution, open-source dataset for segmentation and 3D reconstruction, addressing data scarcity in endovascular imaging. Finally, SplineFormer, a B-spline transformer model that builds upon these foundational contributions, predicts guidewire geometry with high interpretability, enabling robust, real-time navigation across diverse imaging conditions.

Together, these interconnected contributions provide a comprehensive foundation for advancing autonomous endovascular navigation, improving safety, precision, and adaptability in minimally invasive interventions.

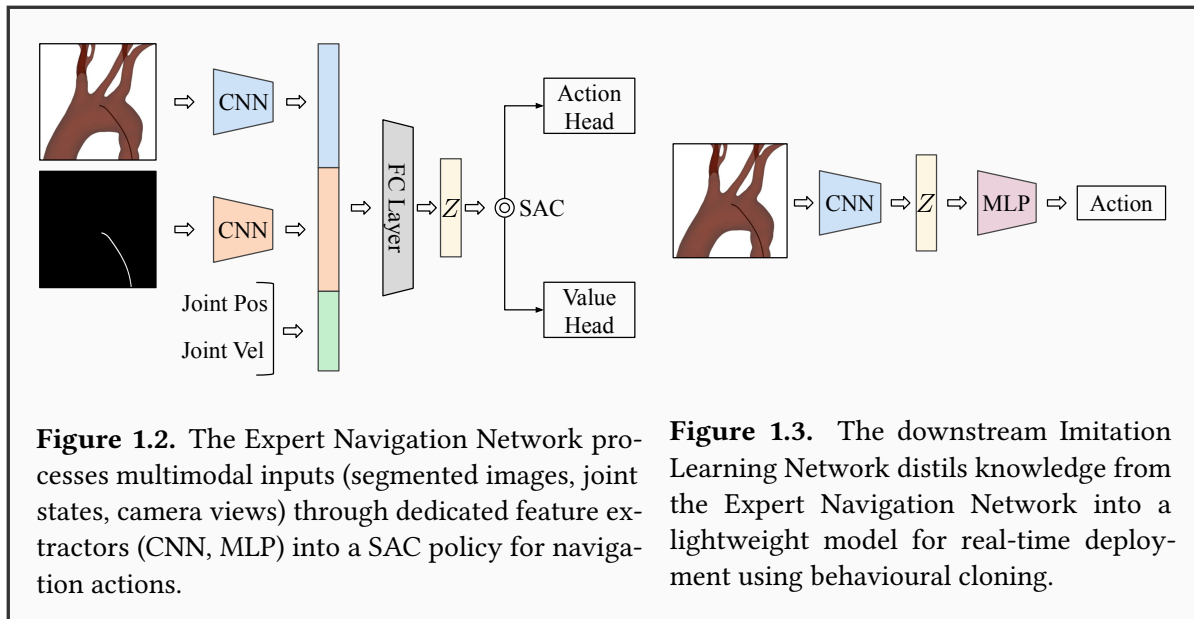
### 1.3.1 CathSim



Existing autonomous catheter navigation solutions predominantly use heuristic-driven controls, which lack adaptability in complex vascular environments, resulting in suboptimal cannulation performance. While RL methods offer potential improvements, they require substantial data for efficacy, and existing simulation environments (e.g., SOFA) prioritize realism over RL integration. To address this gap, *CathSim* is introduced as a high-fidelity simulation environment tailored for real-time interaction and optimized for training advanced learning algorithms. *CathSim* comprises three main components: *i*) a follower robot model, *ii*) anatomically accurate aortic arch phantoms, and *iii*) a catheterguidewire model with realistic curvature dynamics, as illustrated in Fig. 1.1.

MuJoCo's rigid body dynamics [23] are leveraged to calculate contact interactions between the catheter and aortic walls. Each contact point is computed based on spatial coordinates and contact normals, ensuring realistic frictional forces and efficient resolution. This model enables precise force dynamics without complex deformation calculations, providing a streamlined yet high-fidelity simulation environment for advancing autonomous endovascular navigation systems.

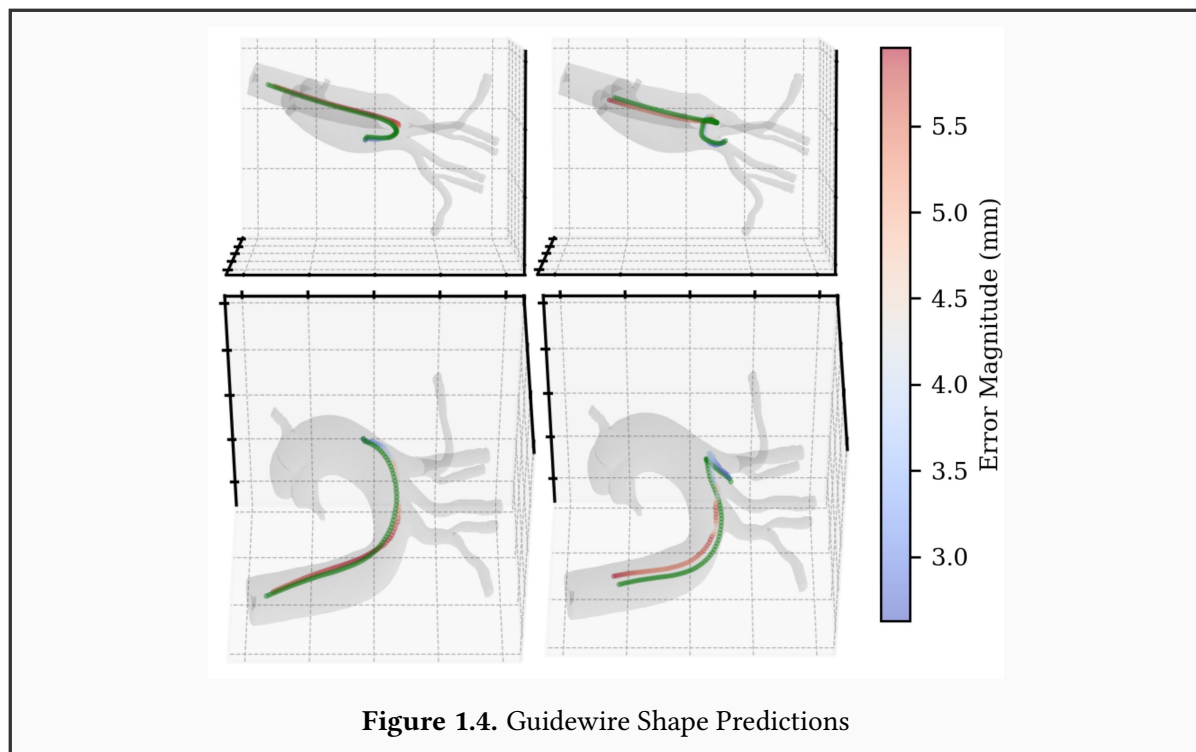
### 1.3.2 Expert Navigation Network



Current endovascular navigation techniques rely primarily on limited real-world sensory inputs, such as X-ray images, which constrain the ability to gather diverse, multimodal data necessary for effective autonomous navigation. To overcome these limitations, the [Expert Navigation Network \(ENN\)](#) is proposed as a multimodal learning framework trained on extensive labelled data generated within the CathSim simulation environment. By leveraging CathSim, the [ENN](#) incorporates additional sensor modalities – such as force feedback and shape representations – that are generally unavailable in clinical settings, thereby enhancing navigation precision and reducing reliance on manual controls.

The [ENN](#) is designed to process multiple input modalities, including guidewire segmentation, joint position, joint velocity, and camera images. Dedicated feature extractors ([Convolutional Neural Networks \(CNNs\)](#) for visual data and an [Multi-Layered Perceptron \(MLP\)](#) for joint data) are used to build a robust navigation representation. The resulting concatenated feature vector is then fed into a [Soft Actor Critic \(SAC\)](#) policy, which maps these combined features to precise navigation actions, as illustrated in Fig. 1.2. To facilitate real-world deployment, the learned policy is distilled into a downstream imitation learning network, shown in Fig. 1.3, which enables efficient execution with reduced computational requirements. Multimodal integration within the [ENN](#) substantially improves autonomous catheterization by enabling precise trajectory planning and effective simulation-to-reality transfer, thereby paving the way for real-time surgical support and fully autonomous catheter navigation.

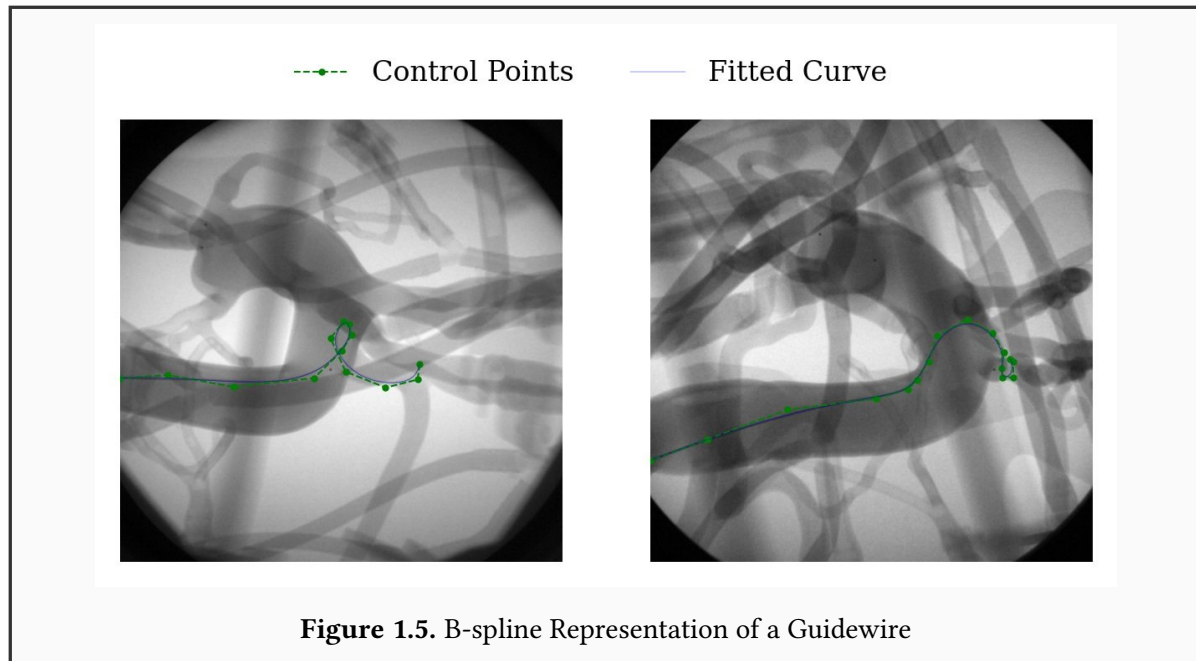
### 1.3.3 3D Reconstruction with stereo X-Ray



Existing endovascular imaging datasets lack the detailed segmentation and 3D reconstruction data essential for developing advanced algorithms, especially in realistic bi-planar configurations. To address this limitation, *Guide3D* is introduced as a high-resolution, open-source dataset tailored for segmentation and 3D reconstruction in endovascular imaging. Figure 1.4 illustrates the 3D representation and predictive capabilities. *Guide3D* contains detailed annotations for two distinct guidewires, offering over 8,700 annotated images across varied flow conditions. By providing bi-planar images, *Guide3D* enables accurate 3D guidewire geometry reconstruction, fulfilling a critical need for reliable benchmarks in the field.

*Guide3D* incorporates a rigorous calibration process with high-fidelity anatomical models and precise X-ray imaging to ensure consistent image quality and anatomically accurate representations. Advanced undistortion and calibration techniques support robust 3D reconstruction via triangulation, enabling thorough algorithm comparisons for both segmentation and dynamic, video-based methods that leverage temporal dimensions for enhanced tracking and analysis. This versatility makes *Guide3D* a vital resource for advancing and benchmarking endovascular imaging algorithms, offering a foundational tool for the research community.

### 1.3.4 SplineFormer



Existing approaches to guidewire navigation often rely on segmentation-based methods, which struggle to accurately model the guidewire’s curvilinear structure, leading to suboptimal navigation accuracy.

To address this challenge, *SplineFormer* is introduced as a B-spline transformer model that directly predicts the guidewire’s shape as a set of continuous B-spline parameters, as illustrated in Figure 1.5. This model provides a compact, interpretable representation that captures the guidewire’s geometry within a constrained parametric space, enhancing both precision and interpretability in endovascular navigation.

Additionally, *SplineFormer* incorporates a dedicated tip predictor module that identifies the guidewire’s starting position, enabling precise, autonomous navigation in real-time applications. By leveraging the guidewire’s inherent curvature, *SplineFormer* achieves robust performance, reducing reliance on segmentation pre-processing. In experimental validation using a high-fidelity vascular phantom equipped with a bi-planar X-ray imaging system and robotic manipulation, *SplineFormer* achieved fully autonomous guidewire control, demonstrating substantial improvements in endovascular navigation tasks. This approach offers a reliable, dimensionally consistent representation that maintains accuracy even in the presence of noise or imaging artefacts, advancing automation and safety in minimally invasive interventions.

## 1.4 List of Publications

The contributions are summarized as following:

- [1] **Jianu, T.**, Huang, B., Nguyen, H., Bhattarai, B., Do, T., Tjiputra, E., Tran, Q., Berthet-Rayne, P., Le, N., Fichera, S., and Nguyen, A., “Guide3d: A bi-planar x-ray dataset for guidewire segmentation and 3d reconstruction,” in *Proceedings of the Asian Conference on Computer Vision (ACCV)*, Code available at: <https://airvlab.github.io/guide3d/>, Dec. 2024, pp. 1549–1565.
- [2] **Jianu, T.**, Huang, B., Vo, T., Vu, M. N., Kang, J., Nguyen, H., Omisore, O., Berthet-Rayne, P., Fichera, S., and Nguyen, A., “Autonomous catheterization with open-source simulator and expert trajectory,” in *Handbook of Robotic and Image-Guided Surgery, 2nd Edition*, Nasab, M. H. A., Ed., 2nd ed., Elsevier, 2025, ISBN: 9780443139123.
- [3] **Jianu, T.**, Huang, B., Vu, M. N., Abdelaziz, M. E., Fichera, S., Lee, C.-Y., Berthet-Rayne, P., Baena, F. R. y, and Nguyen, A., “Cathsim: An open-source simulator for endovascular intervention,” *IEEE Transactions on Medical Robotics and Bionics*, 2024, Code available at: <https://airvlab.github.io/cathsim>.
- [4] **Jianu, T.**, Huang, B., Berthet-Rayne, P., Fichera, S., and Nguyen, A., “3d guidewire shape reconstruction from monoplane fluoroscopic images,” in *International Conference on Robot Intelligence Technology and Applications*, Springer, 2023, pp. 84–94.
- [5] **Jianu, T.**, Huang, B., Nguyen, H., Berthet-Rayne, P., Fichera, S., and Nguyen, A., “Deepwire: Spherical coordinate-based deep learning for accurate guidewire shape reconstruction,” in *Proceedings of the 9th International Conference on Biomedical Signal and Image Processing (ICBIP 2024)*, Suzhou, China, 2024.
- [6] **Jianu, T.**, Doust, S., Li, M., Huang, B., Do, T., Nguyen, H., Bates, K., Ta, T. D., Fichera, S., Berthet-Rayne, P., *et al.*, “Splineformer: An explainable transformer-based approach for autonomous endovascular navigation,” in *International Conference on Intelligent Robots and Systems (IROS) - Under Review*, IEEE, 2025.
- [7] Kang, J., **Jianu, T.**, Huang, B., Bhattarai, B., Le, N., Coenen, F., and Nguyen, A., “Translating simulation images to x-ray images via multi-scale semantic matching,” in *Data Engineering in Medical Imaging*, Bhattarai, B., Ali, S., Rau, A., Caramalau, R., Nguyen, A., Gyawali, P., Namburete, A., and Stoyanov, D., Eds., Cham: Springer Nature Switzerland, 2025, pp. 95–104, ISBN: 978-3-031-73748-0.
- [8] Do, T., Vu, N., **Jianu, T.**, Huang, B., Vu, M., Su, J., Tjiputra, E., Tran, Q. D., Chiu, T.-C., and Nguyen, A., “Fedefm: Federated endovascular foundation model with unseen data,” in *ICRA*, IEEE, 2025.

## 1.5 Outline

The primary focus of this thesis is to advance autonomy in endovascular navigation. The structure of this dissertation is as follows:

- *Chapter 2* presents the technical background underlying this work, focusing on *deep learning*, *reinforcement learning*, and *autonomous robotic* navigation. It introduces key network architectures and control frameworks, reviews existing methods in endovascular navigation and guidewire segmentation, and establishes the context for the contributions developed in this thesis.
- *Chapter 3* presents **CathSim**, a novel simulation environment designed to expedite the development and testing of navigation algorithms. As an open-source tool, CathSim enables rapid algorithmic prototyping and dataset generation, supporting reproducibility and ease of use. This simulation environment serves as a foundational resource for endovascular navigation research.
- *Chapter 4* introduces the **Expert Navigation Network**, which leverages the extensive dataset generated within CathSim to enable precise navigation within complex aortic environments. This network effectively utilizes the internal data from CathSim to replicate expert-level navigation, outperforming traditional methods in accuracy and robustness within simulated aortic pathways.
- *Chapter 5* discusses the development of **Guide3D**, a pioneering open-source dataset specifically designed for guidewire segmentation and 3D reconstruction. Additionally, this chapter presents a guidewire reconstruction method that surpasses existing techniques by providing higher accuracy and reliability in 3D vascular modelling.
- *Chapter 6* introduces **SplineFormer**, a transformer-based network specifically tailored for predicting complex, arbitrary-shaped splines essential for guidewire navigation. SplineFormer is implemented and validated in real-world scenarios, demonstrating substantial improvement in spline prediction accuracy and adaptability over traditional spline modelling approaches.
- *Chapter 7* synthesizes the contributions of this work, summarizing key findings and insights. This chapter also discusses potential future research directions to further enhance autonomous endovascular navigation.

## Chapter 2

---

# Background

Autonomous endovascular navigation, situated at the intersection of medical robotics, [Artificial Intelligence \(AI\)](#), and interventional radiology, addresses the challenge of navigating complex vasculature with minimal human intervention. Achieving full autonomy requires advances in [Deep Learning \(DL\)](#), [Reinforcement Learning \(RL\)](#), computer vision, and robotics.

This chapter presents the core algorithmic foundations that enable autonomous endovascular navigation. It reviews [DL](#) architectures, including [Convolutional Neural Networks \(CNNs\)](#), [Recurrent Neural Networks \(RNNs\)](#), and Transformers, for perception and control, and introduces [Reinforcement Learning \(RL\)](#) as a framework for sequential decision-making under uncertainty. Learning-based approaches to guidewire control, vessel segmentation, and navigation, as well as their integration with robotic systems, are also examined. These foundations support the developments described in subsequent chapters.

## 2.1 Deep Learning Fundamentals

**Deep Learning** has emerged as a paradigm-shifting approach within the domain of **AI**, driving significant advancements across diverse fields, including computer vision, **Natural Language Processing (NLP)**, healthcare, and autonomous systems. Unlike conventional **Machine Learning (ML)** methodologies, which often necessitate extensive feature engineering, **DL** models utilize hierarchically structured **Artificial Neural Networks (ANNs)** to autonomously extract and learn intricate patterns from high-dimensional data [24]. This capability has rendered **DL** particularly effective for complex tasks where traditional statistical and rule-based approaches often exhibit suboptimal performance.

This chapter provides a systematic exposition of the fundamental principles underlying deep learning, focusing on its theoretical foundations, architectural frameworks, and training methodologies. The discussion begins with an examination of **AI**, in which essential components such as perceptrons, activation functions, and the backpropagation algorithm are covered. Subsequently, deep network architectures are analysed, including **CNN**, which have achieved state-of-the-art performance in image analysis; **RNN**, which excel in sequential data processing; and transformer-based models, which have revolutionized natural language understanding and generation [25].

Furthermore, critical aspects of **DL** model optimization are explored, encompassing *gradient-based optimization techniques*, regularization strategies, and *transfer learning paradigms*, all of which play a crucial role in improving model convergence, generalization, and robustness [26]. By the conclusion of this chapter, a comprehensive understanding of **DL**'s foundational principles and methodologies will have been developed, forming a solid basis for subsequent discussions on its practical implementation and advancements.

### 2.1.1 Neural Networks and Learning Representations

**Artificial Neural Networks** are computational models inspired by the structure and function of biological neural networks. These models form the foundation of deep learning by enabling hierarchical feature extraction and representation learning. Neural networks consist of interconnected computational units, known as *neurons*, that process and transform input data through weighted connections and non-linear activation functions. The primary objective of a neural network is to approximate a target function  $f^*(x)$  using training data  $(x, y)$ , where  $y \approx f^*(x)$ . This section provides an overview of fundamental neural network architectures, starting from the perceptron and extending to deep **Multi-Layered Perceptrons (MLPs)**.

## 2.1.2 Perceptron and Multi-Layer Perceptrons (MLPs)

**Perceptron.** The perceptron, introduced by Rosenblatt [27], is the simplest form of an artificial neuron and functions as binary linear classifier. It maps an input vector  $\mathbf{x} = [x_1, x_2, \dots, x_n]$  to an output  $y$  using a weighted sum followed by a threshold function:

$$y = f\left(\sum_{i=1}^n w_i x_i + b\right) = f(\mathbf{w}^T \mathbf{x} + b), \quad (2.1)$$

where:  $\mathbf{x} \in \mathbb{R}^n$  is the input feature vector,  $\mathbf{w} \in \mathbb{R}^n$  represents the weight parameters,  $b$  is the bias term, and  $f(\cdot)$  is a step function:

$$f(z) = \begin{cases} 1, & \text{if } z \geq 0 \\ 0, & \text{otherwise} \end{cases} \quad (2.2)$$

Despite its simplicity, the perceptron is limited to solving only linearly separable problems. The XOR problem, as highlighted by Minsky and Papert [28], is a classic example where a single-layer perceptron fails. This limitation motivated the development of **MLPs** with non-linear activation functions.

**Multi-Layer Perceptron.** An **MLP** extends the perceptron by introducing multiple layers of neurons, allowing the network to learn hierarchical and complex representations. An **MLP** consists of at least three layers:

- Input layer: Receives raw input data  $\mathbf{x}$ .
- Hidden layers: Intermediate layers where neurons apply weighted transformations and activation functions.
- Output layer: Produces the final output  $\hat{y}$ .

The transformation at each neuron in an **MLP** is given by:

$$\mathbf{a}^{(l)} = \sigma(\mathbf{W}^{(l)} \mathbf{a}^{(l-1)} + \mathbf{b}^{(l)}), \quad (2.3)$$

where  $\mathbf{a}^{(l)}$  is the activation vector of layer  $l$ ,  $\mathbf{W}^{(l)}$  is the weight matrix for layer  $l$ ,  $\mathbf{b}^{(l)}$  is the bias vector for layer  $l$ ,  $\sigma(\cdot)$  is a non-linear activation function, and  $l \in \{1, 2, \dots, L\}$  represents the layer index with  $L$  being the total number of layers in the network.

The Universal Approximation Theorem [29], [30] states that an **MLP** with at least one hidden layer and a non-linear activation function can approximate any continuous function, making **MLPs** suitable for classification and regression tasks.

### 2.1.2.1 Activation Functions

Activation functions introduce non-linearity into neural networks, enabling them to model complex decision boundaries. Without non-linearity, an [MLP](#) with multiple layers would reduce to a single-layer linear model. Common activation functions include:

**Sigmoid Activation Function.** The sigmoid function is defined as:

$$\sigma(x) = \frac{1}{1 + e^{-x}}, \quad (2.4)$$

with derivative:

$$\sigma'(x) = \sigma(x)(1 - \sigma(x)) \quad (2.5)$$

Although sigmoid is useful for probabilistic interpretations, it suffers from the vanishing gradient problem, leading to slow convergence in deep networks.

**ReLU Activation Function.** The [Rectified Linear Unit \(ReLU\)](#) function is widely used in deep learning:

$$\text{ReLU}(x) = \max(0, x), \quad (2.6)$$

with derivative:

$$\text{ReLU}'(x) = \begin{cases} 1, & x > 0 \\ 0, & x \leq 0 \end{cases} \quad (2.7)$$

ReLU mitigates the vanishing gradient problem but introduces the dying ReLU problem, where neurons output zero for negative inputs. Variants like [Leaky Rectified Linear Unit \(Leaky ReLU\)](#) and [Parametric Rectified Linear Unit \(PReLU\)](#) address this issue by allowing small gradients for negative inputs.

### 2.1.2.2 Learning Representations in Deep Networks

[Deep Neural Networks \(DNNs\)](#) build hierarchical representations by stacking multiple layers. Each hidden layer captures a more abstract feature representation of the input data. The depth of the model determines its ability to generalize and approximate complex functions. Given a training dataset  $\{(x_i, y_i)\}_{i=1}^N$ , a [DNN](#) approximates the function  $f^*(x)$  such that:

$$y \approx f^*(x) = f(x; \theta, W) = \phi(x; \theta)W, \quad (2.8)$$

where  $\phi(x; \theta)$  represents learned features from input  $x$ ,  $W$  is a mapping from features to output space,  $\theta$  are parameters of the representation function.

The advantage of DL over shallow models lies in the ability to learn hierarchical feature representations rather than relying on manually engineered features [24]. This characteristic enables DNNs to generalize better and achieve state-of-the-art performance across various domains, including computer vision, NLP, and RL.

### 2.1.3 Convolutional Neural Networks

Convolutional Neural Network (CNN) have become the cornerstone of modern deep learning-based image analysis, demonstrating exceptional performance in tasks such as object detection, facial recognition, and medical image processing [31], [32], [33]. Unlike fully connected neural networks, CNNs leverage spatial hierarchies within data by employing convolutional operations, enabling automatic feature extraction without the need for handcrafted descriptors [24], [34]. This architecture consists of three primary components: *convolutional layers*, *non-linearity*, and *pooling*, each of which plays a crucial role in learning hierarchical feature representations [26], [35].

#### 2.1.3.1 Convolution Operation

The core operation in CNNs is the convolution, which applies a set of learnable filters to the input image to extract spatial features. Given an input image  $\mathbf{X} \in \mathbb{R}^{H \times W \times C}$ , where  $H$ ,  $W$ , and  $C$  denote the height, width, and number of channels, respectively, the convolutional operation with a filter  $\mathbf{K} \in \mathbb{R}^{k \times k \times C}$  produces an output feature map  $\mathbf{Y} \in \mathbb{R}^{H' \times W' \times C'}$  given by:

$$Y_{i,j}^{(m)} = \sum_{c=1}^C \sum_{u=1}^k \sum_{v=1}^k X_{i+u,j+v}^{(c)} K_{u,v}^{(c,m)} + b^{(m)}, \quad (2.9)$$

where  $i \in \{1, 2, \dots, H'\}$ ,  $j \in \{1, 2, \dots, W'\}$  represent the spatial indices of the output feature map,  $m \in \{1, 2, \dots, C'\}$  denotes the output channel index,  $H'$  and  $W'$  are the height and width of the output feature map, respectively, and  $C'$  is the number of output channels (filters).

#### 2.1.3.2 Activation Functions

To introduce non-linearity, CNNs employ activation functions such as the ReLU (see Subsec. 2.1.2.1). ReLU prevents vanishing gradient issues observed in sigmoid and tanh activations, facilitating efficient training of deep networks [36], [37]. Alternative activation functions such as Leaky ReLU [38] and Swish [39] have been proposed to further enhance gradient flow and improve feature learning.

#### 2.1.3.3 Pooling Layers

Pooling operations reduce spatial dimensions while preserving critical features, thereby improving computational efficiency and mitigating overfitting [40], [41]. The most commonly

used pooling techniques include max-pooling and average-pooling, defined as:

$$Y_{i,j}^{(m)} = \max_{(u,v) \in R} X_{i+u,j+v}^{(m)}, \quad (2.10)$$

for max-pooling, where  $R$  denotes the pooling region, and

$$Y_{i,j}^{(m)} = \frac{1}{|R|} \sum_{(u,v) \in R} X_{i+u,j+v}^{(m)}, \quad (2.11)$$

for average pooling, where  $|R|$  is the number of elements in the pooling region. These operations contribute to translational invariance in CNNs [42].

### 2.1.3.4 Modern CNNs Architectures

Several advanced CNN architectures have been proposed to enhance feature extraction capabilities. For instance, **Residual Network (ResNet)** introduces residual connections to mitigate the vanishing gradient problem [33], while **Densely Connected Convolutional Network (DenseNet)** employs dense connectivity to promote feature reuse [43]. Additionally, **EfficientNet** utilizes neural architecture search to optimize network depth, width, and resolution [44]. These advancements have significantly improved CNN performance in large-scale image recognition benchmarks such as ImageNet [32], [45].

## 2.1.4 Sequence Modelling in Deep Learning

Sequence modelling plays a fundamental role in DL, enabling the processing and prediction of sequential data across various domains, including speech recognition [46], NLP [47], [48], and time-series forecasting [49]. Unlike conventional **Feed-Forward Networks (FFNs)**, which assume independence between input samples, sequence models incorporate temporal dependencies, allowing for the capture of dynamic patterns within data. This section explores two major paradigms in sequence modelling: **Recurrent Neural Network (RNN)** and their variants – **Long Short-Term Memories (LSTMs)**, **Gated Recurrent Units (GRUs)** – and Transformer-based architectures, which have revolutionized the field with their self-attention mechanism.

### 2.1.4.1 RNNs, LSTMs, and GRUs

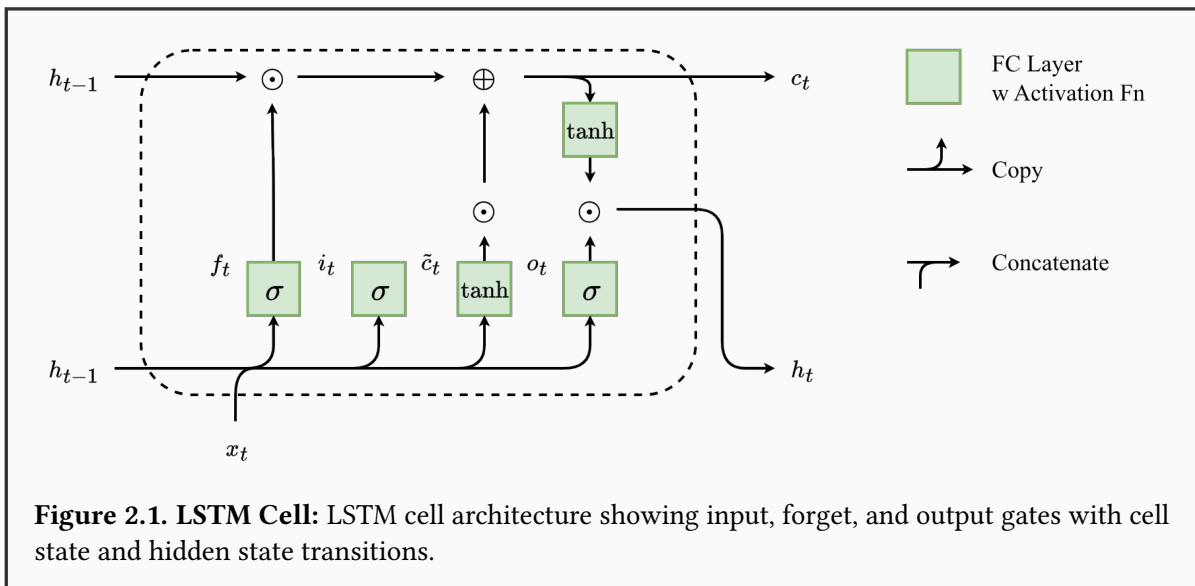
**Recurrent Neural Network (RNN)** extend traditional neural networks by introducing recurrence, allowing them to maintain a hidden state that evolves over time. Given an input sequence  $\mathbf{X} = \{x_1, x_2, \dots, x_T\}$ , an RNN computes the hidden state  $\mathbf{h}_t$  at time step  $t$  using:

$$\mathbf{h}_t = f(\mathbf{W}_h \mathbf{h}_{t-1} + \mathbf{W}_x \mathbf{x}_t + \mathbf{b}), \quad (2.12)$$

where  $\mathbf{W}_h$  and  $\mathbf{W}_x$  are weight matrices,  $\mathbf{b}$  is the bias term, and  $f(\cdot)$  is an activation function, typically  $\tanh$  or ReLU [50]. The output  $\mathbf{y}_t$  at each time step is given by:

$$\mathbf{y}_t = g(\mathbf{W}_y \mathbf{h}_t + \mathbf{b}_y), \tag{2.13}$$

where  $g(\cdot)$  is a task-dependent activation function, such as softmax for classification. While RNNs can model short-term dependencies effectively, they struggle with long-term dependencies due to the vanishing and exploding gradient problems during backpropagation through time [51].



To mitigate these issues, **LSTMs** (LSTM) networks introduce a memory cell that allows for more effective gradient flow across long sequences. As shown in Fig. 2.1, the LSTM cell includes three gating mechanisms – the forget gate  $\mathbf{f}_t$ , input gate  $\mathbf{i}_t$ , and output gate  $\mathbf{o}_t$  – that modulate the cell state  $\mathbf{c}_t$ , enabling the network to retain or discard information as needed. The LSTM dynamics are described by:

$$\mathbf{f}_t = \sigma(\mathbf{W}_f[\mathbf{h}_{t-1}, \mathbf{x}_t] + \mathbf{b}_f), \tag{2.14}$$

$$\mathbf{i}_t = \sigma(\mathbf{W}_i[\mathbf{h}_{t-1}, \mathbf{x}_t] + \mathbf{b}_i), \tag{2.15}$$

$$\mathbf{o}_t = \sigma(\mathbf{W}_o[\mathbf{h}_{t-1}, \mathbf{x}_t] + \mathbf{b}_o), \tag{2.16}$$

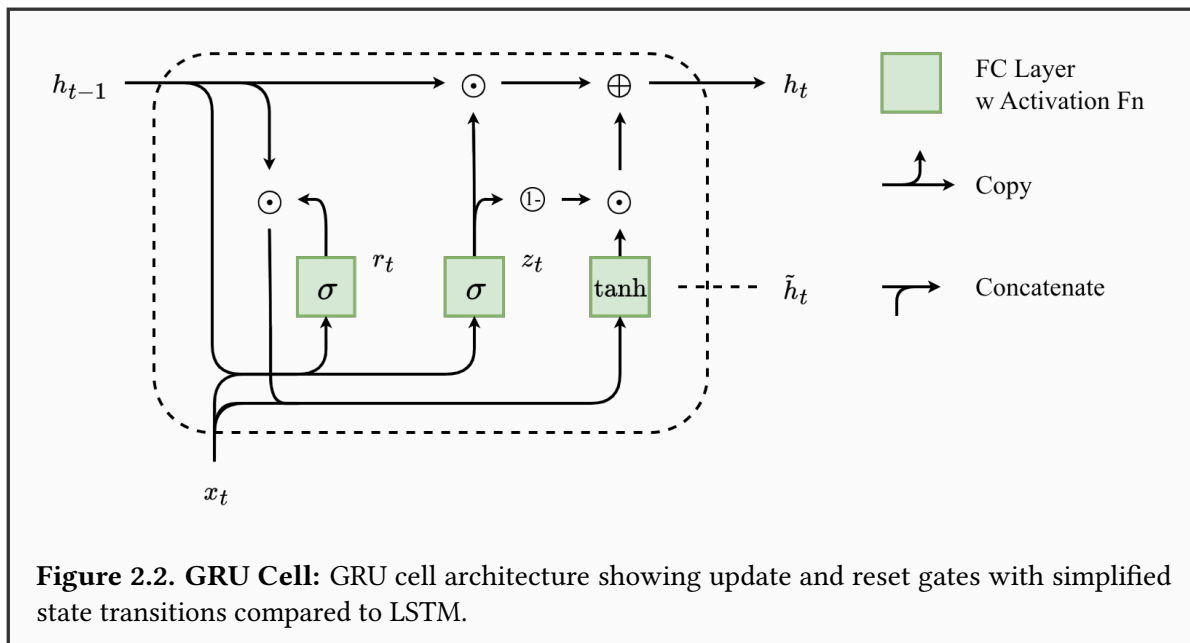
$$\tilde{\mathbf{c}}_t = \tanh(\mathbf{W}_c[\mathbf{h}_{t-1}, \mathbf{x}_t] + \mathbf{b}_c), \tag{2.17}$$

$$\mathbf{c}_t = \mathbf{f}_t \odot \mathbf{c}_{t-1} + \mathbf{i}_t \odot \tilde{\mathbf{c}}_t, \tag{2.18}$$

$$\mathbf{h}_t = \mathbf{o}_t \odot \tanh(\mathbf{c}_t), \tag{2.19}$$

where  $\sigma(\cdot)$  denotes the sigmoid activation, and  $\odot$  represents element-wise multiplication. The

decoupling of memory and output pathways allows LSTMs to learn long-term dependencies more robustly than standard RNNs.



A computationally efficient alternative is the **GRU**, which simplifies the gating structure by combining the forget and input gates into a single update gate  $z_t$ , and using a reset gate  $r_t$  to control the flow of past information. This design reduces the number of parameters while retaining the model's ability to capture long-term dependencies. The GRU cell, depicted in Fig. 2.2, is governed by:

$$z_t = \sigma(\mathbf{W}_z[\mathbf{h}_{t-1}, \mathbf{x}_t] + \mathbf{b}_z), \quad (2.20)$$

$$r_t = \sigma(\mathbf{W}_r[\mathbf{h}_{t-1}, \mathbf{x}_t] + \mathbf{b}_r), \quad (2.21)$$

$$\tilde{\mathbf{h}}_t = \tanh(\mathbf{W}_h[r_t \odot \mathbf{h}_{t-1}, \mathbf{x}_t] + \mathbf{b}_h), \quad (2.22)$$

$$\mathbf{h}_t = (1 - z_t) \odot \mathbf{h}_{t-1} + z_t \odot \tilde{\mathbf{h}}_t. \quad (2.23)$$

By eliminating the separate memory cell, **GRUs** offer faster training and inference times, making them suitable for resource-constrained or real-time applications.

Both **LSTMs** and **GRUs** have demonstrated state-of-the-art performance in sequential tasks such as speech recognition [46], machine translation [49], and time-series analysis, providing a foundation for later advances in self-attention-based models.

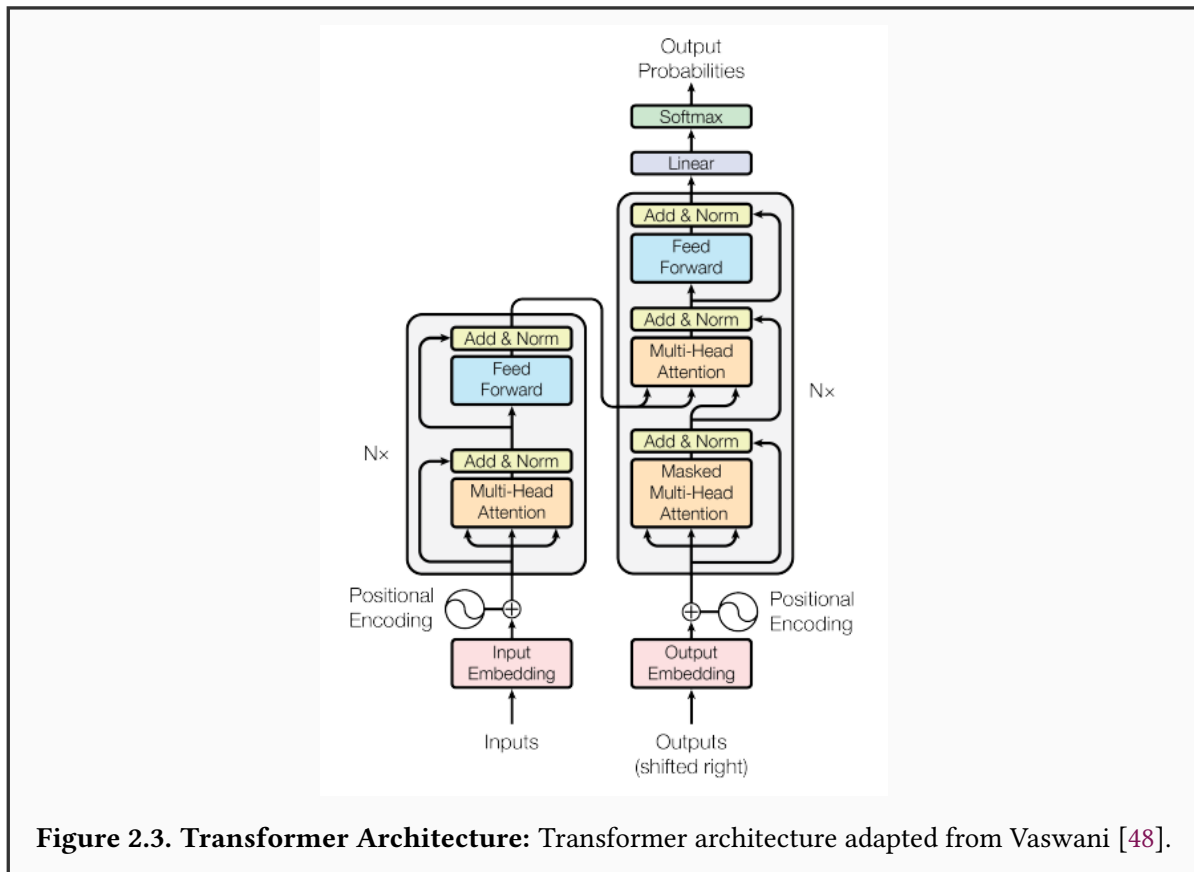


**Figure 2.3. Transformer Architecture:** Transformer architecture adapted from Vaswani [48].

### 2.1.4.2 Transformer Networks and Their Evolution

While RNN-based models have achieved significant success, their sequential nature limits parallelization and scalability. Transformer networks, introduced by Vaswani [48], overcome these limitations by utilizing self-attention mechanisms instead of recurrence. The core operation in a transformer is the scaled dot-product attention:

$$\text{Attention}(\mathbf{Q}, \mathbf{K}, \mathbf{V}) = \text{softmax} \left( \frac{\mathbf{Q}\mathbf{K}^T}{\sqrt{d_k}} \right) \mathbf{V}, \tag{2.24}$$

where  $\mathbf{Q}$ ,  $\mathbf{K}$ , and  $\mathbf{V}$  represent query, key, and value matrices, respectively, and  $d_k$  is the key dimension. This operation enables each token in the input sequence to attend to all other tokens, capturing contextual dependencies regardless of their distance.

The standard transformer architecture (see Figure 2.3) is composed of stacked encoder and decoder layers. Each encoder layer contains two main sub-layers: a Multi-Head Self-Attention (MHA) mechanism and a position-wise fully connected feedforward network, both surrounded by residual connections and layer normalization. The decoder layers include a third sub-layer that performs multi-head attention over the encoder outputs, enabling effective cross-attention. Positional encodings are added to the input embeddings to inject order information, compensating for the model’s lack of recurrence or convolution.

Transformers have evolved through architectures such as [Bidirectional Encoder Representations from Transformers \(BERT\)](#) [52], which uses only the encoder for bidirectional language understanding; [Generative Pre-trained Transformer \(GPT\)](#) [53], which uses only the decoder stack in an autoregressive manner for text generation; and [Vision Transformer \(ViT\)](#) [54], which adapts the encoder for image patches, demonstrating the model's versatility beyond language tasks.

### 2.1.4.3 Application of Transformers in Medical Image Analysis

Transformers have recently been applied to medical imaging, particularly in tasks such as tumour segmentation [55], disease classification [56], and radiology report generation. ViT process medical images as patch embeddings, leveraging self-attention to capture spatial relationships without convolutional operations [54]. Hybrid models, such as Swin Transformers [57], integrate CNN-like hierarchical structures to enhance feature extraction.

Recent studies show that transformer-based models outperform CNNs in various medical imaging benchmarks, highlighting their potential to advance Computer-Aided Diagnosis (CAD) [58]. However, challenges such as data efficiency, high computational cost, and interpretability remain active areas of research.

## 2.1.5 Backpropagation and Training

MLPs and CNNs are trained using Stochastic Gradient Descent (SGD) or its variants, with the loss function typically defined as categorical cross-entropy for classification tasks:

$$\mathcal{L} = - \sum_{i=1}^N y_i \log \hat{y}_i, \quad (2.25)$$

where  $y_i$  is the ground truth label,  $\hat{y}_i$  is the predicted probability, and  $N$  is the number of classes. The gradients of the loss function with respect to the network parameters are computed using backpropagation [59]. Optimization algorithms such as [Adaptive Moment Estimation \(ADAM\)](#) [60] and [Root Mean Square Propagation \(RMSProp\)](#) [61] are commonly employed to improve convergence.

## 2.1.6 Reinforcement Learning Fundamentals

[Reinforcement Learning \(RL\)](#) is a framework for sequential decision-making, where an *agent* learns to interact with an *environment* to maximize cumulative rewards [20]. Unlike supervised learning, which relies on labelled data, RL employs a trial-and-error approach, where the agent explores different strategies and refines its policy based on received feedback [62], [63]. This process is typically formalized using a [Markov Decision Process \(MDP\)](#), which

provides a mathematical foundation for modelling decision-making problems in dynamic environments.

### 2.1.6.1 Markov Decision Processes

A **Markov Decision Process (MDP)** is a 5-tuple  $\mathcal{M} = \langle \mathcal{S}, \mathcal{A}, P, R, \gamma \rangle$ , where:

- $\mathcal{S}$  is the set of all possible states of the environment.
- $\mathcal{A}$  is the set of all possible actions available to the agent.
- $P(s'|s, a)$  is the transition probability function, defining the probability of moving to state  $s' \in \mathcal{S}$  after taking action  $a \in \mathcal{A}$  in state  $s$ .
- $R(s, a)$  is the reward function, specifying the immediate scalar reward received after executing action  $a$  in state  $s$ .
- $\gamma \in [0, 1]$  is the discount factor, determining the importance of future rewards relative to immediate rewards.

The Markov property states that the probability of transitioning to the next state  $s_{t+1}$  depends only on the current state  $s_t$  and action  $a_t$ , and not on the history of previous states and actions [64]:

$$P(s_{t+1}|s_t, a_t, s_{t-1}, a_{t-1}, \dots, s_0, a_0) = P(s_{t+1}|s_t, a_t). \quad (2.26)$$

Given an **MDP**, the agent's objective is to learn an optimal policy  $\pi^*(a|s)$  that maximizes the expected cumulative reward, known as the return:

$$G_t = \sum_{k=0}^{\infty} \gamma^k r_{t+k+1}, \quad (2.27)$$

where  $r_{t+k+1}$  is the reward received at time step  $t + k + 1$  and  $\gamma$  ensures that future rewards contribute less significantly than immediate rewards.

### 2.1.6.2 States, Actions, Rewards, and Policies

**States and Observations.** A state  $s_t \in \mathcal{S}$  fully describes the environment at time step  $t$ . In many real-world scenarios, the agent has access only to a partial observation  $o_t$  rather than the full state, leading to a **Partially Observable Markov Decision Process (POMDP)** [65]. In such cases, the agent maintains a belief distribution over states to make decisions.

**Action Space.** The action space  $\mathcal{A}$  defines the set of all possible actions the agent can take. It can be discrete, as in board games where the agent selects a finite set of moves [66], or continuous, as in robotic control tasks where actions involve real-valued motor torques [67].

**Rewards and Return.** The reward function  $R(s, a)$  provides immediate feedback on the desirability of an action in a given state. The agent's goal is to maximize the expected return, which is either finite-horizon undiscounted:

$$G_t = \sum_{k=0}^T r_{t+k+1}, \quad (2.28)$$

or infinite-horizon discounted:

$$G_t = \sum_{k=0}^{\infty} \gamma^k r_{t+k+1}, \quad (2.29)$$

where  $\gamma \in (0, 1]$  is a discount factor that prioritizes immediate rewards.

**Policy Representation.** A policy  $\pi(a|s)$  defines the agent's strategy by mapping states to actions. Policies can be:

- Deterministic: The agent always selects the same action for a given state:

$$a_t = \mu(s_t) \quad (2.30)$$

- Stochastic: The agent samples actions from a probability distribution:

$$a_t \sim \pi(\cdot|s_t) \quad (2.31)$$

.

Policy optimization methods in deep reinforcement learning often involve parameterized policies, where a neural network with parameters  $\theta$  approximates  $\pi_\theta(a|s)$  [68].

**Value Functions.** Value functions estimate the expected return from a state or state-action pair:

- State-value function:

$$V^\pi(s) = \mathbb{E}_\pi [G_t \mid s_t = s] \quad (2.32)$$

- Action-value function:

$$Q^\pi(s, a) = \mathbb{E}_\pi [G_t \mid s_t = s, a_t = a] \quad (2.33)$$

The Bellman equation expresses the recursive relationship between value functions:

$$V^\pi(s) = \mathbb{E}_\pi [R(s, a) + \gamma V^\pi(s') \mid s] \quad (2.34)$$

The optimal policy  $\pi^*$  maximizes the expected return:

$$\pi^*(s) = \arg \max_a Q^*(s, a) \quad (2.35)$$

### 2.1.6.3 Conclusion

Reinforcement learning provides a mathematical framework for sequential decision-making, where an agent interacts with an environment to maximize cumulative rewards. By formalizing the problem as an [MDP](#), [RL](#) enables efficient learning through policies, value functions, and reward optimization. Recent advances in deep [RL](#) have extended these principles to complex, high-dimensional problems, such as robotic control [67], game playing [66], and autonomous decision-making [63].

## 2.1.7 Policy Learning in Reinforcement Learning

In [RL](#), an agent seeks to optimize a *policy*,  $\pi(a|s)$ , which defines a probability distribution over actions given a state. The primary goal of policy learning is to find an optimal policy  $\pi^*$  that maximizes the expected cumulative reward. Policy learning methods can be broadly classified into *model-free* and *model-based* approaches, with further subdivisions into *value-based* and *policy gradient* methods [20], [63], [69]. This section provides a formal exposition of these methods and their mathematical underpinnings.

### 2.1.7.1 Model-Free vs. Model-Based RL

A fundamental distinction in [RL](#) is whether the agent explicitly models the environment dynamics. *Model-free* [RL](#) methods learn a policy or a value function directly from interactions with the environment, without constructing an explicit transition model [63]. These methods typically require large amounts of data but are widely used due to their simplicity and applicability to unknown environments.

Conversely, *model-based* [RL](#) methods attempt to learn a model of the transition dynamics,  $P(s'|s, a)$ , and the reward function,  $R(s, a)$ , enabling the agent to simulate and plan ahead [62]. The advantage of model-based methods lies in their sample efficiency, as they leverage the learned model for decision-making without direct environment interaction. However, inaccuracies in the learned model can lead to suboptimal policies due to model bias.

Mathematically, an [RL](#) agent seeks to maximize the expected return:

$$J(\pi) = \mathbb{E}_\pi \left[ \sum_{t=0}^{\infty} \gamma^t R(s_t, a_t) \right], \quad (2.36)$$

where  $\gamma \in (0, 1]$  is the discount factor ensuring convergence. In model-free RL, this objective is optimized directly, whereas model-based RL first estimates the transition model before optimizing  $J(\pi)$ .

### 2.1.7.2 Value-Based Methods (Q-Learning, Deep Q-Networks)

Value-based methods focus on estimating the *action-value function*:

$$Q^\pi(s, a) = \mathbb{E}_\pi \left[ \sum_{t=0}^{\infty} \gamma^t R(s_t, a_t) \mid s_0 = s, a_0 = a \right], \quad (2.37)$$

which represents the expected return from state  $s$  after taking action  $a$  and following policy  $\pi$ . The optimal action-value function satisfies the *Bellman optimality equation* [70]:

$$Q^*(s, a) = \mathbb{E} \left[ R(s, a) + \gamma \max_{a'} Q^*(s', a') \mid s, a \right] \quad (2.38)$$

**Q-Learning.** Q-Learning [71] is an off-policy algorithm that approximates  $Q^*(s, a)$  using the update rule:

$$Q(s, a) \leftarrow Q(s, a) + \alpha \left[ r + \gamma \max_{a'} Q(s', a') - Q(s, a) \right], \quad (2.39)$$

where  $\alpha$  is the learning rate. This iterative update ensures convergence to the optimal Q-function under mild conditions.

**Deep Q-Networks.** Deep Q-Networks (DQNs) [63] extend Q-learning by employing a deep neural network  $Q_\theta(s, a)$  to approximate the Q-function, where  $\theta$  are the network parameters. The optimization objective minimizes the Temporal Difference (TD) error:

$$L(\theta) = \mathbb{E} \left[ (y_t - Q_\theta(s, a))^2 \right], \quad (2.40)$$

where the target value  $y_t$  is given by:

$$y_t = r + \gamma \max_{a'} Q_{\theta'}(s', a'), \quad (2.41)$$

and  $\theta'$  represents the parameters of a slowly updated *target network* to stabilize training. Experience replay is employed to break correlations between consecutive samples, improving convergence.

### 2.1.7.3 Policy Gradient Methods

Policy gradient methods optimize a parameterized policy  $\pi_\theta(a|s)$  by directly maximizing the expected return:

$$J(\theta) = \mathbb{E}_{\pi_\theta} \left[ \sum_{t=0}^{\infty} \gamma^t R(s_t, a_t) \right] \quad (2.42)$$

The gradient of  $J(\theta)$  is computed using the policy gradient theorem [72]:

$$\nabla_\theta J(\theta) = \mathbb{E}_{\pi_\theta} [\nabla_\theta \log \pi_\theta(a|s) Q^\pi(s, a)] \quad (2.43)$$

**REINFORCE Algorithm.** The **REward Increment = Nonnegative Factor  $\times$  Offset Reinforcement  $\times$  Characteristic Eligibility (REINFORCE)** algorithm [73] updates the policy parameters using Monte Carlo estimates:

$$\theta \leftarrow \theta + \alpha \sum_{t=0}^T \nabla_\theta \log \pi_\theta(a_t|s_t) G_t, \quad (2.44)$$

where  $G_t$  is the empirical return from time  $t$  onward. While simple, **REINFORCE** suffers from high variance in gradient estimates.

**Proximal Policy Optimization** **Proximal Policy Optimization (PPO)** [68] improves stability by introducing a surrogate objective:

$$L^{\text{PPO}}(\theta) = \mathbb{E} [\min(r_t(\theta)A_t, \text{clip}(r_t(\theta), 1 - \epsilon, 1 + \epsilon)A_t)], \quad (2.45)$$

where  $r_t(\theta) = \frac{\pi_\theta(a_t|s_t)}{\pi_{\theta_{\text{old}}}(a_t|s_t)}$  is the probability ratio between new and old policies,  $A_t = A(s_t, a_t)$  is the advantage function that measures how much better an action  $a_t$  is compared to the average action in state  $s_t$ , and  $\epsilon$  is a clipping parameter to constrain updates.

**Soft Actor-Critic.** **Soft Actor Critic (SAC)** [74] incorporates an entropy term  $\mathcal{H}(\pi)$  into the objective:

$$J(\pi) = \mathbb{E} \left[ \sum_{t=0}^{\infty} \gamma^t (R(s_t, a_t) + \alpha \mathcal{H}(\pi(\cdot|s_t))) \right], \quad (2.46)$$

where  $\alpha$  is a temperature parameter controlling the trade-off between exploration and exploitation. SAC employs an off-policy actor-critic framework, optimizing both the policy and the Q-function.

#### 2.1.7.4 Conclusion

Policy learning in RL encompasses both model-free and model-based methods, with further distinctions between value-based approaches like Q-learning and DQN, and policy gradient methods such as REINFORCE, PPO, and SAC. While value-based methods excel in discrete action spaces, policy gradient methods are well-suited for continuous control tasks. Ongoing research continues to refine these approaches, enhancing their stability, sample efficiency, and generalization capabilities [69], [74].

### 2.1.8 Reinforcement Learning for Robot Control

---

RL has revolutionized control and robotics by enabling autonomous agents to learn complex behaviours through interaction with dynamic environments [75], [76]. Unlike traditional control methods based on predefined models and optimization techniques, RL provides a data-driven approach to learning policies that map high-dimensional sensory inputs to continuous control actions [77]. This section explores RL techniques specifically tailored for continuous control tasks and autonomous navigation.

#### 2.1.8.1 RL in Continuous Control Tasks

Control problems in robotics often involve high-dimensional continuous action spaces, where an agent must generate smooth motor commands for tasks such as locomotion and dexterous manipulation [67]. The challenge lies in efficiently learning policies that generalize well to diverse conditions while ensuring stability and safety.

**Optimal Control and RL.** Classical optimal control relies on solving the Hamilton Jacobi Bellman (HJB) equation:

$$V^*(s) = \max_a [R(s, a) + \gamma \mathbb{E}_{s' \sim P} [V^*(s')]], \quad (2.47)$$

where  $V^*(s)$  is the optimal value function. While Dynamic Programming (DP) methods such as Linear Quadratic Regulator (LQR) solve this equation for linear systems, they do not scale well to high-dimensional robotic tasks. RL methods overcome this limitation by learning parametric approximations of  $V^*(s)$  or directly optimizing policies [78].

**Model-Based RL for Control.** In robotics, data efficiency is critical, as collecting physical interactions is costly. Model-Based Reinforcement Learning (MBRL) methods improve sample

efficiency by learning an approximate transition model  $\hat{P}(s'|s, a)$  and using it for planning [79]. Given a learned model, policies can be optimized using [Model Predictive Control \(MPC\)](#):

$$a_t = \arg \max_a \sum_{k=0}^T \gamma^k R(s_{t+k}, a_{t+k}), \quad (2.48)$$

where  $T$  is the planning horizon. Hybrid approaches such as Probabilistic Ensembles with Trajectory Sampling (PETS) further improve robustness by modelling uncertainty in  $\hat{P}$  [79].

**Energy-Based and Safety-Critical RL.** Safety is paramount in robotic control, requiring constraints on actions and trajectories. Energy-based RL methods incorporate constraints via Control Lyapunov Functions (CLFs) and Control Barrier Functions (CBFs) [80]:

$$\frac{dV(s)}{dt} + \alpha(V(s)) \leq 0, \quad \forall s \in \mathcal{S}, \quad (2.49)$$

where  $\alpha(\cdot)$  is a class- $\mathcal{K}$  function ensuring stability. These approaches guarantee that RL policies respect physical constraints while optimizing for task performance.

### 2.1.8.2 RL for Autonomous Navigation

Autonomous navigation involves decision-making in dynamic, often partially observable environments. RL-based approaches leverage spatial reasoning, motion planning, and obstacle avoidance to enable robots to navigate in unstructured environments such as urban streets or indoor spaces [81].

**Policy Learning for Navigation.** Navigation tasks can be framed as a goal-conditioned RL problem, where the policy  $\pi(a|s, g)$  conditions on a goal state  $g$ . The reward function is often defined using geodesic distance:

$$R(s, a) = -d(s, g), \quad (2.50)$$

where  $d(s, g)$  is the shortest path distance between the agent's current state and the goal.

**Hierarchical RL for Long-Horizon Navigation.** Hierarchical Reinforcement Learning (HRL) decomposes navigation into high-level planning and low-level control [82]:

$$g_t = \pi_{\text{high}}(s_t), \quad (2.51)$$

$$a_t = \pi_{\text{low}}(s_t, g_t). \quad (2.52)$$

This structure enables efficient exploration and generalization across large environments.

**Sim-to-Real Transfer in Navigation.** One challenge in RL-based navigation is the reality gap—the discrepancy between simulated and real-world environments. Domain adaptation techniques such as Randomized-to-Canonical Adaptation Networks (RCANs) [83] minimize this gap by mapping simulated observations  $o_{\text{sim}}$  to a canonical space:

$$o_{\text{real}} = f_{\theta}(o_{\text{sim}}), \quad (2.53)$$

where  $f_{\theta}$  is a learned mapping function. This enables RL policies trained in simulation to generalize effectively to real-world navigation tasks.

## 2.2 Applications

### 2.2.1 Autonomy in Endovascular Navigation

The field of autonomous endovascular navigation has advanced significantly due to the integration of robotics and medical imaging technologies. To evaluate a system's autonomy level, Haidegger [84] introduces the concept of a **Degree of Autonomy (DoA)** metric. This metric provides a structured framework to assess the autonomy levels of Medical Electrical Equipment (MEE) and Medical Electrical System (MES) in surgical settings, highlighting progressive capabilities for enabling autonomous endovascular interventions. The **DoA** metric, as defined in ISO/IEC Technical Report IEC/TR 60601-4-1, employs a mathematical model to characterize autonomy through four core cognitive-related processes:

$$\text{DoA} = F\{G, E, M, S\}$$

where

- *G* represents "Generate an option," entailing the formulation of possible actions or strategies based on real-time observations.
- *E* represents "Execute an option," which involves carrying out a chosen action or strategy, potentially with robotic assistance.
- *M* represents "Monitor an option," gathering information necessary for assessing the system's status, including internal and external sensory inputs.
- *S* represents "Select an option," where a decision is made on a specific course of action from the generated options.

The **DoA** is computed as a normalized sum of these functions, each quantified on a linear scale from 0 (fully manual) to 1 (fully autonomous), thus:

$$\text{DoA} \in [0, 1]$$

In this scale, a **DoA** value of 0 indicates a completely manual system, whereas a **DoA** of 1 denotes full autonomy. Each functional component *G*, *E*, *M*, and *S* can be managed by either a human operator or a computerized system, thereby influencing the overall autonomy level. This thesis aims to develop a fully autonomous system for navigation in endovascular settings.

Autonomous endovascular navigation, driven by **AI**, represents a transformative shift in interventional procedures, with potential benefits including improved procedural precision,

minimized radiation exposure, and reduced cognitive and physical strain on clinicians. These benefits are associated with enabling a DoA = 1 system. Recent research has explored various ML approaches, including RL and Learning from Demonstration (LfD), for navigating complex vascular structures using catheters and guidewires. This section reviews major methodologies in autonomous endovascular navigation, focusing on reinforcement learning, Imitation Learning (IL), and hybrid techniques that integrate expert-driven data with RL.

### 2.2.1.1 Reinforcement Learning (RL)

Reinforcement learning has become a leading approach in autonomous endovascular navigation, with approximately 64% of studies utilizing RL-based methods [85]. RL enables systems to autonomously learn optimal navigation strategies by receiving environmental feedback based on actions taken, simulating human learning through iterative trial-and-error [21]. Several RL algorithms, including Deep Deterministic Policy Gradient (DDPG) and Dueling Deep Q-Network (DDQN), have been applied in endovascular settings. For instance, DDQNs has been used to guide endovascular catheters, optimizing navigation paths based on Electro-magnetic (EM) tracking sensor feedback [86]. However, RL often requires extensive in vitro validation before clinical application due to challenges posed by the dynamic and variable nature of human vasculature [87].

### 2.2.1.2 Learning from Demonstration (LfD)

LfD, also known as IL, allows models to learn by observing expert operators. In endovascular navigation, LfD is frequently combined with RL to create a hybrid approach that uses expert-generated trajectories as a baseline, reducing the exploration time needed for effective RL training [88]. This combined LfD-RL method has shown promise in improving navigation efficiency, as pre-acquired expert knowledge facilitates a smoother transition from simulation to physical trials [89]. Furthermore, this approach reduces mechanical wear on robotic systems, a critical advantage for the repeated cycles often required in RL training [90].

### 2.2.1.3 Hybrid Approaches: Combining RL and Imitation Learning

Several studies have implemented a hybrid approach, merging RL and LfD to leverage the advantages of both techniques. For example, Chi *et al.* [88] used Generative Adversarial Imitation Learning (GAIL) in conjunction with RL to enhance the adaptability of robotic catheter navigation across various vascular geometries [88]. This hybrid technique seeks to accelerate the training process, enhance navigation robustness, and ensure that systems generalize beyond specific vascular layouts encountered during initial training [91].

### 2.2.1.4 Experimental Environments and Validation

Experimental setups for evaluating autonomous navigation systems are primarily in vitro platforms, accounting for 79% of studies, with a smaller subset employing in silico simulations. These controlled environments help mitigate risk before clinical deployment, though they do not fully capture the complexity of live human anatomy [92]. Studies frequently utilize EM-tracking for real-time 3D visualization, aiding precise catheter orientation, though this technology would require innovation for clinical translation due to high costs and complexity [87]. Additionally, standardized performance metrics, including path length, procedural time, and task success rates, are essential for evaluating and comparing navigation models, though inconsistencies in metrics across studies present challenges for systematic assessment [17].

## 2.2.2 Simulation Environments

Simulation environments for endovascular interventions are categorized based on their fidelity and intended use, including synthetic, Virtual Reality (VR), animal, and cadaveric simulations. Each type offers distinct benefits and limitations depending on the desired outcomes in training, path planning, and system testing [93, 94, 95]. Synthetic environments, such as high-fidelity phantoms, are widely used for skill acquisition and procedural practice. These platforms are particularly advantageous for integrating imitation learning methods, allowing robotic systems to develop foundational skills by observing human techniques [88]. However, synthetic simulators can be costly and require physical maintenance, which poses limitations for continuous, scalable training [96].

In the realm of VR-based simulations, advances have allowed for realistic modelling of endovascular procedures, providing a risk-free environment where trainees and autonomous agents can perform repetitive tasks to reinforce procedural learning and optimize path-planning strategies [95, 97]. VR platforms often include haptic feedback systems to mimic tactile sensations, enhancing realism and user engagement [96]. Yet, despite these advances, many VR simulators are proprietary and lack open-source accessibility, limiting their integration with customizable training protocols and RL algorithms.

### 2.2.2.1 Autonomous Catheter Navigation

Simulation environments have played a crucial role in progressing autonomous catheterization research. Initial studies in this field aimed at providing assistive navigation tools, but recent efforts are increasingly focused on higher levels of autonomy, such as semi-autonomous or fully autonomous navigation [98]. Autonomous catheterization has primarily leveraged Deep Reinforcement Learning (DRL) techniques, which adapt to complex vascular geometries by using fluoroscopic images or other imaging modalities to train models on bi-dimensional

synthetic phantoms [86, 91]. However, alternative methods such as Dijkstra’s algorithm and breadth-first search have also been applied for path planning in non-RL-based approaches, demonstrating diverse methodologies for addressing the challenges of autonomous navigation in simulated environments [99, 100].

### 2.2.2.2 Imitation Learning in Endovascular Simulation

IL, particularly when combined with RL, is pivotal in endovascular simulations for translating human expertise into robotic actions. It enables surgical agents to replicate complex manoeuvres based on human demonstrations, which is especially beneficial in scenarios requiring precise navigation through dynamic anatomical structures [101]. This technique has been applied to various simulation environments, where agents trained on expert demonstrations were able to improve navigation accuracy and procedural efficiency [102, 103]. Moreover, advanced models, including GAIL, have been implemented within synthetic and VR environments to refine agent decision-making and mimic expert strategies under simulated anatomical conditions [101]. These methods demonstrate significant potential for achieving task autonomy in surgery, where a robotic agent, under supervised conditions, can assume part of the decision-making responsibilities [104].

## 2.2.3 Endovascular Tool Segmentation and Tracking

Endovascular tool segmentation (*i.e.*, guidewires and catheters) in fluoroscopic images is essential for precise navigation during minimally invasive procedures, enabling accurate tracking of the tool position and assisting in real-time decision-making. Techniques for guidewire segmentation have evolved from traditional image processing to advanced deep learning methods, allowing for improved detection accuracy and computational efficiency. This section reviews various approaches for guidewire segmentation, focusing on x-ray-based techniques, machine learning, and deep learning methods.

### 2.2.3.1 Tool Visualization

X-ray fluoroscopy is the standard imaging modality for visualizing guidewires and catheters during catheter-based interventions, such as Percutaneous Coronary Intervention (PCI) and Transcatheter Aortic Valve Replacement (TAVR). These procedures require real-time visualization to guide the guidewire accurately through complex vascular structures. Traditional x-ray-based segmentation methods rely on the intensity and shape characteristics of the guidewire within the fluoroscopic images. Techniques such as thresholding, edge detection, and filtering are commonly applied to extract the guidewire’s linear structure from the background. For example, methods utilizing Difference-of-Gaussian (DoG) filters and Laplacian-of-Gaussian (LoG) filters have been effective in enhancing the guidewire’s features, enabling accurate differentiation from surrounding anatomical structures [105], [106].

These intensity-based methods provide a relatively straightforward segmentation approach; however, they are sensitive to variations in image quality, such as noise and occlusions, which are common in fluoroscopic imaging. To mitigate these issues, techniques such as Kalman filtering have been integrated to track the guidewire's position across frames, compensating for noise and ensuring smoother segmentation [107]. Additionally, multi-view setups, which apply epipolar constraints across paired views, allow for 3D localization of guidewires, enhancing segmentation accuracy and enabling applications like 3D roadmapping [108].

### 2.2.3.2 ML Approaches in Endovascular Tool Segmentation

The integration of machine learning has advanced guidewire segmentation by providing data-driven solutions that can generalize to variations in guidewire shape and appearance. Early machine learning methods applied techniques like dictionary learning, which learns a set of representative guidewire shapes from annotated data, allowing for robust segmentation by fitting these learned shapes to new image frames [109]. This approach enhances segmentation in cases where traditional filtering methods struggle, particularly when dealing with guidewires of different shapes or in varying anatomical locations.

Model-based approaches have also been applied, using predefined models of guidewire appearance to guide segmentation. For instance, B-spline curves are commonly used to model guidewire shapes as they allow for smooth, continuous curves that match the guidewire's natural form. These B-spline models can be initialized in the first frame and updated in subsequent frames to maintain alignment with the guidewire's current position, thus providing a balance between shape accuracy and computational efficiency [110]. However, model-based approaches still require initial manual labelling or accurate initialization, which can limit their usability in fully automated settings.

### 2.2.3.3 Deep Learning in Endovascular Tool Segmentation

Recent advances in deep learning have led to the development of highly accurate and automated segmentation frameworks for guidewires. CNNs and Fully Convolutional Networks (FCNs) have been widely adopted for their ability to learn hierarchical features directly from raw image data, enabling robust guidewire segmentation even in challenging imaging conditions [108]. For instance, Baur *et al.* [111] demonstrated the effectiveness of FCN for segmenting catheters and guidewires in fluoroscopic images, leveraging the network's capability to detect tubular structures across varying levels of contrast and noise [111].

Furthermore, CNN-based approaches have facilitated real-time guidewire tracking by using temporal data across sequential frames, providing continuous updates to the guidewire's segmented path. These methods often outperform traditional algorithms in accuracy and computational speed, making them highly suitable for real-time surgical assistance. However,

deep learning approaches are typically data-intensive, requiring large, annotated datasets to achieve high accuracy. In clinical environments where labelled data is limited, this can pose challenges for implementing these methods effectively [109].

## 2.2.4 3D Reconstruction

Accurate three-dimensional visualization of interventional devices is crucial for successful navigation through complex vascular anatomy, providing clinicians with spatial awareness that cannot be achieved through two-dimensional projections alone. During endovascular procedures, clinicians must navigate guidewires and catheters through tortuous vascular pathways while avoiding perforation or dissection of vessel walls. Traditional 2D fluoroscopy lacks depth perception and can obscure the true spatial relationships between devices and anatomy, potentially leading to navigation errors or procedural complications. The ability to reconstruct accurate 3D representations of guidewires in real-time thus addresses a fundamental clinical need, enabling more precise navigation, reducing procedure times, and improving patient safety.

Among the available techniques, bi-planar X-ray imaging has established itself as a gold standard for 3D reconstruction in clinical settings, offering simultaneous orthogonal views that enable precise triangulation of device positions and shapes. This technology is particularly valuable in complex interventions such as neurovascular procedures, structural heart interventions, and aortic repairs, where millimeter-level accuracy can significantly impact procedural outcomes. Despite its advantages, bi-planar imaging faces challenges including equipment cost, radiation exposure, and workflow integration, prompting the exploration of alternative approaches that attempt to balance reconstruction accuracy with clinical practicality. The evolution of 3D reconstruction methods thus reflects a continuous trade-off between precision, efficiency, and clinical feasibility, with each technique offering distinct advantages and limitations in the context of endovascular interventions.

Advances in guidewire reconstruction and localization have significantly enhanced precision and navigation during minimally invasive interventions. The focus of recent work has been on improving 3D localization accuracy and reducing the clinical workflow disruptions associated with traditional fluoroscopic methods. Various reconstruction techniques have emerged, notably those relying on multi-view fluoroscopy, monoplane approaches supplemented by kinematic data, and, more recently, machine learning-based methods.

### 2.2.4.1 Biplane Fluoroscopic Approaches

Biplane fluoroscopy has been foundational for accurate guidewire shape estimation, utilizing dual-angle imaging for real-time triangulation of 3D structures. Early works, such as Burgner, Herrell, and Webster III [112], employed projective-invariant triangulation methods to derive

the guidewire's centreline, achieving accurate reconstructions but often requiring extensive calibration and image processing. This approach has since been refined by Wagner *et al.* [113] and Hoffmann *et al.* [114], Hoffmann *et al.* [115], and Hoffmann *et al.* [116], who incorporated dynamic 4D modelling to capture continuous guidewire movement, yielding enhanced shape reconstruction. These methods have proved effective in experimental setups; however, the high cost, radiation exposure, and operational constraints of biplane systems during interventions limit their clinical applicability. The dependence on dedicated biplane C-arm configurations also complicates their integration into diverse clinical environments, leading to increased interest in monoplane alternatives.

#### 2.2.4.2 Monoplane Fluoroscopic Techniques

To mitigate the limitations of biplane fluoroscopy, monoplane C-arm systems have been adapted for guidewire shape reconstruction through the integration of supplementary data sources. One approach, introduced by Lobaton *et al.* [117], involved combining fluoroscopic images with kinematic models in bronchoscopy, which provided deformable surface parameterization to improve positional accuracy. This method, while precise, was constrained to offline simulation environments and required meticulous C-arm adjustments. Vandini *et al.* [118] expanded this monoplane approach by reconstructing robotic catheter shapes through 2D centreline extraction and appearance priors, albeit with workflow disruptions due to frequent C-arm repositioning. To address this, Vandini *et al.* [119] later proposed a kinematic model-integrated monoplane method for transnasal robotic surgery, eliminating the need for C-arm adjustments and allowing more seamless workflow integration.

Further advancements have been made by Otake *et al.* [120] and Papalazarou Papalazarou, Rongen, *et al.* [121], who incorporated piecewise-rigid 2D/3D registration and non-rigid structure-from-motion techniques. These methods demonstrated improved intraoperative adaptability, yet multiple monoplane views were often required to achieve accurate 3D reconstructions, increasing computational demands. Although monoplane fluoroscopy reduces radiation exposure compared to biplane setups, it still presents workflow challenges in clinical environments, underscoring the need for real-time adaptable systems.

#### 2.2.4.3 Deep Learning and Data-Driven Reconstruction Techniques

Emerging deep learning methods have shown potential to address limitations of traditional fluoroscopic techniques by interpreting monoplane images with high precision. While these models offer promising avenues for reducing reliance on multi-view systems, their application to full 3D guidewire reconstruction remains largely unexplored. As highlighted by Ramadani *et al.* [122], current deep learning efforts primarily target segmentation or localization tasks, with true 3D reconstruction still in its infancy. Moreover, the need for large annotated datasets and high computational demands poses additional challenges for clinical deployment.

## Chapter 3

---

# CathSim

*Autonomous robots in endovascular operations have the potential to navigate circulatory systems safely and reliably while decreasing susceptibility to human errors. However, numerous challenges are involved in the training process of such robots, including prolonged training times and safety concerns related to catheter-aorta interactions. Recently, endovascular simulators have been utilized in medical training, but they are typically unsuitable for autonomous catheterization due to a lack of standardization and integration with reinforcement learning frameworks. Furthermore, most current simulators are closed-source, which hinders the collaborative development of safe and reliable autonomous systems through shared learning and community-driven enhancements. To address these limitations, CathSim is introduced as an open-source simulation environment designed to accelerate the development of machine learning algorithms for autonomous endovascular navigation. A high-fidelity catheter and aorta are simulated within a state-of-the-art endovascular robot. Real-time force sensing between the catheter and the aorta is provided within the simulation. The simulator is validated through two distinct catheterization tasks — navigation towards the Left Common Carotid Artery (LCCA) and the Brachiocephalic Artery (BCA) — using two widely adopted reinforcement learning algorithms: Soft Actor Critic (SAC) and Proximal Policy Optimization (PPO). The experimental results demonstrate that the open-source simulator effectively mimics the behaviour of real-world endovascular robots and facilitates the development of various autonomous catheterization tasks.*

This chapter presents the work from the following publication:

**Jianu, T.** *et al.*, “Cathsim: An open-source simulator for endovascular intervention,” *IEEE Transactions on Medical Robotics and Bionics*, 2024, Code available at: <https://airvlab.github.io/cathsim>

## 3.1 Introduction

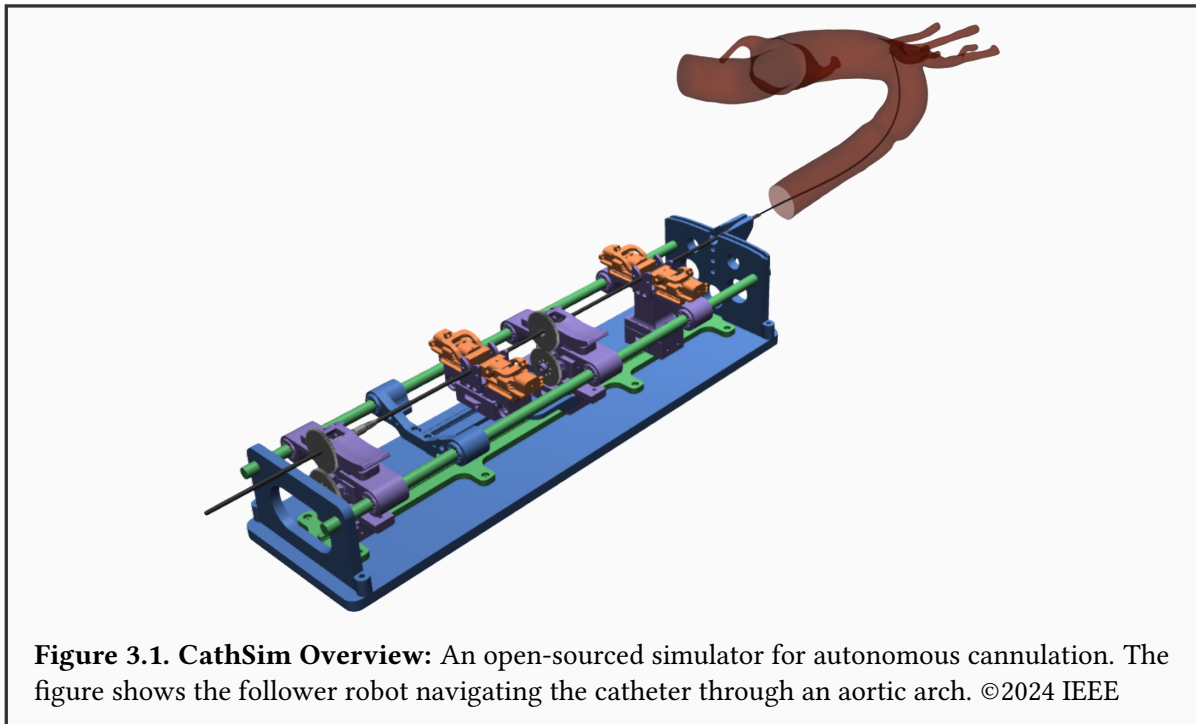
Endovascular intervention has significantly evolved from traditional open surgery. It is performed through a small incision, typically in the common femoral or radial artery, allowing surgical tools such as catheters and guidewires to be manoeuvred within the vasculature. This form of **Minimally Invasive Surgery (MIS)** offers numerous benefits, including reduced blood loss, shorter recovery time, less postoperative pain, and a diminished inflammatory response compared to traditional methods [124]. In clinical practice, navigation of the catheter and guidewire to the diagnostic site is guided by fluoroscopy, a real-time X-ray imaging technique. However, endovascular intervention is not without limitations, such as the absence of sensory feedback, radiation exposure, operator dependency, a steep learning curve, and the need for precise, dexterous manipulation [125].

To mitigate the continuous radiation risk to surgeons during fluoroscopic procedures, numerous robotic systems with leader-follower (master-slave) teleoperation architectures have been developed [126, 127, 128]. In these systems, a leader device is controlled by the surgeon, with commands mapped to a follower robot that executes the corresponding actions. This setup enables remote operation from a safe, radiation-free zone. Recent advancements have focused on the development of Magnetic Resonance (MR)-safe robotic platforms [126], eliminating ionizing radiation exposure while facilitating soft tissue visualization, including vasculature [129, 130]. In academic research, these robotic systems have been further enhanced with assistive features such as force/torque sensing [131], haptic feedback [96], and real-time segmentation and tracking [132].

Recent robotic platforms for endovascular intervention have demonstrated assistive potential in supporting procedural success. However, two key limitations persist: *i*) the lack of autonomy [133], and *ii*) increased procedural duration compared to manual techniques [88]. In current systems, the surgeon must navigate the three-dimensional vascular space using only two-dimensional fluoroscopic imaging and without the aid of haptic feedback. This setup imposes high cognitive and physical demands, requiring exceptional precision to avoid vascular damage under mentally strenuous conditions.

Procedural automation could alleviate these burdens by improving efficiency and reducing the risk of complications. Yet, achieving safe autonomy remains non-trivial—it necessitates the integration of sophisticated vision, learning, and control systems capable of meeting stringent safety requirements [133].

Endovascular navigation simulations have historically faced significant challenges, limiting their advancement and practical utility [134]. One major issue has been the absence of standardized environments. This issue is exemplified by the closed-source nature of many previous simulators, which, despite showcasing algorithmic innovations, are not publicly



accessible, thereby hindering reproducibility and broader community contributions. Computational performance, crucial for real-time response and complex algorithmic processing, is often insufficient in existing platforms. Furthermore, integration with frameworks such as the Gymnasium interface [135], which is essential for the streamlined development of **Reinforcement Learning (RL)**-based methods, is frequently absent. Additional barriers, including installation complexity and limited interactivity, further impede widespread adoption and iterative development within research contexts. Addressing these challenges is essential to advancing endovascular navigation simulations and supporting training and algorithm development. Related work in Section 3.1 further explores these limitations and introduces *CathSim*, an open-source, efficient, and high-fidelity simulation environment that responds directly to these needs.

In response to these challenges, a new **MIS** simulation environment tailored for endovascular procedures is introduced. The primary objective is to facilitate the development of endovascular navigation autonomy by providing a standardized environment familiar to the **Machine Learning (ML)** community. To this end, *CathSim* is presented as a real-time simulation platform for autonomous cannulation, developed using the MuJoCo physics engine [136]. MuJoCo was selected for its real-time performance, accurate physics modelling, and suitability for optimal control applications, making it well-suited to the intended objectives. An overview of the simulator is provided in Fig. 3.1. The key contributions and potential applications of the simulator are summarized as follows:

1. *CathSim* is introduced as a novel open-source simulation environment for endovascular

procedures.

2. Baselines and benchmarks are provided for autonomous cannulation tasks in *CathSim* using two widely adopted [RL](#) algorithms.

## 3.2 Related Work

**Table 3.1.** Endovascular Simulator Environments Comparison

| Simulator                      | Physics Engine      | Catheter                | Guidewire               | Aorta     | OS?            |
|--------------------------------|---------------------|-------------------------|-------------------------|-----------|----------------|
| Molinero <i>et al.</i> [96]    | Unity Physics [137] | Discretized             | ✗                       | 3D artery | ✗              |
| Karstensen <i>et al.</i> [138] | SOFA [139]          | Timoshenko <sup>1</sup> | ✗                       | 2D vessel | ✓              |
| Behr <i>et al.</i> [86]        | SOFA [139]          | Timoshenko <sup>1</sup> | ✗                       | 2D vessel | ✓              |
| Omisore <i>et al.</i> [140]    | CopelliaSim [141]   | ✗                       | Discretized             | 3D vessel | ✓ <sup>2</sup> |
| Schegg <i>et al.</i> [142]     | SOFA [139]          | ✗                       | Timoshenko <sup>1</sup> | 3D artery | ✓              |
| <b>CathSim</b> (ours)          | MuJoCo [136]        | Discretized             | ✗                       | 3D artery | ✓              |

<sup>1</sup> Timoshenko Beam theory [143]

<sup>2</sup> Primary engine is open source; however, certain functionalities require commercial licenses.

**Simulation Environments.** Endovascular surgical simulation environments can be categorized into four primary types: synthetic models, animal models, virtual systems, and human cadavers, each offering distinct advantages and inherent limitations [93, 94, 95, 97]. These environments are primarily designed for skill development [93, 144] or for the integration and development of assistive features, such as haptic feedback [96]. However, reliance on physical materials often renders them unsuitable for RL-based applications. Recent advancements have included high-fidelity synthetic phantoms for **Imitation Learning (IL)**, as exemplified by the SOFA simulation environment [139], which has been tested on two-dimensional synthetic phantoms [67]. Despite these developments, most environments remain closed-source, thereby limiting accessibility, hindering reproducibility, and restricting broader contributions to the field.

**Autonomous Catheterization.** Machine learning has enabled the shift from assistive features to semi-autonomous navigation in the context of autonomous catheterization [98]. In recent work, a focus has been placed on **Deep Reinforcement Learning (DRL)** due to its effectiveness in complex decision-making tasks, as demonstrated in domains such as autonomous driving. Numerous studies have utilized RL, particularly with image data derived from fluoroscopy [86, 91, 96, 138, 140]. While alternative methods, such as the Dijkstra algorithm or breadth-first search, have been employed [142, 145], model-free RL has been regarded as well-suited for handling the uncertainty and complexity associated with achieving higher autonomy. Nonetheless, most research remains in the early stages of autonomy [98], and comprehensive autonomous navigation of the vascular system continues to represent a challenging yet promising objective for RL.

In Table 3.1, a detailed comparison is provided of current learning-based works that utilize environments built on a variety of physics engines. A limitation of such environments is their

lack of public availability, which hinders reproducibility. *CathSim*, unlike other simulators, offers an open-source platform specifically designed for training autonomous agents, allowing for rapid development of various ML methodologies. Based on the MuJoCo framework [136], the simulator provides an advanced simulation environment suitable for real-time applications. In addition, real-time force sensing capabilities and high-fidelity, realistic visualization of the aorta, catheter, and endovascular robots are supported. In practice, *CathSim* can be used to train RL agents or serve as a practice platform for healthcare professionals.

Recent advancements in gym-based simulation frameworks have incorporated the SOFA platform, as demonstrated by SofaGym, a general framework for SOFA environments [146], and LapGym, designed specifically for laparoscopic surgery [147]. Both frameworks utilize the Finite Element Method (FEM) to simulate deformable objects and integrate a Gym API [148], representing significant progress in medical simulation. However, support for domain randomization—a critical component for training robust ML and RL models—is absent in these systems. In contrast, *CathSim* is focused specifically on endovascular navigation, leveraging the MuJoCo physics engine [136] and incorporating domain randomization. Additionally, highly realistic aortic models derived from post-mortem anatomies and Computerized Tomography (CT) scans are employed, offering a unique contribution to the medical simulation landscape. Unlike SofaGym’s broader application as a Gym wrapper for diverse SOFA environments and LapGym’s emphasis on laparoscopic surgery, *CathSim* provides targeted advancements in endovascular navigation simulation, enriching the field with application-specific innovations.

## 3.3 The CathSim Simulator

The *CathSim* environment is composed of three components: *i*) the follower robotic model for endovascular procedures, as introduced by Abdelaziz *et al.* [130], *ii*) the aortic arch phantoms, and *iii*) the catheter or guidewire. Real-time simulation is enabled, and support is provided for the training of state-of-the-art learning algorithms.

### 3.3.1 Robot Simulation

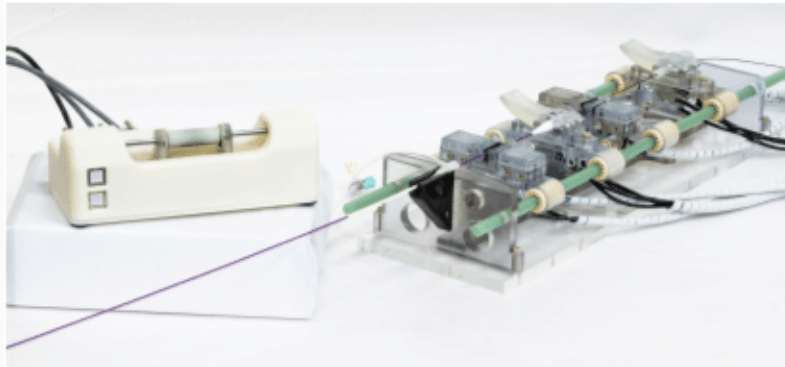
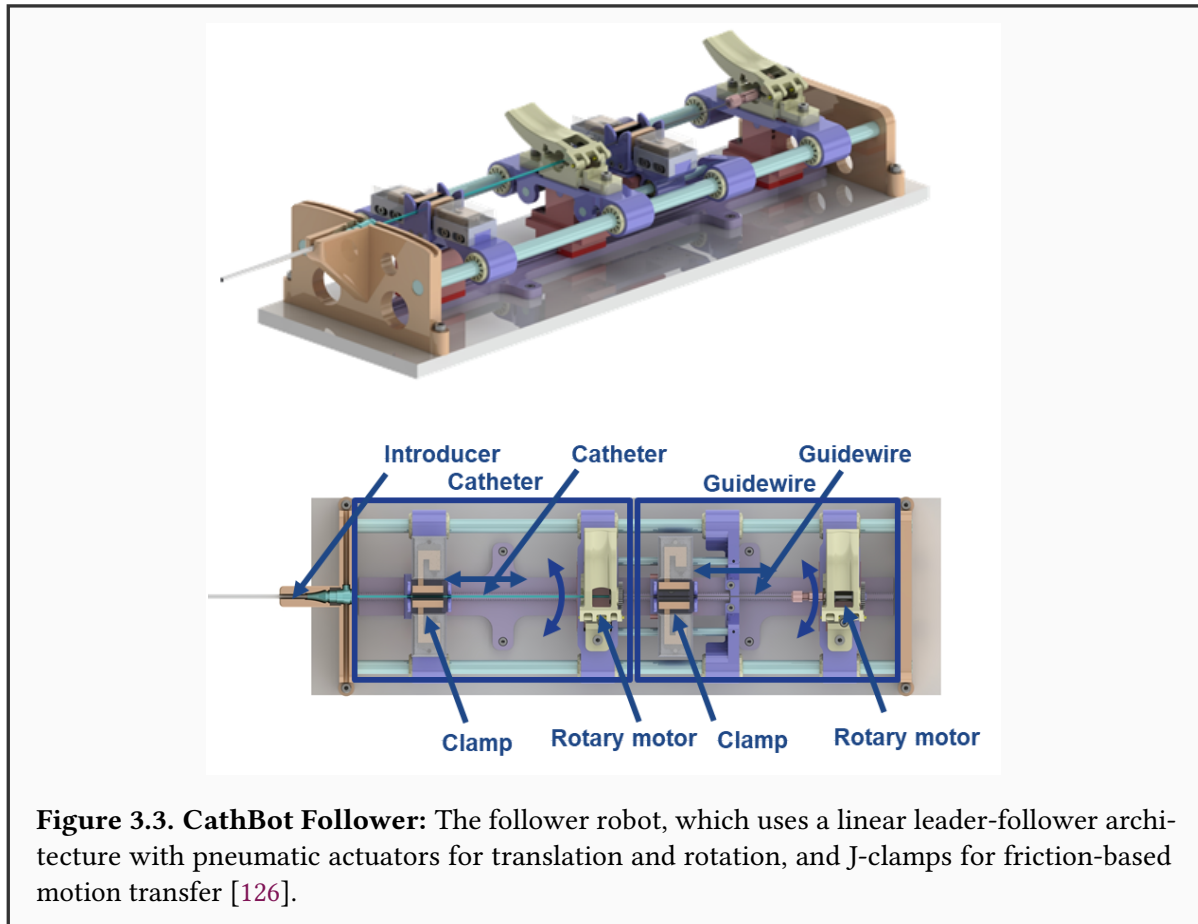


**Figure 3.2. CathBot:** The robotic platform for fluoroscopy and MR-guided endovascular interventions consists of leader device (*left*) and follower robot (*right*). Adapted from [132].

In this work, the transfer of CathBot, developed by Kundrat *et al.* [126], to simulation is pursued for the purpose of autonomous agent training. CathBot is selected due to its status as a state-of-the-art robot that is not restricted by a commercial licence. The design of CathBot follows the widely adopted leader-follower architecture, in which the leader robot uses haptic feedback generated by the catheter’s interaction with the environment through the navigation system [96], maintaining intuitive control that replicates human motion patterns such as insertion, retraction, and rotation. The follower robot mimics the leader’s motion and is composed of two pneumatic linear motors for translation, one pneumatic rotating stepper motor, and two pneumatic J-clamps for clamping the instrument during translational movements.

Given the linear mapping between the leader and the follower robot in CathBot’s design [126], the simulation focuses solely on the follower robot for simplicity. The follower robot is simulated by constructing four modular platforms attached to a main rail. On two of these platforms, a pair of clamps is positioned to secure the guidewire during translational motion, while the remaining two platforms are configured with rotary catheter and guidewire components to perform angular motion. The components responsible for translational movement along the main rail, as well as the clamps, are joined using prismatic joints. Revolute joints are used to attach the wheels, thereby enabling rotational motion of the catheter. The rotational

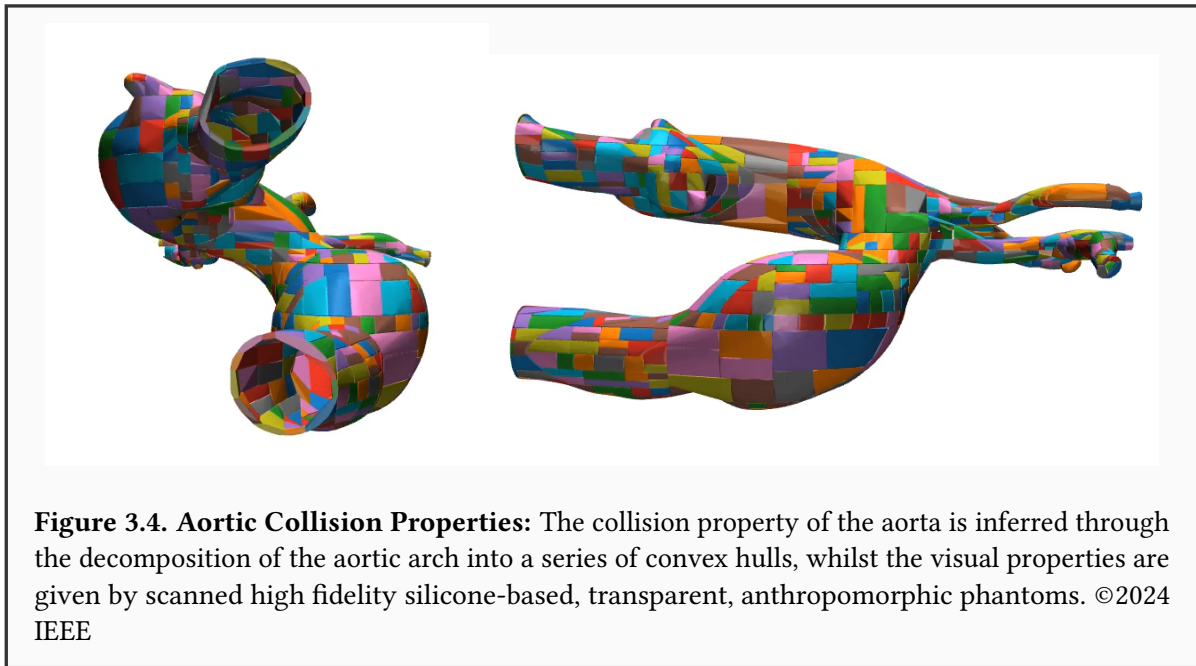


behaviour of the catheter involves frictional interaction, in which the clamps lock the catheter and rotate it during actuation. A similar mechanism is applied for linear displacement. However, due to the difficulty of accurately modelling friction-dependent rotation in simulation, a perfect motion assumption is made, and joint actuation is performed directly.

The follower component of the CathBot robot is simulated alongside the aortic arch phantoms and the catheter. These elements are modelled using the MuJoCo physics engine [136], selected for its stability, computational efficiency, and ability to support real-time interactions.

### 3.3.2 Aorta Simulation

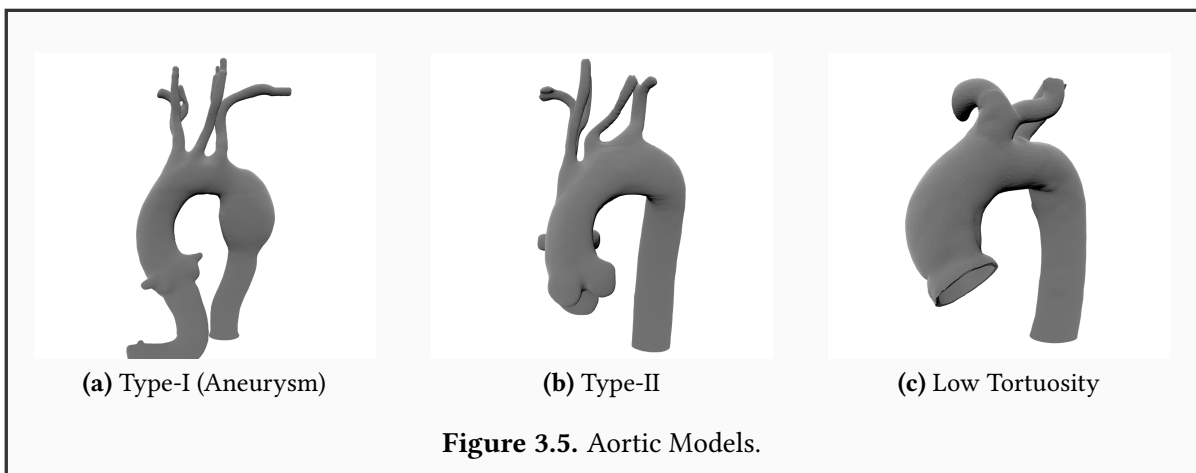
The aortic simulation is generated by scanning silicone-based, transparent, anthropomorphic phantoms of Type-I and Type-II aortic arch models (Elastrat Sarl, Switzerland) to produce high-fidelity 3D mesh models. These models are derived from postmortem vascular casts using methodologies described in [149, 150, 151], ensuring anatomical accuracy. The concave mesh is subsequently decomposed into a set of nearly convex surfaces using volumetric hierarchical approximate decomposition [152], resulting in 1,024 convex hulls for the Type-I aortic arch and 470 convex hulls for the Type-II aortic arch. The variation in the number of convex hulls corresponds to differences in the concavity of the two meshes [153]. Convex hulls are



employed for collision modelling, optimizing computational efficiency and enabling the use of soft contacts within the physics engine [136]. Figure 3.4 illustrates the aorta simulation.

### 3.3.2.1 Additional Aortic Models in CathSim

In addition to Type-I Aortic Arch model which is mainly used in our experiments, we incorporate three distinct aortic models to enrich our anatomical dataset. These models include a high-fidelity Type-II aortic arch and a Type-I aortic arch with an aneurysm, both sourced from Elastrat, Switzerland. Furthermore, a low tortuosity aorta model, based on a patient-specific CT scan, is included. With these three additional representations, our simulator contains four distinct aorta models. These models aim to enhance the diversity and accuracy of aortic structures available for research and educational endeavours. These aortas are visualized in Fig. 3.5.



### 3.3.3 Catheter Simulation

In the context of catheter design, curvature is considered critical for manoeuvrability and precise placement within complex anatomical paths. This curvature is modelled using quaternion differences to represent the relative orientations of catheter segments. For segments with orientations  $\mathbf{q}_i$  and  $\mathbf{q}_{i+1}$ , the curvature  $\boldsymbol{\kappa}$  is defined as:

$$\boldsymbol{\kappa} = \mathbf{q}_i^{-1} \mathbf{q}_{i+1} \quad (3.1)$$

Within this model, bending is prioritized over twisting. The bending energy  $E_{\text{bend}}$  is computed from the bending stiffness  $E$  and the deviation from the initial curvature  $\boldsymbol{\omega}_0$ :

$$E_{\text{bend}} = \frac{1}{2} E (\boldsymbol{\kappa} - \boldsymbol{\omega}_0)^2 \quad (3.2)$$

Accordingly, the total energy  $E_{\text{total}}$  of the catheter is expressed as:

$$E_{\text{total}} = E_{\text{bend}} \quad (3.3)$$

This formulation emphasizes the significance of bending behaviour in determining catheter effectiveness. The behaviour is influenced by the material properties, represented by  $E$  (Young's modulus [154], which defines the stiffness of the material), and the initial configuration  $\boldsymbol{\omega}_0$ . In this context, Young's modulus  $E$  denotes the ratio of stress to strain, indicating the extent of deformation experienced by the catheter under a specific load. The catheter itself can be visualized in Fig. 3.6

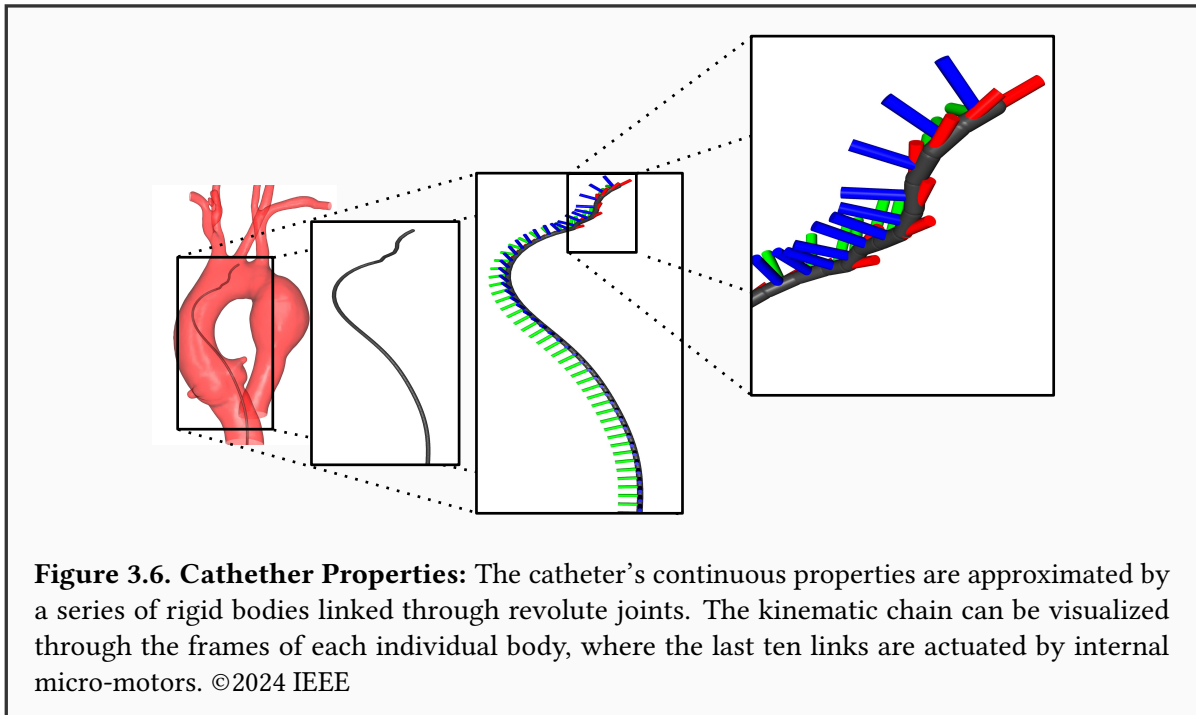
### 3.3.4 Contact Simulation

In the *CathSim* simulation, modelled using MuJoCo [136], the interaction between the aorta and catheter is represented through point contacts within a rigid body framework. Each contact point is defined by a spatial frame in a global coordinate system, where the primary axis is aligned with the contact normal—crucial for calculating normal forces—while the remaining axes define the tangent plane for frictional force computations. The contact distance, which determines whether objects are separated, in contact, or penetrating, influences the resulting contact force calculations.

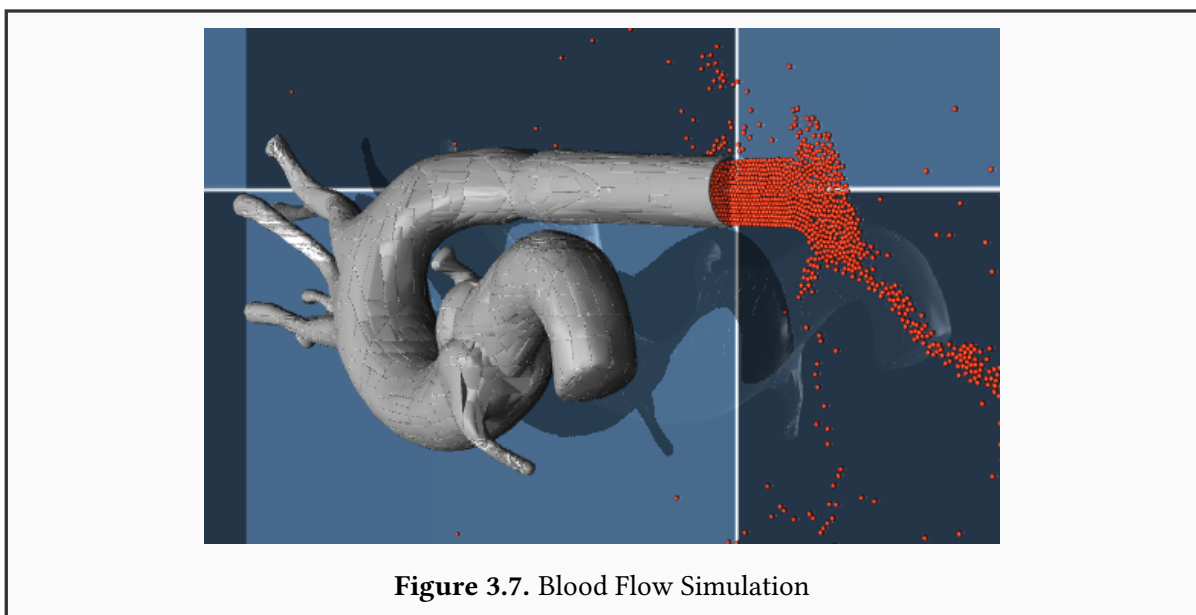
Within this rigid body model, dynamics are governed by the equation:

$$M\dot{v} + c = \tau + J^T f, \quad (3.4)$$

where  $M$  denotes the joint-space inertia,  $\dot{v}$  the acceleration, and  $c$  the bias force, which is



computed using the Recursive-Newton-Euler algorithm [155]. The applied force  $\tau$ , which includes components such as fluid dynamics and actuation forces, and the constraint Jacobian  $J$ , which relates joint and constraint coordinates, are used to determine force interactions at the contact points. The rigid body assumption streamlines the simulation by focusing on fundamental mechanical principles. Deformations and complex material behaviours are not considered, which ensures both computational efficiency and simulation fidelity [156, 157].



### 3.3.5 Blood Simulation

---

Although blood modelling is not the primary focus of the current work, a basic implementation is included for reference purposes. In this model, blood is treated as an incompressible Newtonian fluid, following the real-time methodology described in the study by Wei *et al.* [97] (see Fig. 3.7). The dynamics of a pulsating vessel are intentionally omitted, resulting in the simplification of assuming rigid vessel walls. This approach is commonly adopted in the field, as demonstrated in studies such as Behr *et al.* [86], Karstensen *et al.* [138], and Yi *et al.* [158], and serves to minimize computational demands while effectively simulating the forces that oppose guidewire manipulation.

## 3.4 RL for Autonomous Cannulation

The problem of autonomous cannulation is addressed by formulating it as an episodic **Partially Observable Markov Decision Process (POMDP)**. The agent, represented by the catheter, interacts with a continuous, partially observable environment  $\mathcal{E}$ , modelled on the anatomical structure of an aortic arch. At each time step  $t$ , an observation  $s_t$  is received that reflects the current state of the environment, and a continuous action vector  $a_t(s_t)$ , corresponding to motor actuation, is selected. A reward  $r_t(s_t, a_t)$  is then obtained based on the agent’s progress toward the goal, followed by a transition to a new state  $s_{t+1}$ .

The objective is to optimize a policy  $\pi(a|s)$  to guide the catheter through the aortic environment and reach the target position  $g \in \mathcal{G}$ . Each episode terminates either upon reaching the desired position or when predefined termination conditions, such as time limits, are met. This formulation enables adaptability to anatomical variability and accommodates uncertainties inherent in real-world interactions, such as partial observability and noisy sensor feedback.

Subsequent sections describe the components of this framework, including the observation modalities (*i.e.*, Internal, Image, and Sequential), the continuous action space, and the reward structure designed to promote efficient and accurate navigation of the catheter.

### 3.4.1 Observations

Three observation setups are evaluated: Internal, Image, and Sequential, each designed to provide varying levels of information to the RL agent.

The Internal setup delivers detailed proprioceptive data regarding the catheter’s state, including *position, velocity, centre of mass inertia, centre of mass velocity, and forces generated by both actuators and external interactions*. This rich dataset enables precise decision-making but assumes a complete internal understanding of the system.

The Image setup replicates clinical conditions by utilizing a virtual RGB camera placed above the aortic phantom. The resulting grayscale images, with a resolution of  $128 \times 128$ , are analogous to X-ray images commonly used during catheterization procedures. Although higher-resolution images were considered, no performance gains were observed in experiments, indicating that the computational and memory costs outweigh any marginal benefits.

The Sequential setup builds upon the Image modality by incorporating a temporal dimension. It combines three successive images  $\{s_{t-2}, s_{t-1}, s_t\}$  to capture motion and temporal patterns in the catheter’s behaviour. This approach improves the agent’s ability to infer dynamic information, thereby enhancing its capacity to navigate complex environments effectively.

These observation modalities were selected to explore the trade-offs between information

richness, temporal awareness, and computational efficiency.

### 3.4.2 Actions and Rewards

---

The agent’s actions are represented by a continuous vector  $a_t \in \mathbb{R}^{21}$ . Of these, the first 20 elements correspond to the motors that actuate the revolute joints within the catheter tip, while the final element controls the prismatic joint responsible for translational movement. To ensure consistency and prevent extreme outputs, the action values are normalized within the range  $[-1, 1]$ , resulting in an action space of  $a_t \in [-1, 1]^{21}$ .

To address the sparsity of rewards inherent in the navigation task, reward shaping is applied to provide the agent with additional spatial guidance. Specifically, the reward function incorporates the negative Euclidean distance  $-d(h, g) = \|h - g\|$ , where  $h$  denotes the position of the catheter tip and  $g$  represents the goal location. This formulation incentivizes the agent to minimize the distance to the target during its trajectory.

If the catheter tip reaches a goal region within a distance threshold  $\delta = 8$  mm of the target, the episode is terminated and a terminal reward of  $r = 10$  is provided. This threshold ensures full insertion of the catheter into the artery at the desired location. The reward function is defined as follows:

$$r(h_t, g) = \begin{cases} 10 & \text{if } d(h, g) \leq \delta \\ -d(h, g) & \text{otherwise} \end{cases} \quad (3.5)$$

Although this reward structure facilitates convergence by providing continuous feedback, it remains susceptible to local minima. For instance, the catheter may erroneously enter an unintended artery, thereby decreasing the distance to an incorrect but nearby target. In such cases, the agent must increase its distance from the incorrect location before reorienting toward the correct goal, thereby adding complexity to the optimization process.

### 3.4.3 Network Architectures

---

To handle the continuous action representation, two state-of-the-art RL algorithms are employed: [Proximal Policy Optimization \(PPO\)](#) [68] and [Soft Actor Critic \(SAC\)](#) [74]. The algorithm parameters are adopted from Dalal *et al.* [159].

The network architecture varies depending on the observation type. For the Internal observation, a [Multi-Layered Perceptron \(MLP\)](#)-based policy network is utilized, while for the Image and Sequential observations, a [Convolutional Neural Network \(CNN\)](#)-based policy network is applied. Following the methodology described by Mnih *et al.* [160], the same CNN architecture is used for both Image and Sequential observations, as these modalities differ only

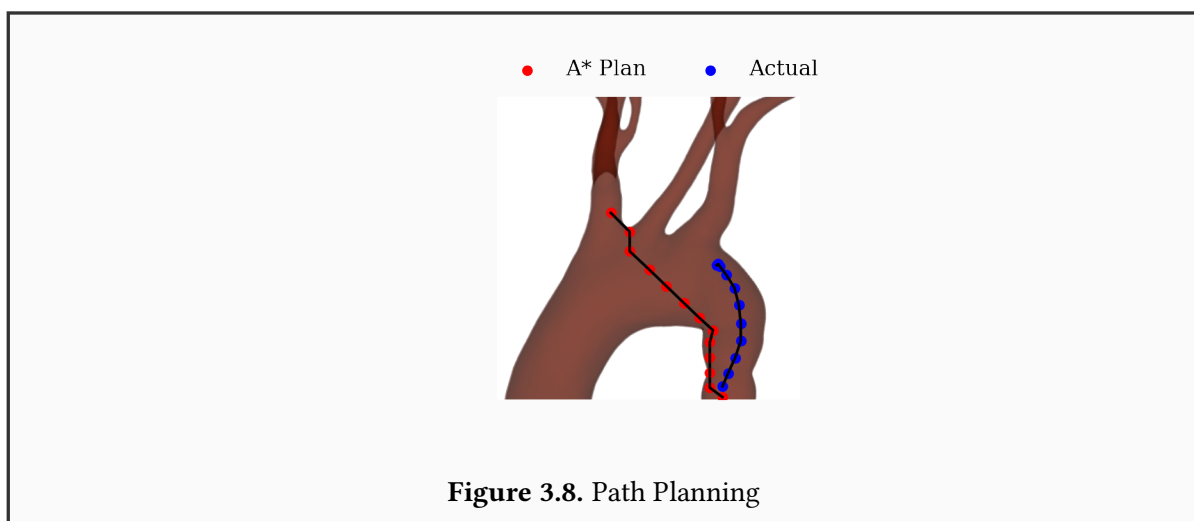
in the number of input channels—one for Image and four for Sequential, with each channel corresponding to a greyscale image.

The [MLP](#) policy network comprises an input layer, two hidden layers with 64 units each, and an output layer. All hidden layers use tanh activation functions. The final output layer is linear, producing the mean of the stochastic policy in the continuous action space  $\mathbb{R}^{21}$ .

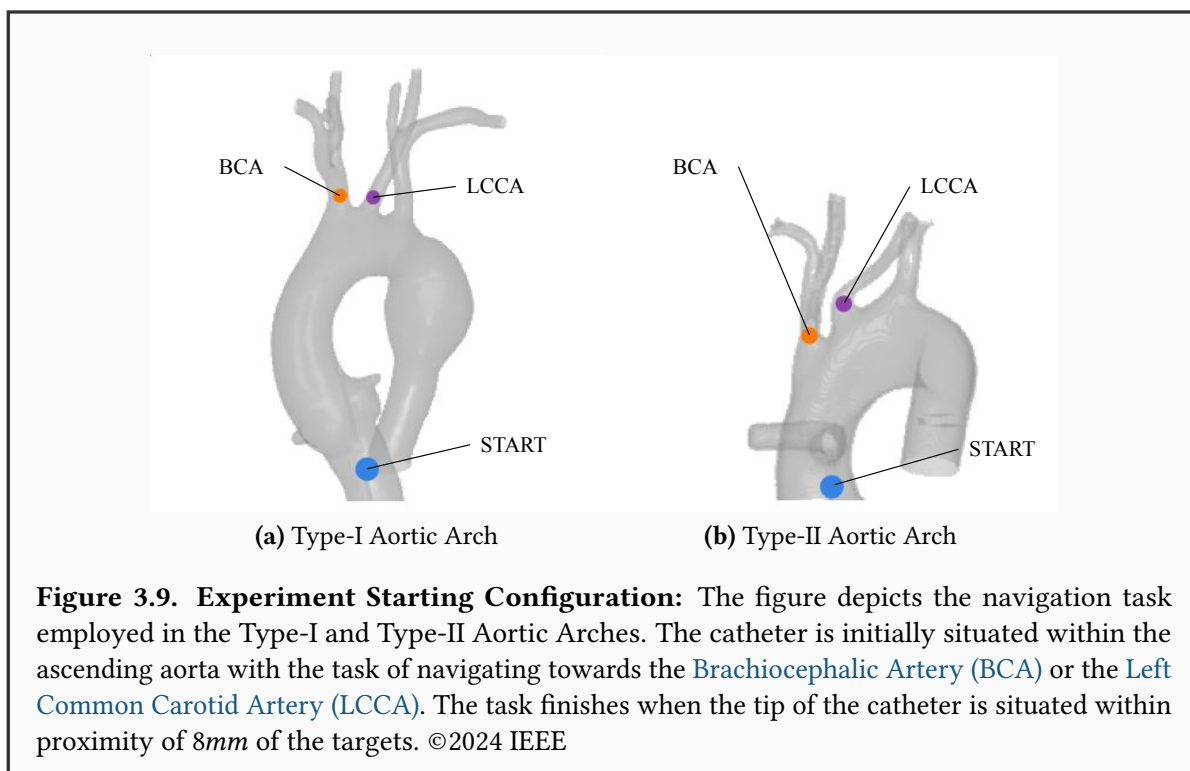
The [CNN](#) architecture consists of three convolutional layers: the first applies 32 filters of size  $8 \times 8$  with stride 4, the second uses 64 filters of size  $4 \times 4$  with stride 2, and the third uses 64 filters of size  $3 \times 3$  with stride 1. Each convolutional layer is followed by a ReLU activation. The output is flattened and passed through a fully connected layer with 512 units and ReLU activation, which then feeds into the final linear output layer that parameterizes the policy. All networks are trained using the [Adaptive Moment Estimation \(ADAM\)](#) optimizer with a fixed learning rate of 0.0003.

### 3.4.4 Traditional Path Planning

To emphasize our choice of using a neural network policy as the expert, we conducted a defining experiment. We initially used the A\* planner [161] to identify the most straightforward route from a starting position to the goal, ensuring sampling was restricted to the aortic arch. This plan is depicted in Fig. 3.8. However, the results revealed that the shortest path is not always the best. The cannulation efficiency along this route was suboptimal, and there was no standardized method to determine the exact actuation for the guidewire tip to follow this path. Expanding our research, we utilized a [MLP](#) to predict the next action from a sequence of observations. Yet, this model also faced difficulties in following the desired route, highlighting the intrinsic complexities of the task. The agent’s actual path, showing the guidewire’s deviation, can be seen below:



## 3.5 Experiments



In this section, comprehensive experiments are conducted to evaluate the performance and utility of the simulation framework, *CathSim*. The fidelity of *CathSim* is first verified by comparing its behaviour to that of the physical robotic system, *CathBot*, under similar conditions. This validation ensures that the simulator accurately replicates the dynamics and interactions observed in real-world settings.

Subsequently, the capability of *CathSim* to facilitate autonomous cannulation using state-of-the-art RL algorithms is demonstrated. Agents are trained within *CathSim* and evaluated based on their ability to navigate the catheter through anatomically realistic environments, such as Type-I and Type-II aortic arches, and achieve precise targeting of key arterial branches.

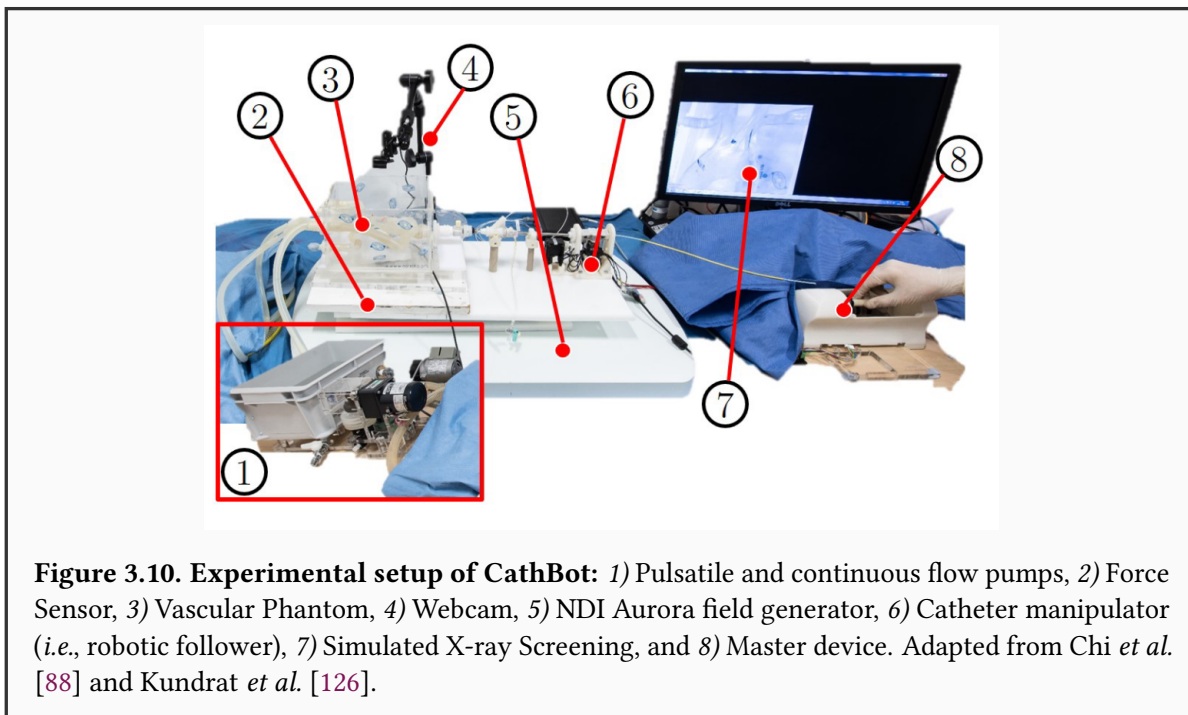
**Training Details.** All experiments were executed on a system equipped with an NVIDIA RTX 2060 GPU, running Ubuntu 22.04 LTS. The system was configured with an AMD Ryzen 7 5800X 8-Core Processor with 16 threads and 64 GB of RAM. All implementations were developed using PyTorch, and the RL algorithms were implemented using the Stable-Baselines3 library [162].

Each episode during training is associated with two terminal conditions:

- *Time-bound termination:* The episode is terminated once a predefined maximum number of steps is reached.

- *Goal-bound termination*: The episode is terminated when the agent successfully achieves the goal  $g$ , defined as the catheter tip reaching within 8 mm of the target location.

### 3.5.1 CathSim Validation



**CathSim vs. Real Robot Comparison.** To evaluate the accuracy of the simulator, force measurements from *CathSim* were compared to those obtained in real-world experiments. In the physical experiments [126], an ATI Mini40 load cell was used to measure interaction forces between the catheter and a Type-I silicone phantom, which was identical to the model used in the simulation. This force-based comparison was selected due to the lack of standardized quantitative metrics for evaluating endovascular simulators [163]. Figure 3.10 illustrates the experimental setup.

**Statistical Analysis.** To validate the similarity between the simulator and real-world systems, a statistical analysis was performed comparing the empirical force distributions from *CathSim* to those observed in the experiments by Kundrat *et al.* [126]. Based on the real-world measurements, a cumulative distribution (Fig. 3.11) was generated by sampling from a Gaussian distribution, which, due to its symmetry, also includes negative values. Although these negative forces are not physically meaningful, they arise naturally from the statistical modelling process and do not impact the validity of the comparison.

The Mann-Whitney U test was applied to determine whether the two distributions were statistically distinguishable. The test yielded a statistic of  $U = 76076$  and a p-value of  $p \approx 0.445$ , indicating that the observed differences were not statistically significant and were

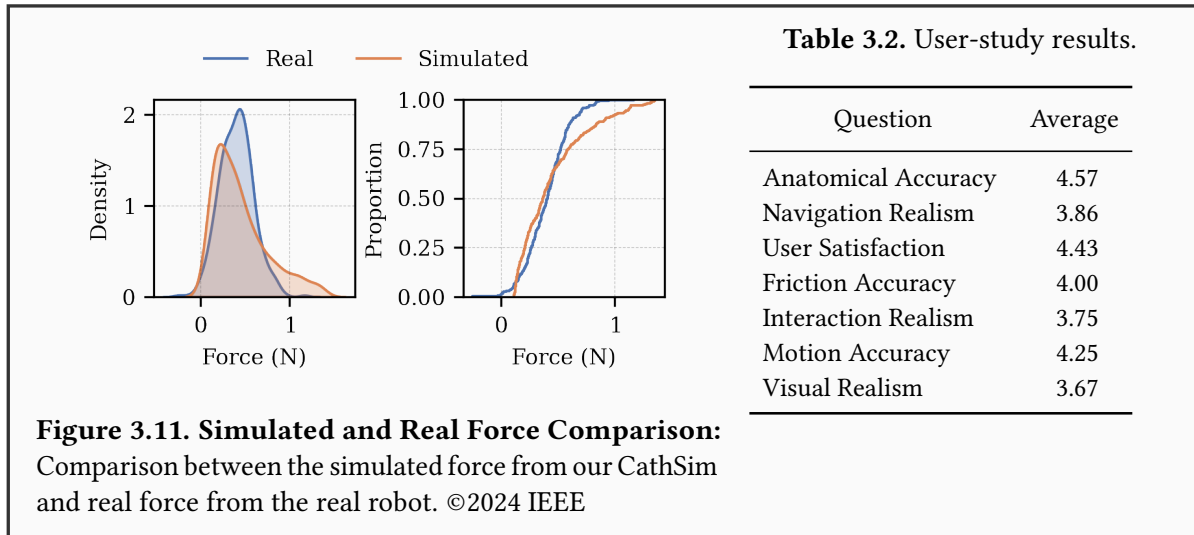
likely attributable to random variation. These results suggest that the force distributions from *CathSim* and the real-world system originate from the same population, confirming that *CathSim* accurately replicates the force interactions experienced in the physical robotic system.

**User Study.** To further validate the authenticity and effectiveness of *CathSim* as an endovascular simulator, a user study was conducted with 10 participants, all of whom were university students with no prior experience in endovascular navigation. The inclusion of novice users was intentional, aiming to assess the accessibility and intuitiveness of the simulator for individuals at the early stages of training. Participants were first shown a fluoroscopic video of an actual endovascular procedure to establish context, after which they interacted with *CathSim* by performing tasks such as cannulating the *BCA* and *LCCA*.

Upon completion, feedback was collected via a questionnaire in which participants rated *CathSim* across seven criteria using a 5-point Likert scale [164]:

1. *Anatomical Accuracy*: How effectively did the simulator replicate the anatomy and structure of blood vessels?
2. *Navigational Realism*: How closely did the simulator emulate the visual experience of a real endovascular procedure?
3. *User Satisfaction*: What was the level of satisfaction regarding the simulator's overall performance and functionality?
4. *Friction Accuracy*: How accurately did the simulation portray the resistance and friction of the guidewire against vessel walls?
5. *Interaction Realism*: How realistic were the visual depictions of the guidewire's interactions with the vessel walls?
6. *Motion Accuracy*: Did the motion of the guidewire align with expectations for a real guidewire's movement?
7. *Visual Realism*: How visually authentic was the guidewire simulation?

The results, summarized in Table 3.2, indicate positive feedback across all criteria. However, participants identified the visual experience of the simulator as an area requiring further improvement. The use of student participants, while enabling assessment of usability for novice users, may limit the generalizability of the findings to experienced clinicians. Nevertheless, this cohort provides valuable insight into the simulator's learnability and initial user engagement, which are critical for training applications.



## 3.5.2 Reinforcement Learning Results

### 3.5.2.1 Setup

Autonomous catheterization was performed on two principal arteries within the aortic arch: the [Brachiocephalic Artery \(BCA\)](#) and the [Left Common Carotid Artery \(LCCA\)](#). For both configurations, the catheter tip was positioned at a predefined starting location within the ascending aorta, and training was terminated once full insertion into the target artery was achieved. The procedure was identical for both Type-I and Type-II aortic arches. [Figure 3.9](#) illustrates the experimental setup.

The model was trained for a total of  $6 \times 10^5$  time steps. Each episode was initialized with a random catheter displacement of 1 mm, followed by navigation through the ascending aorta to the designated target. Episodes were terminated either upon successful insertion into the target artery or after exceeding a limit of 2,000 steps. During training, data on contact points and exerted forces were collected at every time step, with forces computed according to [Eq. 3.6](#), enabling the generation of force heatmaps overlaid on RGB virtual images.

The model's performance was evaluated over 30 episodes. The maximum and mean forces exerted during  $n$  samples were calculated as follows:

$$f_{\max} = \max_{t \in n} f_t, \quad f_{\text{mean}} = \frac{1}{n} \sum_{t=1}^n f_t \quad (3.6)$$

The training time varied depending on the algorithm. [PPO](#) completed training in approximately 1 hour, whereas [SAC](#) required 8 hours, making [PPO](#) approximately five times faster. Despite the difference in training time, the simulator maintained a performance rate of 60 FPS in the image-based environment and 80 FPS in the internal-based environment.

### 3.5.3 Force Analysis

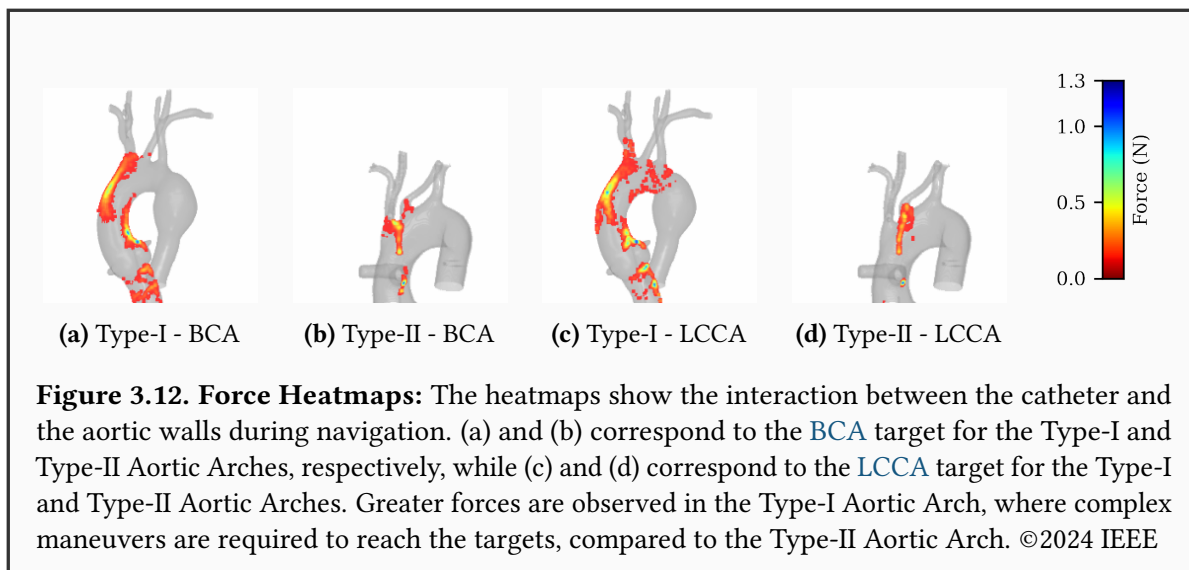


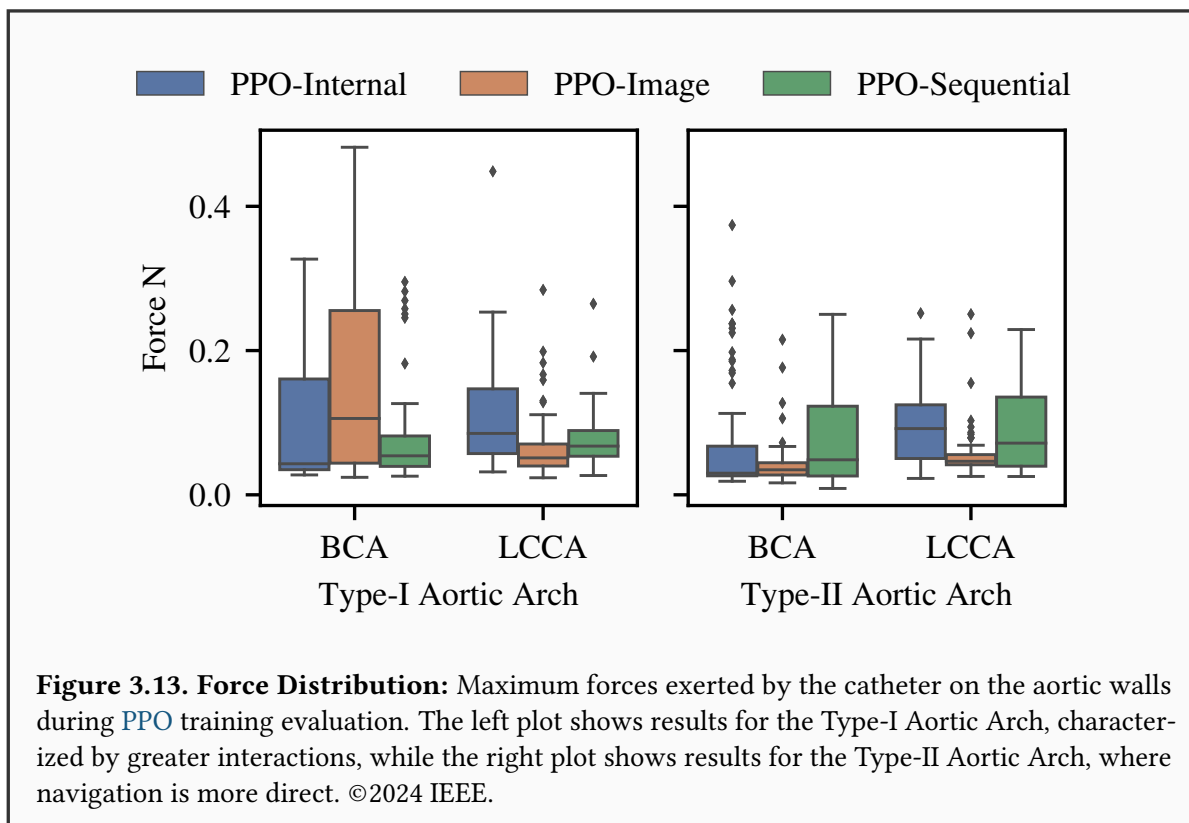
Figure 3.12 illustrates the force heatmaps derived from catheter interactions with the aortic walls during navigation. Subfigures (a) and (b) represent navigation toward the **BCA** target for the Type-I and Type-II aortic arches, respectively, while (c) and (d) correspond to navigation toward the **LCCA** target for the same anatomical variations. These heatmaps offer insights into the dynamics of catheter-aorta interactions, revealing variations in force intensity and distribution as a function of aortic arch morphology.

- *Type-I Aortic Arch:* More complex manoeuvres were required during navigation, resulting in increased forces exerted on the aortic walls, particularly at bends.
- *Type-II Aortic Arch:* Navigation involved less complex trajectories, leading to lower force interactions between the catheter and vessel walls.

Figure 3.13 presents an analysis of the force interactions by depicting the maximum forces exerted during evaluation episodes for **PPO**. The relationship between anatomical configuration and the catheter's interaction dynamics is revealed as follows:

- In the *Type-I Aortic Arch* (left), navigation required increased reliance on vessel walls for intricate manoeuvres, resulting in higher exerted forces.
- In the *Type-II Aortic Arch* (right), navigation followed more direct paths, leading to overall lower interaction forces.

Most force values across both arch types were observed within the 0.0 to 0.2 N range. However, outliers exceeding 0.4 N were present. This force range is reasonable for vascular interventions, as forces below 0.2 N are typically sufficient for catheter manipulation without risking vessel damage, while occasional higher forces up to 0.4 N may occur during challenging navigational segments or in areas of increased vessel tortuosity [165]. Notably, the **BCA** within the Type-I



Aortic Arch exhibited a wider interquartile range compared to the LCCA, indicating greater variability in force interactions during BCA targeting.

This analysis underscores the influence of anatomical variations on catheterization dynamics. The Type-I Aortic Arch presents greater challenges, requiring higher forces for complex navigation manoeuvres when compared to the more straightforward pathways in the Type-II Aortic Arch.

Table 3.3. Results Summary

| Aorta   | Observation    | Reward       |           |                      | Mean Force ( $N \downarrow$ ) |                      |                      | Max Force ( $N \downarrow$ ) |           |      | Success % |     |      |
|---------|----------------|--------------|-----------|----------------------|-------------------------------|----------------------|----------------------|------------------------------|-----------|------|-----------|-----|------|
|         |                | BCA          | LCCA      | BCA                  | BCA                           | LCCA                 | LCCA                 | BCA                          | BCA       | LCCA | LCCA      | BCA | LCCA |
| Type-I  | PPO-Internal   | -70 ± 28     | -154 ± 66 | 0.011 ± 0.021        | 0.008 ± 0.015                 | 0.121 ± 0.095        | 0.123 ± 0.089        | 53                           | 7         |      |           |     |      |
|         | SAC-Internal   | -54 ± 36     | -158 ± 83 | 0.007 ± 0.014        | 0.006 ± 0.015                 | 0.059 ± 0.047        | 0.095 ± 0.039        | 77                           | 7         |      |           |     |      |
|         | PPO-Image      | -65 ± 52     | -140 ± 96 | <b>0.005 ± 0.007</b> | 0.007 ± 0.016                 | <b>0.048 ± 0.020</b> | 0.076 ± 0.059        | 83                           | <b>37</b> |      |           |     |      |
|         | SAC-Image      | -391 ± 157   | -196 ± 5  | 0.024 ± 0.035        | <b>0.003 ± 0.003</b>          | 0.258 ± 0.094        | <b>0.059 ± 0.028</b> | 0                            | 0         |      |           |     |      |
| Type-II | PPO-Sequential | -57 ± 36     | -336 ± 55 | 0.006 ± 0.009        | 0.010 ± 0.015                 | 0.045 ± 0.022        | 0.094 ± 0.036        | <b>97</b>                    | 0         |      |           |     |      |
|         | SAC-Sequential | -200 ± 20    | -227 ± 12 | 0.003 ± 0.003        | 0.003 ± 0.003                 | 0.043 ± 0.009        | 0.061 ± 0.022        | 0                            | 0         |      |           |     |      |
|         | PPO-Internal   | -52 ± 48     | -22 ± 30  | 0.016 ± 0.023        | 0.011 ± 0.015                 | 0.118 ± 0.103        | 0.068 ± 0.040        | 50                           | 87        |      |           |     |      |
|         | SAC-Internal   | <b>0 ± 0</b> | -67 ± 30  | 0.014 ± 0.010        | 0.010 ± 0.016                 | <b>0.030 ± 0.007</b> | 0.121 ± 0.044        | <b>100</b>                   | 27        |      |           |     |      |
| Type-II | PPO-Image      | -20 ± 47     | -8 ± 10   | 0.017 ± 0.025        | 0.015 ± 0.022                 | 0.046 ± 0.047        | 0.066 ± 0.054        | 87                           | <b>97</b> |      |           |     |      |
|         | SAC-Image      | -68 ± 91     | -54 ± 7   | <b>0.004 ± 0.005</b> | <b>0.005 ± 0.005</b>          | 0.042 ± 0.013        | <b>0.050 ± 0.008</b> | 73                           | 3         |      |           |     |      |
|         | PPO-Sequential | -47 ± 49     | -80 ± 92  | 0.011 ± 0.017        | 0.011 ± 0.018                 | 0.068 ± 0.059        | 0.066 ± 0.050        | 57                           | 67        |      |           |     |      |
|         | SAC-Sequential | -99 ± 18     | -85 ± 15  | 0.005 ± 0.007        | 0.006 ± 0.008                 | 0.055 ± 0.017        | 0.100 ± 0.023        | 3                            | 0         |      |           |     |      |

### 3.5.4 Quantitative Results

---

Table 3.3 summarizes the performance of all evaluated methods in terms of force, reward, and success rate. In experiments conducted on the Type-I Aortic Arch, PPO with sequential observations yielded the highest reward when cannulating the BCA target, although a significant decline in performance was observed when targeting the LCCA. In contrast, the use of singular image observations produced more consistent rewards, with cannulation of the LCCA achieving the highest success rate (37%) and the BCA cannulation success rate (83%) closely matching that of the sequential observation setup.

The observed performance disparity between BCA and LCCA cannulation can be attributed to anatomical differences within the aortic arch. As shown in Fig. 3.9, the BCA is positioned closer to the initial navigation direction, making it more accessible for both human operators and reinforcement learning agents. In contrast, the LCCA is located further along the navigation path and is surrounded by additional vascular branches, thereby increasing task complexity.

Cannulation within the Type-II Aortic Arch was found to be comparatively more straightforward, as reflected by higher success rates across all evaluated methods. The reduced reliance on vessel walls during navigation enabled smoother catheterization. This trend is further illustrated in Fig. 3.12, where lower forces were exerted on the aortic walls in the Type-II configuration compared to the Type-I arch.

Overall, the results indicate that PPO outperformed SAC in autonomous cannulation tasks, particularly when image-based observations were employed.

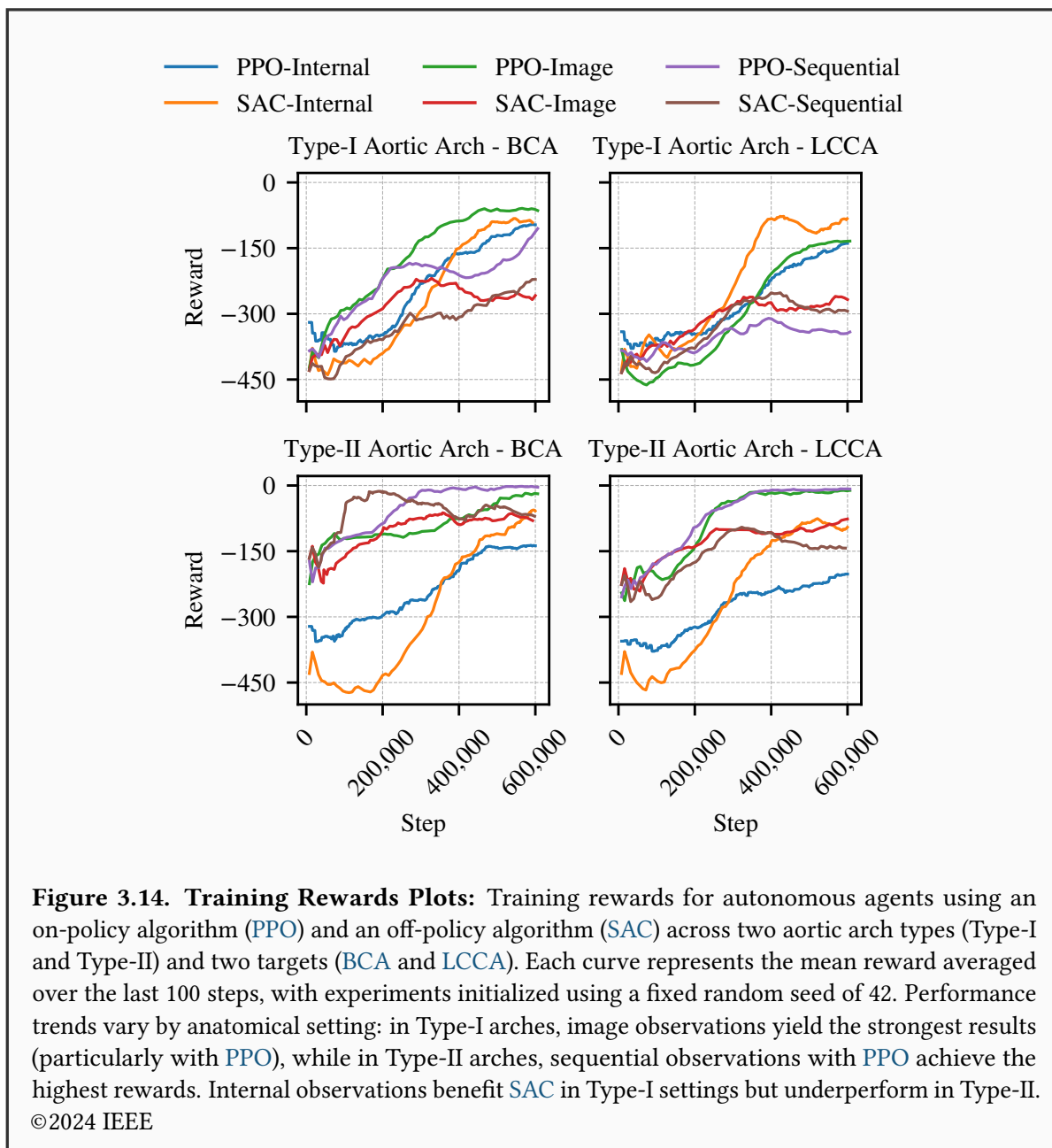
### 3.5.5 Rewards Analysis

---

At each time step, the mean reward over the last 100 steps was computed, with results presented in Fig. 3.14. Both PPO and SAC exhibited stable learning behaviour with gradual improvements and eventual signs of convergence. The relative performance, however, varied considerably depending on the aortic arch type, target, and observation modality.

In the Type-I aortic arch, PPO with image observations achieved the highest reward for the BCA target, followed closely by SAC with internal observations. For the LCCA target, SAC with internal observations achieved the best results, slightly outperforming PPO with image observations. Across both targets in Type-I arches, sequential observations (particularly with PPO) consistently ranked lowest, suggesting that they fail to provide the necessary representational richness for reliable navigation.

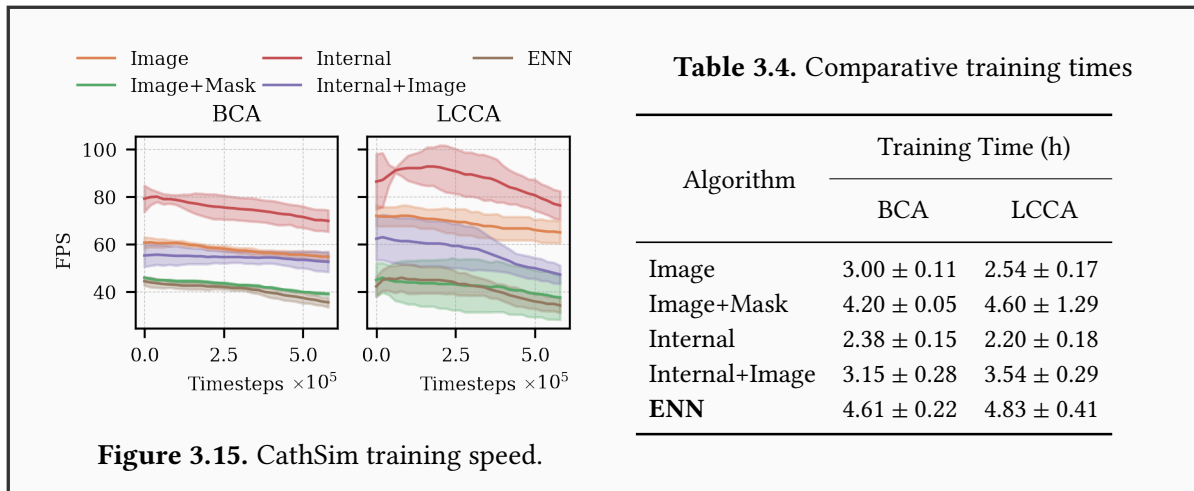
In contrast, the Type-II aortic arch revealed a different trend. For both BCA and LCCA, PPO with sequential observations achieved the highest reward, surpassing all other settings. PPO with image observations remained competitive, consistently ranking second. By comparison,



PPO with internal observations consistently performed worse across both targets in Type-II arches, indicating that internal-only states are insufficient to capture the greater anatomical complexity of these geometries.

Taken together, these results highlight that the most effective algorithm–observation pair depends on the vascular configuration. Image-based observations are advantageous in Type-I arches, particularly when paired with PPO, while sequential observations become critical for Type-II arches, where they enable PPO to achieve the best performance. Internal observations favour SAC in Type-I settings, but degrade performance when paired with PPO in Type-II anatomies. These findings emphasize the importance of tailoring both the learning algorithm and the observation space to the anatomical context in order to maximize performance.

### 3.5.6 CathSim Speed Evaluation



As illustrated in Fig. 3.15, we provide a comparison of frames per second (FPS) for the various algorithms we employed during model training. It is evident that utilizing solely the internal state space, comprised of joint positions and velocities, facilitates expedited training processes. In contrast, integrating all modalities into the training process results in its deceleration. The most significant computational demand arises from the dual convolutional neural networks utilized in both the image and mask representations. However, despite this load, the algorithms exhibit respectable computational speed, even during the training phase. Our simulator supports approximately 40 to 80 frames per second performance for all implemented algorithms, underscoring the computational speed of our simulation environment. Moreover, we provide the training times in terms of hours for the different modalities in Table 3.4.

## 3.6 Discussion and Conclusions

CathSim has been introduced as an open-source simulation environment designed to function as a comprehensive benchmarking platform for autonomous endovascular navigation. Through the development and evaluation of diverse algorithms for autonomous cannulation, CathSim eliminates the reliance on physical robotic systems, thereby mitigating the risks and costs typically associated with experimental hardware. The simulator is intended to serve a dual purpose: to provide researchers with a robust environment for algorithm development and evaluation, and to offer healthcare professionals a risk-free platform for skill acquisition and procedural refinement.

Given the rapid advancements in medical robotics, the need for controlled and flexible simulation environments has become increasingly apparent. This need is effectively addressed by CathSim, which enables the testing and optimization of novel procedures and techniques prior to clinical deployment. Furthermore, the open-source nature of CathSim encourages collaborative innovation and facilitates knowledge sharing across both scientific and medical communities.

Planned future enhancements – including the integration of deformable anatomical models, improvements in imaging fidelity, and the development of more realistic real-time interaction dynamics – are expected to further strengthen CathSim as a pivotal tool bridging the gap between simulation and clinical practice. By addressing these challenges, CathSim holds the potential to significantly advance the field of autonomous endovascular navigation and to contribute meaningfully to medical robotics, surgical training, and healthcare education. The simulation environment developed in this chapter serves as the foundation for the Expert Navigation Network presented in the next chapter, which leverages CathSim’s multimodal data to enhance navigation precision.

## Chapter 4

---

# Expert Network for Autonomous Navigation

*Endovascular robots have been actively developed in both academic and industrial contexts. However, progress toward autonomous catheterization has often been hindered by the absence of robust navigation strategies capable of generalizing across diverse anatomical and procedural variations. Furthermore, the acquisition of large-scale datasets for training machine learning algorithms in endovascular navigation remains largely infeasible due to the complexity of medical procedures and the scarcity of expert demonstrations. In this chapter, an Expert Navigation Network (ENN) is introduced as a multimodal framework designed to address these challenges. ENN emphasizes real-time adaptability and leverages multimodal data sources to enhance decision-making and navigation performance. Validation is performed using a combination of simulated and real-world robotic setups, demonstrating superior performance compared to traditional navigation approaches in complex endovascular tasks. The experimental results indicate that ENN holds strong potential for advancing research in autonomous endovascular navigation, serving as a bridge between simulation and real-world application.*

This chapter presents the work from the following publication:

**Jianu, T.** *et al.*, “Autonomous catheterization with open-source simulator and expert trajectory,” in *Handbook of Robotic and Image-Guided Surgery, 2nd Edition*, Nasab, M. H. A., Ed., 2nd ed., Elsevier, 2025, ISBN: 9780443139123

## 4.1 Introduction

Endovascular interventions are widely employed for diagnosing and treating various vascular diseases. These procedures utilize flexible instruments such as guidewires and catheters, which are introduced into the body through small incisions and guided manually through the vascular system to reach target regions, including the heart or brain [124]. Navigation of endovascular tools accounts for approximately 70% of the total intervention time and is applied in the treatment of conditions such as Peripheral Artery Disease (PAD), aneurysms, and stenosis [167]. Endovascular techniques offer significant advantages over traditional open surgery, including reduced recovery times, lower levels of pain and scarring, and a decreased risk of complications [124]. Despite these benefits, surgeons must rely on monoplanar X-ray imaging for visual feedback, which introduces operational challenges. Consequently, prolonged exposure to occupational hazards such as radiation and orthopaedic strain is common. Moreover, manual manipulation of guidewires and catheters requires advanced surgical expertise, while the absence of haptic feedback and limited visualization hinder precision during these procedures [168].

In response to these limitations, robotic systems have been developed to assist surgeons during endovascular procedures [126]. These systems allow for remote operation, thereby reducing direct exposure to intraoperative hazards [169]. However, most current systems operate on a follower-leader (master-slave) architecture, in which the surgeon retains full control of navigation [170]. Furthermore, manually operated robotic systems impose high cognitive demands and are frequently associated with longer procedural durations when compared to traditional non-robotic techniques [171]. As such, the development of autonomous solutions for endovascular tasks has emerged as a critical area of research.

Autonomous catheterization, an evolving challenge within the [Machine Learning \(ML\)](#) domain, has motivated the introduction of an expert trajectory solution as a robust baseline. Expert trajectories encapsulate the complexity of surgical procedures and provide a structured framework for training autonomous systems [172]. Through [Imitation Learning \(IL\)](#), these systems are able to replicate expert behaviour with high fidelity, thereby accelerating the transition from novice to proficient interventionist. *CathSim* offers a dynamic and safe simulation environment that enables autonomous agents to iteratively refine their performance through expert-guided actions [173]. Experimental results have shown that expert-guided learning in simulation substantially improves downstream [ML](#) tasks related to autonomous catheterization, including [IL](#) and force prediction. This contribution includes an expert trajectory network along with a novel set of evaluation metrics designed to assess its performance in such tasks. These advancements aim to extend the capabilities of [ML](#) in the context of autonomous medical interventions.

## 4.2 Related Work

**Autonomous Catheterization.** Recent advancements in [ML](#) have facilitated notable progress in autonomous catheterization, particularly in foundational methodologies and early-stage implementations. Initial research efforts were directed toward supportive functionalities, including image processing and basic motion planning [174]. Over time, a transition toward higher levels of autonomy has been observed, with semi-autonomous navigation representing a key area of focus [98]. A number of studies have adopted deep [Reinforcement Learning \(RL\)](#) approaches [86, 91, 125, 138, 140, 175], often utilizing fluoroscopic images to guide navigation and decision-making [176].

Despite the increasing prevalence of [RL](#), alternative algorithmic strategies have also been explored. For instance, deterministic navigation along vascular centrelines has been demonstrated using the Dijkstra algorithm [99], as applied in studies such as [142, 145, 177]. Other studies have employed Breadth-First Search (BFS) to enable efficient exploration of vascular structures [100]. While these approaches have shown promise, much of the current work remains limited to lower levels of autonomy [98], often constrained by the use of physical test beds or closed-source simulation platforms.

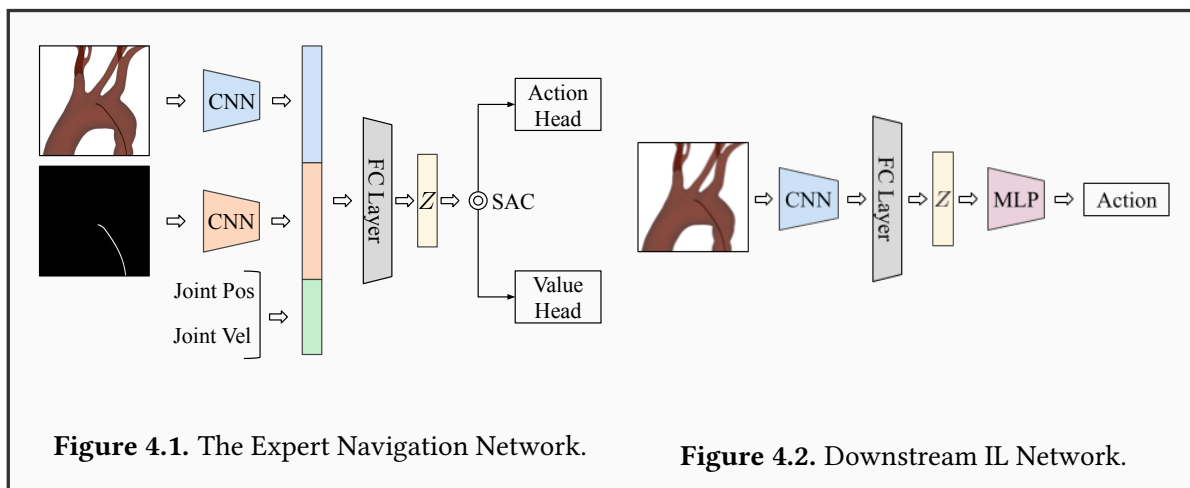
**Imitation Learning.** Advances in [RL](#) have led to the emergence of [IL](#) techniques that leverage human demonstrations for policy learning [101]. These techniques have proven especially valuable in complex, dynamic environments such as surgical tasks involving anatomically variable conditions. Applications of [IL](#) in robotics have included navigation in unstructured environments and precise object manipulation [178, 179].

Demonstration-based methods have been widely studied in the context of endovascular navigation [88, 102, 103, 180, 181], with early work incorporating hidden Markov models and dynamical movement primitives [182]. More recent frameworks have adopted [Generative Adversarial Imitation Learning \(GAIL\)](#) to improve generalization and policy robustness [101]. By leveraging insights from [Deep Reinforcement Learning \(DRL\)](#), surgical autonomy is increasingly moving toward task-level autonomy, where decision-making responsibilities are shared between human operators and robotic systems under supervised control [104].

## 4.3 Autonomous Navigation with Expert Navigation Network

Drawing inspiration from the domains of autonomous driving and human-robot interaction [172, 183], an expert navigation network is proposed to support downstream tasks in autonomous endovascular interventions. Using *CathSim* [123], a substantial dataset of labelled training samples is generated, enabling the model to learn from a broad range of simulated scenarios that reflect diverse procedural variations. This exposure to varied procedural contexts enhances the model’s capacity to generalize navigation strategies to real-world applications [184].

In addition, data that is typically unavailable in real-world systems, such as force measurements [185] and shape representations [186], are incorporated to improve the robustness and precision of the expert navigation system [170]. The simulation environment offers a comprehensive set of sensing modalities, including force feedback and shape representation, which are absent in clinical endovascular procedures where surgeons rely solely on X-ray imaging. By integrating these advanced modalities, the expert navigation system is designed to deliver both high navigation accuracy and enhanced sample efficiency, thereby optimizing learning performance under minimal data requirements.



### 4.3.1 Expert Navigation Network

The **Expert Navigation Network (ENN)** is implemented as a *multimodal* learning architecture trained within *CathSim*, designed to integrate multiple input types to improve navigation accuracy.

**Segmentation Input.** The first input modality consists of semantic segmentation of the guidewire, offering pixel-level information about its position and shape within the environ-

ment. This modality enables precise perception of the guidewire’s configuration, thereby facilitating safe and controlled navigation through vascular pathways.

**Kinematic Input.** The second input modality comprises the guidewire’s joint positions and velocities, which represent its kinematic and dynamic behaviour [187]. These parameters contribute to smoother and more efficient navigation compared to previously proposed approaches [188, 189].

**Visual Input.** The third modality incorporates images captured from a top-view camera, offering a visual perspective of the navigation environment. This input provides essential contextual information, enabling the identification of vessel structures and the detection of obstacles that may impact navigation [145].

**Multimodal Feature Fusion.** A [Convolutional Neural Network \(CNN\)](#) is employed to extract high-level visual features from both the segmentation maps and top-view images. In parallel, a [Multi-Layered Perceptron \(MLP\)](#) processes the joint positions and velocities to encode kinematic information related to the guidewire. The resulting feature maps are flattened to reduce dimensionality and subsequently concatenated to form a unified representation of the multimodal data. This combined representation is then passed through an [MLP](#), which maps the input to a compact feature vector  $Z$  that encapsulates the sensory modalities required for trajectory learning.

**Policy Learning.** By integrating these diverse modalities, the expert navigation network learns the complex mapping between multimodal sensory inputs and the guidewire’s desired trajectory. The resulting feature vector  $Z$  is used to train a [Soft Actor Critic \(SAC\)](#) policy  $\pi$  [74], which serves as the decision-making component within the broader [RL](#) framework. An overview of the complete architecture, including modality integration and the training pipeline, is depicted in Fig. 4.1.

**Experimental Setup.** The experiments were conducted on a system equipped with an NVIDIA RTX 2060 GPU (33MHz) and Ubuntu 22.04 LTS as the operating system. The system also featured an AMD Ryzen 7 5800X 8-core processor with 16 threads and 64GB of RAM. All experiments were implemented using PyTorch, and the [SAC](#) algorithm was executed via the Stable-Baselines3 library [162]. Training was carried out for  $6 \times 10^5$  time steps across 5 random seeds, with training durations ranging from 2 to 5 hours depending on computational load and task complexity.

Each episode was terminated upon satisfying one of two conditions: a time-bound limit (termination after a fixed number of steps), or a goal-bound condition (successful achievement of the goal  $g \in G$ ).

**Table 4.1. The network architectures for ENN:** The CNN is utilized to extract the image-based features (*i.e.*, grayscale image and binary mask) whilst the MLP is used to extract the internal features (*i.e.*, joint positions and joint velocities)

| Network | Layer (type) | Output Shape | Param # | Nonlinearity | Kernel | Stride | Padding |
|---------|--------------|--------------|---------|--------------|--------|--------|---------|
| CNN     | Input        | (1, 80, 80)  | 0       | —            | —      | —      | —       |
|         | Conv2D       | (32, 19, 19) | 2,080   | ReLU         | 8      | 4      | 0       |
|         | Conv2D       | (64, 8, 8)   | 32,832  | ReLU         | 4      | 2      | 0       |
|         | Conv2D       | (64, 6, 6)   | 36,928  | ReLU         | 3      | 1      | 0       |
|         | Flatten      | (2304)       | 0       | —            | —      | —      | —       |
|         | Linear       | (256)        | 590,080 | ReLU         | —      | —      | —       |
|         | Linear       | (128)        | 32,896  | ReLU         | —      | —      | —       |
| MLP     | Input        | (1, 336)     | 0       | —            | —      | —      | —       |
|         | Linear       | (256)        | 86,272  | ReLU         | —      | —      | —       |
|         | Linear       | (128)        | 32,896  | ReLU         | —      | —      | —       |

**Table 4.2. SAC hyperparameters**

| Hyperparameter                   | Value              |
|----------------------------------|--------------------|
| Learning Rate                    | $3 \times 10^{-4}$ |
| Buffer Size                      | $10^6$             |
| Batch Size                       | 256                |
| Smoothing Coefficient ( $\tau$ ) | 0.005              |
| Discount ( $\gamma$ )            | 0.99               |
| Train Frequency                  | 1                  |
| Gradient Steps                   | 1                  |
| Entropy Coefficient              | 1                  |
| Target Update Interval           | 1                  |
| Target Entropy                   | -2                 |

**Networks.** Multiple feature extractors are utilized within the ENN to isolate and process key multimodal inputs, enabling efficient representation learning. A CNN [63] is employed to extract image-based features, producing two latent feature representations,  $J_I$  and  $J_S$ , corresponding to the top-view camera image and the guidewire segmentation map, respectively. The CNN comprises three convolutional layers, each followed by a ReLU activation function [190], and a final flattening operation to prepare the features for downstream processing. Concretely, we use a Nature-CNN configuration with kernels ( $8 \times 8$ ,  $4 \times 4$ ,  $3 \times 3$ ), strides (4, 2, 1), and channel widths 32–64–64, followed by a fully connected projection to a 256-dimensional embedding for each image stream, yielding  $J_I, J_S \in \mathbb{R}^{256}$ .

Joint positions  $Q$  and joint velocities  $V$  are concatenated to form a joint feature vector  $J_J = Q \parallel V$  with a dimensionality of 336, which is subsequently processed by a MLP. This dimensionality arises from concatenating  $n_Q = 168$  joint position variables and  $n_V = 168$  joint

velocity variables as defined in the MuJoCo model. The extracted features  $J_I$ ,  $J_S$ , and  $J_J$  are concatenated to form a unified feature vector  $J = J_I \parallel J_S \parallel J_J$ , which serves as input to the policy network  $\pi(a_t, \theta)$  responsible for decision-making and trajectory generation. Detailed specifications of the CNN and MLP architectures, including layer parameters, are provided in Table 4.1.

**SAC.** The primary RL algorithm used is SAC [74], selected for its ability to balance exploration and exploitation in stochastic environments. SAC is a model-free algorithm that concurrently learns a stochastic policy and a value function. Its objective function combines the policy’s expected return with an entropy term, thereby promoting exploration while avoiding premature convergence to suboptimal policies.

The algorithm maintains three networks: a state-value function  $V$ , parameterized by  $\psi$ , which estimates the value of a given state; a soft  $Q$ -function  $Q$ , parameterized by  $\theta$ , which evaluates the value of state-action pairs; and a policy network  $\pi$ , parameterized by  $\phi$ , which defines the action distribution. The policy network consists of linear layers structured to effectively map the fused feature vector  $J$  to the action space. Parameter configurations used for training with SAC are listed in Table 4.2.

### 4.3.2 Downstream Tasks

The effectiveness of the ENN and the *CathSim* simulator is demonstrated through downstream tasks such as IL and force prediction. These tasks are of practical relevance, as they provide critical support and insights for surgeons during real-world endovascular procedures.

**Imitation Learning.** The ENN is applied in conjunction with Behavioural Cloning (BC), a supervised form of IL [191], to train a navigation policy. This approach highlights the capability of the simulation environment to extract meaningful representations that can be leveraged in downstream learning tasks.

Initially, expert trajectories are generated by executing the expert policy  $\pi_{\text{exp}}$  within the *CathSim* simulator. These trajectories serve as labelled training data, specifying the optimal actions for each encountered state during the navigation process. To emulate conditions consistent with real-world clinical scenarios, the image modality is used as the sole input for training.

Subsequently, the BC algorithm is trained to replicate the expert’s actions based on these input observations. This is accomplished by optimizing the policy parameters  $\theta$  to minimize the discrepancy between expert and predicted actions using the following loss function:

$$\mathcal{L}(\theta) = -\mathbb{E}_{\pi_{\theta}}[\log \pi_{\theta}(a|s)] - \beta H(\pi_{\theta}(a|s)) + \lambda \|\theta\|_2^2, \quad (4.1)$$

where  $-\mathbb{E}_{\pi_\theta}[\log \pi_\theta(a|s)]$  denotes the negative log-likelihood of the expert actions given the observed states. The term  $-\beta H(\pi_\theta(a|s))$  introduces an entropy penalty, encouraging exploration and diversity in action selection, weighted by  $\beta$ . The final term,  $\lambda \|\theta\|_2^2$ , applies  $L_2$  regularization to mitigate overfitting, weighted by  $\lambda$ .

To support the learning process, the feature space  $Z$ , extracted from the expert policy, is used to train the BC. Concretely, the CNN comprises three convolutional blocks (Conv2D–ReLU–max pooling); the resulting feature maps are flattened and passed through a fully connected projection to form the latent variable  $Z$ . A subsequent policy head (fully connected) maps  $Z$  to action scores, and a value head (fully connected) estimates the state value. This feature representation encapsulates key attributes of expert navigation strategies [192], providing a compact and expressive input space. A subsequent mapping is then learned from the feature space  $Z$  to the action space, enabling the behavioural cloning model to replicate expert decision-making while requiring fewer input modalities than the original policy. The architecture for the IL task is illustrated in Fig. 4.2.

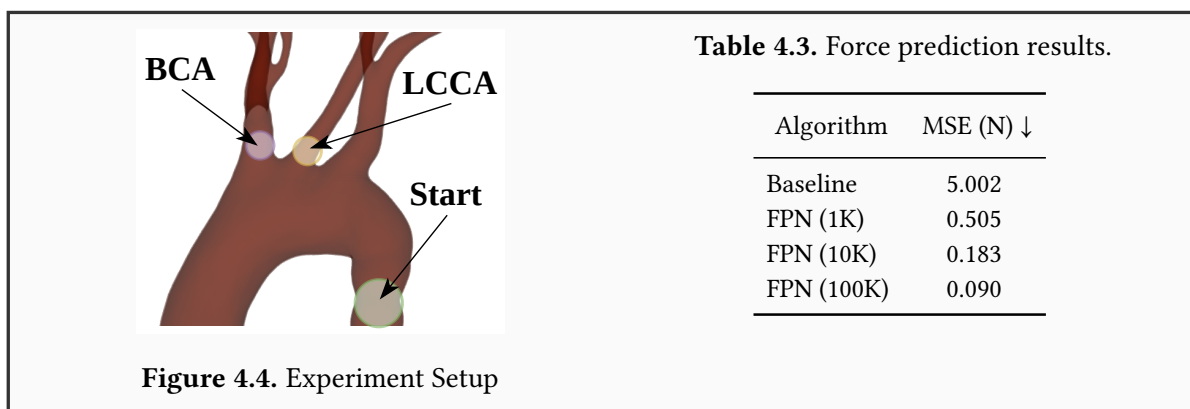
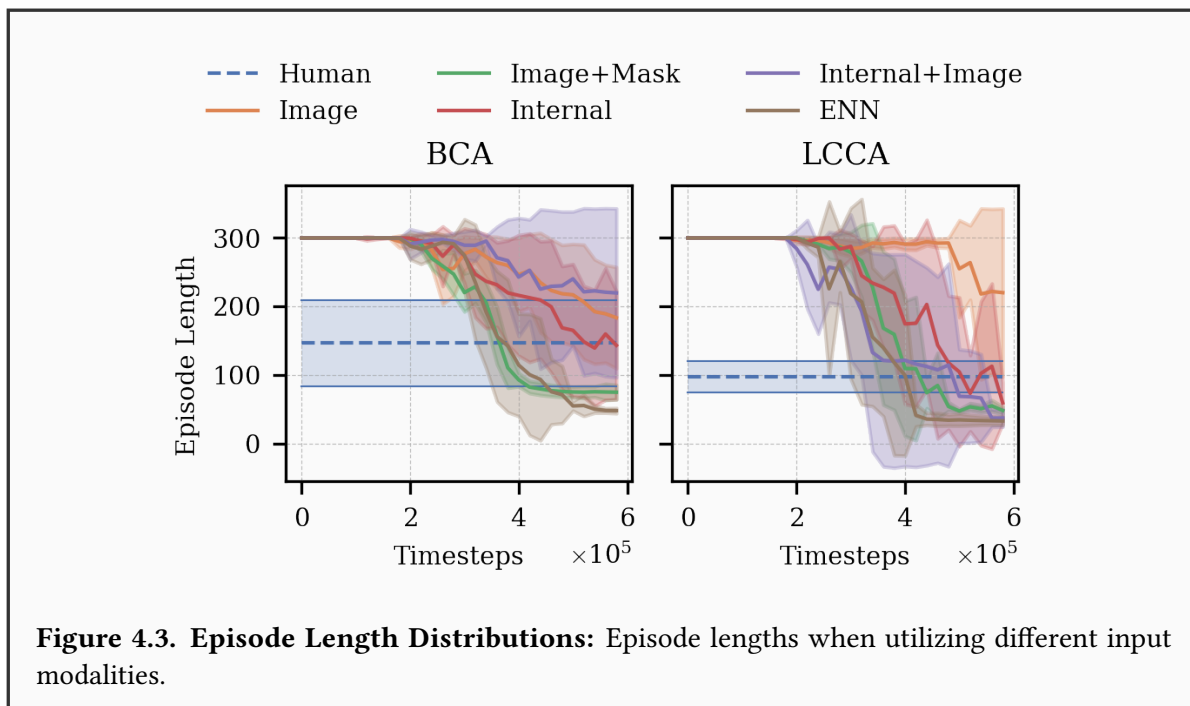
**Force Prediction.** Force prediction is a critical task in endovascular intervention, as surgeons rely on force feedback to avoid damage to the endothelial walls of blood vessels. Several force prediction methods have been explored, including sensor-based techniques [193] and image-based approaches [189].

To assess the force prediction capabilities of the ENN, a supervised learning-based regression model is proposed. The architecture integrates a CNN for visual feature extraction with an MLP head for predicting the contact forces. The model is trained using the following composite loss function:

$$\mathcal{L} = \mathcal{L}_Z + \mathcal{L}_f = \sum_{i=1}^D (Z_i - \hat{Z}_i)^2 + \sum_{i=1}^D (f - \hat{f})^2, \quad (4.2)$$

where  $\hat{Z}$  denotes the feature vector predicted by the network,  $\hat{f}$  represents the predicted force corresponding to the expert transition  $\pi_{\text{exp}}$ , and  $D$  is the total number of samples in the dataset. This formulation penalizes discrepancies between both the predicted and ground truth feature vectors ( $Z_i, \hat{Z}_i$ ) and the predicted and actual forces ( $f, \hat{f}$ ), thereby ensuring accurate modelling of both feature consistency and physical interaction dynamics.

## 4.4 Experiments



### 4.4.1 Expert Trajectory Analysis

Experiments were conducted to validate the effectiveness of expert trajectories using various input modalities, including image, internal state, and segmentation mask representations. In addition, a professional endovascular surgeon was recruited to manually control the *CathSim* environment, thereby generating a “Human” trajectory for comparative analysis.

Catheterization performance was evaluated using a set of quantitative metrics, as described in Subsection 4.4.1.1: Force (N), Path Length (cm), Episode Length (steps), Safety (%), Success (%), and SPL (%). The experiments were carried out for two navigation targets: the [Brachiocephalic Artery \(BCA\)](#) and the [Left Common Carotid Artery \(LCCA\)](#). The initial catheter placements and target locations are visualized in Fig. 4.4.

Across all training configurations, *CathSim* maintained operational speeds ranging from 40 to 80 frames per second, thereby supporting compatibility with real-time applications.

**Table 4.4. Ablation study on input modalities:** ENN (I+V+M) consistently outperforms other input combinations across all metrics. Human expert results are included as reference.

| Target | Input              | Force<br>N ↓       | Path Length<br>cm ↓ | Episode Length<br>s ↓ | Safety<br>% ↑ | Success<br>% ↑ | SPL<br>% ↑ |
|--------|--------------------|--------------------|---------------------|-----------------------|---------------|----------------|------------|
| BCA    | H                  | <b>1.02 ± 0.22</b> | 28.82 ± 11.80       | 146.30 ± 62.83        | <b>83 ± 4</b> | 100 ± 0        | 62         |
|        | V                  | 3.61 ± 0.61        | 25.28 ± 15.21       | 162.55 ± 106.85       | 16 ± 10       | 65 ± 48        | 74         |
|        | V+M                | 3.36 ± 0.41        | 18.55 ± 2.91        | 77.67 ± 21.83         | 25 ± 7        | 100 ± 0        | 86         |
|        | I                  | 3.33 ± 0.46        | 20.53 ± 4.96        | 87.25 ± 50.56         | 26 ± 9        | 97 ± 18        | 80         |
|        | I+V                | 2.53 ± 0.57        | 21.65 ± 4.35        | 221.03 ± 113.30       | 39 ± 15       | 33 ± 47        | 76         |
|        | <b>I+V+M (ENN)</b> | 2.33 ± 0.18        | <b>15.78 ± 0.17</b> | <b>36.88 ± 2.40</b>   | 45 ± 4        | 100 ± 0        | <b>99</b>  |
| LCCA   | H                  | <b>1.28 ± 0.30</b> | 20.70 ± 3.38        | 97.36 ± 23.01         | <b>77 ± 6</b> | 100 ± 0        | 78         |
|        | V                  | 4.02 ± 0.69        | 24.46 ± 5.66        | 220.30 ± 114.17       | 14 ± 14       | 33 ± 47        | 69         |
|        | V+M                | 3.00 ± 0.29        | 16.32 ± 2.80        | 48.90 ± 12.73         | 33 ± 6        | 100 ± 0        | 96         |
|        | I                  | 2.69 ± 0.80        | 22.47 ± 9.49        | 104.37 ± 97.29        | 39 ± 17       | 83 ± 37        | 79         |
|        | I+V                | 2.47 ± 0.48        | 14.87 ± 0.79        | 37.80 ± 10.50         | 42 ± 8        | 100 ± 0        | 100        |
|        | <b>I+V+M (ENN)</b> | 2.26 ± 0.33        | <b>14.85 ± 0.79</b> | <b>33.77 ± 5.33</b>   | 45 ± 5        | 100 ± 0        | 100        |

**Input Legend:** H = Human, I = Internal, V = Vision (Image), M = Segmentation Mask.

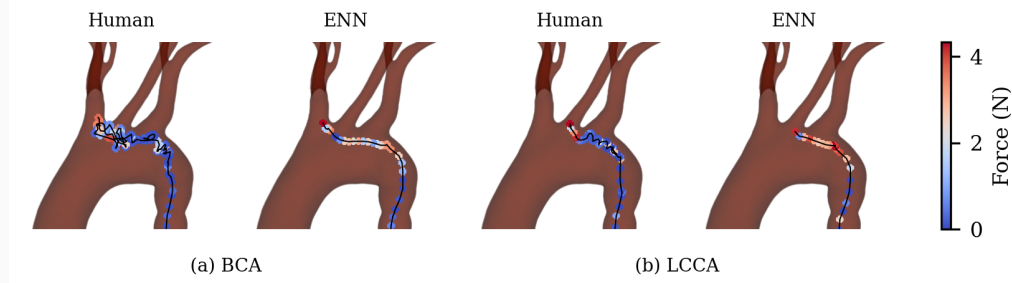


**Figure 4.5. Navigation Paths Comparison:** Examples of navigation path from an endovascular surgeon and our ENN.

**Quantitative Results.** Table 4.4 presents the ablation study results across various input configurations for both the **BCA** and **LCCA** targets. The **ENN**, which integrates internal features, vision, and segmentation mask (I+V+M), consistently achieves the best performance in terms of minimal force exertion, shortest path length, and lowest episode duration. While the human expert (H) demonstrates the highest safety score, **ENN** outperforms all ablated configurations across the remaining metrics. These findings highlight the importance of combining multiple input modalities to improve catheter navigation performance. However, it is important to note that *the human surgeon continues to perform the task with greater safety*, which remains a critical consideration in real-world clinical applications.

**Expert Trajectory vs. Human Skill.** To evaluate the performance of various iterations of the model during training, the mean episode length was computed and compared with that of the human operator. As illustrated in Fig. 4.3, successful navigation of the BCA environment was achieved after  $6 \times 10^5$  time steps, with approximately half of the model checkpoints outperforming the human benchmark. Moreover, the consistency of navigation across both target vessels demonstrates that the ENN achieves robust performance with low inter-seed variance.

Although the ENN surpasses the human operator in terms of trajectory efficiency and completion time, it benefits from access to multiple modalities—including image, internal force, and segmentation mask—whereas the human operator relies solely on image-based inputs for task completion.

**Navigation Path.** A comparison of the navigation paths produced by the ENN and the human operator is shown in Fig. 4.5. The surgeon’s trajectory follows a more meandering path compared to the expert network’s direct and efficient route. In the case of BCA navigation (Fig. 4.5), the human trajectory displays increased irregularity, reflecting the greater anatomical complexity of targeting the BCA relative to the LCCA. This additional challenge is likely attributed to the BCA’s deeper anatomical location within the thoracic region. Despite this, the human operator exerted less force than the ENN, illustrating a higher degree of finesse and tactile sensitivity during catheter manipulation.

#### 4.4.1.1 Evaluation Metrics

**Force.** The force exerted by surgical instruments during simulation is a critical metric for evaluating performance and interaction dynamics with the aorta. To measure this accurately, a manual cannulation method was employed within the simulator. At each simulation time step, collision points between the guidewire and the aortic wall were recorded. These data provided key insights into the tridimensional force components acting on the system, including the normal force ( $f_z$ ) and the frictional forces ( $f_x$  and  $f_y$ ).

The total force magnitude at a given time step  $t$ , denoted as  $f_t$ , was computed using the Euclidean norm of the force vector:

$$f_t = \sqrt{f_{x,t}^2 + f_{y,t}^2 + f_{z,t}^2} \quad (4.3)$$

This calculation offers a comprehensive assessment of the collective impact of the force components, enhancing the understanding of guidewire behaviour and interaction throughout the simulation. Furthermore, it facilitates direct comparison with the experimental force measurements reported by Kundrat *et al.* [126], which were used to validate the simulation

model in Sec. 3.5.1.

**Path Length.** The path length was computed by summing the Euclidean distances between consecutive positions of the guidewire tip. At each time step, the guidewire head position  $h_t$  was recorded. The Euclidean distance between positions at time  $t$  and  $t + 1$  was calculated as  $d(h_t, h_{t+1}) = \sqrt{(h_{t+1} - h_t)^2}$ . The total path length for an episode of length  $n$  was given by:

$$\text{PathLength} = \sum_{i=1}^n \|h_{t+1} - h_t\| \quad (4.4)$$

**SPL.** To evaluate navigation optimality, the [Success Weighted by Normalized Inverse Path Length \(SPL\)](#) (Success weighted by Path Length) metric, as proposed by Anderson *et al.* [194], was applied. This metric compares the actual path length  $p_i$  to the shortest observed path  $l_i$ , treating the latter as the optimal reference. The metric was computed using:

$$\text{SPL} = \frac{1}{N} \sum_{i=1}^N S_i \frac{l_i}{\max(p_i, l_i)}, \quad (4.5)$$

where  $S_i$  is a binary success indicator, and  $N$  is the number of episodes. Given that the expert navigation policy consistently outperforms the human operator, the shortest successful path was used as the optimal baseline.

**Safety.** Safety was defined based on the frequency of force values exceeding  $2N$ , a threshold informed by real-world findings in [126]. A binary variable  $a \in \{0, 1\}$  was introduced, where  $a = 1$  if  $f_t \geq 2N$ . The safety score was computed as:

$$\text{Safety} = 1 - \frac{1}{N} \sum_{i=1}^N a_i, \quad (4.6)$$

where  $N$  denotes the number of steps per episode. A score of 0% indicates that excessive force was applied at every time step, while a score of 100% implies that all forces remained within the safe threshold.

**Episode Length.** Episode length was defined as the total number of steps taken to complete a task. This metric offers a measure of efficiency; shorter episodes generally reflect more efficient navigation, provided task quality is not compromised.

**Success.** An episode was marked as successful if the agent reached the target location within a fixed limit of 300 time steps. This binary metric reflects the agent's ability to complete tasks

under time constraints, emulating the urgency often encountered in clinical scenarios.

## 4.4.2 Downstream Task Results

### 4.4.2.1 Imitation Learning

A comparison was performed between the baseline algorithm (Image-only), the expert policy (i.e., ENN), and the BC algorithm enhanced by expert-generated trajectories. The results, presented in Table 4.5, demonstrate that the integration of expert trajectories markedly improves performance under constrained observation conditions.

Relative to the Image-only baseline, the use of expert trajectories in the BC algorithm led to substantial improvements across multiple evaluation metrics. For both BCA and LCCA targets, the enhanced model exhibited lower force application, shorter path and episode lengths, increased safety, and improved success rate and SPL scores. These findings emphasize the importance of expert-guided learning in simulation and its potential to facilitate sim-to-real transfer in future applications.

**Table 4.5. Imitation Learning Results:** The Imitation Learning results with and without using the Expert Navigation Network (ENN).

| Target | Algorithm     | Force (N) ↓        | Path Length cm ↓    | Episode Length cm ↓ | Safety % ↑    | Success % ↑ | SPL % ↑   |
|--------|---------------|--------------------|---------------------|---------------------|---------------|-------------|-----------|
| BCA    | ENN           | 2.33 ± 0.18        | <b>15.78 ± 0.17</b> | <b>36.88 ± 2.40</b> | 45 ± 4        | 100         | <b>99</b> |
|        | Image wo. ENN | 3.61 ± 0.61        | 25.28 ± 15.21       | 162.55 ± 106.85     | 16 ± 10       | 65          | 74        |
|        | Image w. ENN  | <b>2.23 ± 0.10</b> | 16.06 ± 0.33        | 43.40 ± 1.50        | <b>49 ± 3</b> | 100         | 98        |
| LCCA   | ENN           | <b>2.26 ± 0.33</b> | 14.85 ± 0.79        | 33.77 ± 5.33        | <b>45 ± 5</b> | 100         | 100       |
|        | Image wo. ENN | 4.02 ± 0.69        | 24.46 ± 5.66        | 220.30 ± 114.17     | 14 ± 14       | 33          | 69        |
|        | Image w. ENN  | 2.51 ± 0.21        | <b>14.71 ± 0.20</b> | <b>33.10 ± 2.07</b> | 43 ± 4        | 100         | 100       |

**Network Architecture.** The BC network architecture consists of a structured sequence of convolutional and fully connected layers. The input, a tensor of shape (1, 80, 80), is a single-channel greyscale crop (80×80 px) of the fluoroscopic frame, resized from the original image and intensity-normalized to [0, 1]. It is processed through three Conv2D layers, each followed by a **Rectified Linear Unit (ReLU)** activation function. The resulting feature maps are then flattened into a single vector, which is passed through a fully connected Linear layer with **ReLU** activation, and finally through an output Linear layer without activation to produce the raw action scores. This architecture enables effective transformation of visual input into control decisions. Architectural details are provided in Table 4.6.

**Training Methodology.** Training was conducted using the Adam optimizer [60], with a batch size of 32, a learning rate of  $1 \times 10^{-3}$ , and an entropy coefficient of the same magnitude.

**Table 4.6. BC Architecture:** BC Architecture

| Layer (type) | Output Shape | Param # | Nonlinearity | Kernel | Stride | Padding |
|--------------|--------------|---------|--------------|--------|--------|---------|
| Input        | (1, 80, 80)  | 0       | -            | —      | —      | —       |
| Conv2D       | (32, 19, 19) | 2,080   | ReLU         | 8      | 4      | 0       |
| Conv2D       | (64, 8, 8)   | 32,832  | ReLU         | 4      | 2      | 0       |
| Conv2D       | (64, 6, 6)   | 36,928  | ReLU         | 3      | 1      | 0       |
| Flatten      | (2304)       | 0       | -            | —      | —      | —       |
| Linear       | (256)        | 590,080 | ReLU         | —      | —      | —       |
| Linear       | (128)        | 32,896  | ReLU         | —      | —      | —       |
| Linear       | (2)          | 258     | None         | —      | —      | —       |

**Table 4.7. BC Hyperparameters:** BC Hyperparameters

| Hyperparameter      | Default Value      |
|---------------------|--------------------|
| Batch Size          | 32                 |
| Optimizer           | Adam               |
| Learning Rate       | $1 \times 10^{-3}$ |
| Entropy Coefficient | $1 \times 10^{-3}$ |
| Epochs              | 800                |

These hyperparameters, summarized in Table 4.7, controlled both the optimization step size and the degree of exploratory behaviour. The network was trained for 800 epochs, with each epoch encompassing a complete pass through the dataset, allowing for sufficient convergence of the model parameters.

#### 4.4.2.2 Force Prediction

Table 4.3 summarizes the results of fine-tuning the [Force Prediction Network \(FPN\)](#) using varying quantities of trajectory samples generated by the [ENN](#). Performance was evaluated based on the [Mean Squared Error \(MSE\)](#) between the predicted and actual force values.

The baseline [MSE](#) was measured at 5.0021N. Following fine-tuning with  $1 \times 10^3$  samples, the [MSE](#) decreased to 0.5047N, illustrating the value of expert-generated trajectories. This trend continued as additional samples were introduced:  $1 \times 10^4$  samples reduced the [MSE](#) to 0.1828N, and  $1 \times 10^5$  samples led to a further reduction to 0.0898N. These results indicate that the expert network is capable of generating high-quality data that is instrumental in training robust predictive models. Such volume and quality of training data would be difficult, if not infeasible, to obtain from human operators in real-world settings.

## 4.5 Conclusion and Discussion

The work introduces the ENN and investigates its application to downstream tasks in autonomous catheterization. Although no new learning algorithms are proposed, the approach demonstrates how the capabilities of the ENN can be leveraged to improve performance in tasks such as IL and force prediction. Through the integration of multiple input modalities and the generation of expert trajectories, the ENN exhibits strong potential for addressing the complex challenges associated with endovascular navigation.

Drawing inspiration from advancements in related domains such as autonomous driving [195], this research is intended to encourage greater engagement from the ML community with the emerging yet critical domain of autonomous catheterization. The results highlight the promise of machine learning frameworks in enhancing patient safety, precision, and procedural efficiency in endovascular interventions. The multimodal approach demonstrated in this chapter sets the stage for addressing data scarcity challenges in endovascular imaging, which will be the focus of the next chapter through the introduction of the Guide3D dataset.

## Chapter 5

---

# Stereo X-Ray-Based 3D Reconstruction

*Endovascular navigation is highly dependent on fluoroscopic imaging due to the limited availability of sensory feedback. However, traditional methods for 3D reconstruction often rely on specialized hardware or require prolonged exposure to ionizing radiation. To address these limitations, a novel deep learning framework is proposed for 3D guidewire reconstruction, which utilizes a spherical coordinate representation for efficient modelling and a *Gated Recurrent Unit (GRU)*-based architecture for accurate shape prediction. Extensive evaluations demonstrate strong predictive performance, including a *Maximum Euclidean Distance (MaxED)* of  $6.88 \pm 5.23$  and a *Mean Error in Tip Tracking (METE)* of  $3.28 \pm 2.59$ , even under challenging anatomical conditions. To support reproducibility and accelerate progress in the field, a new benchmark dataset, *Guide3D*, is introduced. This dataset comprises publicly available bi-planar X-ray images with annotated fluoroscopic video sequences for guidewire shape prediction. The proposed approach enhances both the accuracy and efficiency of guidewire 3D reconstruction and contributes to the broader research community by providing an open-access resource for future innovation.*

This chapter presents the work from the following publications:

- **Jianu, T. et al.**, “Guide3d: A bi-planar x-ray dataset for guidewire segmentation and 3d reconstruction,” in *Proceedings of the Asian Conference on Computer Vision (ACCV)*, Code available at: <https://airvlab.github.io/guide3d/>, Dec. 2024, pp. 1549–1565
- **Jianu, T. et al.**, “Deepwire: Spherical coordinate-based deep learning for accurate guidewire shape reconstruction,” in *Proceedings of the 9th International Conference on Biomedical Signal and Image Processing (ICBIP 2024)*, Suzhou, China, 2024
- **Jianu, T. et al.**, “3d guidewire shape reconstruction from monoplane fluoroscopic images,” in *International Conference on Robot Intelligence Technology and Applications*, Springer, 2023, pp. 84–94

## 5.1 Introduction

Minimally invasive surgery has transformed endovascular intervention by offering less intrusive alternatives that promote accelerated recovery [170]. These advancements rely significantly on precise instrument navigation, which is typically achieved through imaging technologies, particularly 2D visualization methods such as *monoplanar fluoroscopy*. This imaging modality is widely adopted due to its minimal disruption to surgical workflows and its cost-effectiveness [199]. However, its inherent reliance on two-dimensional projections introduces critical limitations, most notably the absence of depth perception. This deficit complicates the spatial localization of surgical instruments and increases the likelihood of unintentional contact with fragile arterial structures, potentially resulting in arterial damage, clot formation, or decreased procedural accuracy [114, 116]. Furthermore, 2D imaging techniques are often constrained by limited resolution and an inability to provide real-time 3D guidance, thereby complicating the execution of complex interventions. Overcoming these imaging constraints is imperative for improving patient safety, minimizing procedural risks, and enhancing the success rate of minimally invasive techniques.

To address the lack of depth perception, multi-view imaging systems—particularly biplanar scanners—have been introduced in endovascular procedures. These systems enhance spatial localization by integrating multiple angular perspectives [112, 113, 114, 200], often employing epipolar geometry-based methods to reconstruct accurate 3D representations [108]. Despite their advantages, two key challenges limit the widespread adoption and utility of these systems [122]: *i*) the difficulty of accurate image segmentation due to low contrast, overlapping anatomical structures, and motion artefacts, which undermine the reliability of shape reconstruction algorithms; and *ii*) the dependence on specialized biplanar scanners, which are cost-prohibitive and not readily available in many clinical environments [112]. Addressing these challenges necessitates the development of robust datasets encompassing a wide range of anatomical and imaging scenarios. Such resources would support the training and validation of segmentation and reconstruction algorithms, ultimately enabling more accessible and reliable imaging solutions across diverse clinical contexts.

In this chapter, a series of interconnected contributions to guidewire reconstruction in endovascular intervention are introduced, spanning simulation-based experimentation, real-world data application, and dataset development. First, we apply reconstruction techniques to real-life data using a manually annotated dataset and introduce a spherical coordinate representation enhanced by [Recurrent Neural Networks \(RNNs\)](#). Secondly, the Guide3D dataset is presented as a large-scale, publicly available resource informed by insights from the prior contributions. Guide3D facilitates scalable 3D reconstruction, offering a foundation for advancing guidewire navigation in both research and clinical applications.

## 5.2 Related Works

**Endovascular Datasets.** Datasets serve a pivotal role in advancing endovascular navigation by providing the foundational resources for algorithm development, evaluation, and benchmarking. Existing datasets have been derived from multiple imaging modalities, including mono X-ray [132, 200, 201, 202], 3D echocardiography [107], and 3D MRI [203]. These datasets comprise both real and synthetic imagery; however, their limited availability for critical tasks such as tool segmentation and 3D reconstruction continues to pose a significant bottleneck [132, 200, 201, 203, 204]. Mono X-ray datasets remain dominant within the context of endovascular interventions (see Table 5.1), yet they often lack the spatial fidelity required for high-precision 3D reconstruction. This shortfall underscores the need for comprehensive and standardized datasets specifically designed for guidewire and catheter-related applications.

**Catheter and Guidewire Segmentation.** The segmentation of endovascular instruments, such as guidewires and catheters, is a prerequisite for accurate navigation and procedural success. However, progress in this domain is tightly coupled with the availability and granularity of annotated datasets. Due to the scarcity of real-world annotated data, synthetic and semisynthetic datasets have been increasingly adopted, leveraging modalities such as 2D X-ray and 3D MRI [200, 201, 203]. Synthetic datasets have been shown to improve training efficiency and model generalizability [132, 204]. Deep learning-based approaches, particularly those employing U-Net architectures [205], have significantly advanced segmentation accuracy, enabling fully automated pipelines. Furthermore, optical flow-based unsupervised methods have contributed to streamlined tracking of instruments during interventions. Nevertheless, the continued absence of a publicly available, standardized dataset for catheter and guidewire segmentation remains a major limitation, hindering both reproducibility and clinical translation of state-of-the-art methods.

**Table 5.1.** Endovascular intervention datasets comparison.

| Dataset                       | Data Collection | Data Type | #Frames          | Data Source                      | Annotation | Public | Task                              |
|-------------------------------|-----------------|-----------|------------------|----------------------------------|------------|--------|-----------------------------------|
| Barbu <i>et al.</i> [201]     | Mono X-ray      | Video     | 535              | Real                             | Manual     | No     |                                   |
| Wu <i>et al.</i> [107]        | 3D Echo         | Video     | 800              | Real                             | Manual     | No     |                                   |
| Ambrosini <i>et al.</i> [200] | Mono X-ray      | Image     | 948              | Real                             | Manual     | No     |                                   |
| Mastmeyer <i>et al.</i> [203] | 3D MRI          | Image     | 101              | Real                             | Manual     | No     | Segmentation                      |
| Yi <i>et al.</i> [202]        | Mono X-ray      | Image     | 2,540            | Synthesis                        | Automatic  | No     |                                   |
| Nguyen <i>et al.</i> [132]    | Mono X-ray      | Image     | 25,271           | Phantom                          | Semi-Auto  | No     |                                   |
| Danilov <i>et al.</i> [204]   | 3D Ultrasound   | Video     | 225              | Synthetic                        | Manual     | No     |                                   |
| Wagner <i>et al.</i> [113]    | Mono X-ray      | Video     | –                | Phantom                          | Automatic  | No     |                                   |
| Hoffmann <i>et al.</i> [114]  | Mono X-ray      | Image     | 176              | Phantom                          | Semi-Auto  | No     |                                   |
| Delmas <i>et al.</i> [206]    | Mono X-ray      | Image     | 2,289<br>5<br>63 | Simulated<br>Phantom<br>Clinical | Automatic  | No     | 3D Reconstruction                 |
| Baur <i>et al.</i> [108]      | Bi-planar X-ray | Image     | 70               | Canine                           | Manual     | No     |                                   |
| Brost <i>et al.</i> [207]     | Mono X-ray      | Image     | 938              | Clinical                         | Semi-Auto  | No     |                                   |
| Ma <i>et al.</i> [105]        | Mono X-ray, CT  | Image     | 1,048            | Clinical                         | Manual     | No     |                                   |
| Hoffmann <i>et al.</i> [115]  | Bi-planar X-Ray | Video     | 33               | Clinical                         | Semi-Auto  | No     |                                   |
| <b>Guide3D (ours)</b>         | Bi-planar X-ray | Video     | 8,746            | Phantom                          | Manual     | Yes    | Segmentation<br>3D Reconstruction |

**3D Reconstruction in Endovascular Procedures.** Accurate 3D reconstruction plays a critical role in endovascular interventions by facilitating advanced visualization, precise instrument tracking, and improved clinical outcomes. Historically, biplane fluoroscopic imaging systems have served as the cornerstone for 3D shape reconstruction, employing triangulation and epipolar geometry principles. Early work by Burgner, Herrell, and Webster III [112] introduced projective-invariant triangulation for shape estimation, which was later refined through elastic grid registration and graph-search algorithms by Wagner *et al.* [113], Hoffmann *et al.* [114], Hoffmann *et al.* [116], and Hoffmann *et al.* [115]. The clinical relevance of 3D vascular modelling has also been demonstrated in both biplanar and single-view contexts by Delmas *et al.* [206] and Petković, Homan, and Lončarić [208].

Despite their precision, biplane systems see limited clinical use due to high costs, increased radiation, and workflow disruptions. This has driven interest in monoplanar imaging as a more accessible alternative. Methods like those of Lobaton *et al.* [117] and Vandini *et al.* [118] combine fluoroscopic views with kinematic priors for shape reconstruction, but often require C-arm repositioning, interrupting procedures. To mitigate this, Vandini *et al.* [119] proposed an automated robotic approach fusing kinematics with fluoroscopy, avoiding C-arm adjustments. Other works, such as Otake *et al.* [120] and Papalazarou, Rongen, *et al.* [121], explore piecewise-rigid 2D/3D registration and non-rigid SfM. Yet, monoplanar systems still rely on multiple closely-spaced views, raising computational demands and radiation exposure.

**Challenges and Emerging Approaches.** Despite continued advancements in biplane and monoplanar reconstruction methods, several persistent challenges remain, including elevated system costs, workflow disruptions, and high computational complexity. These limitations underscore the promise of deep learning techniques, which have demonstrated the ability to infer guidewire and catheter shapes directly from monoplanar images with high accuracy. Unlike traditional methods, deep learning approaches eliminate the need for dual-view setups and reduce reliance on manual intervention. However, such methods demand access to large, diverse datasets to ensure robust training and generalizability.

To address these gaps, there is a pressing need for the development of specialized datasets that support both 3D reconstruction and tool segmentation at scale. These datasets must account for anatomical and imaging variability encountered in real-world clinical environments and provide a reliable foundation for benchmarking algorithmic progress. Establishing such resources is essential for advancing the field toward safer and broadly accessible endovascular procedures.

## 5.3 The Guide3D Dataset

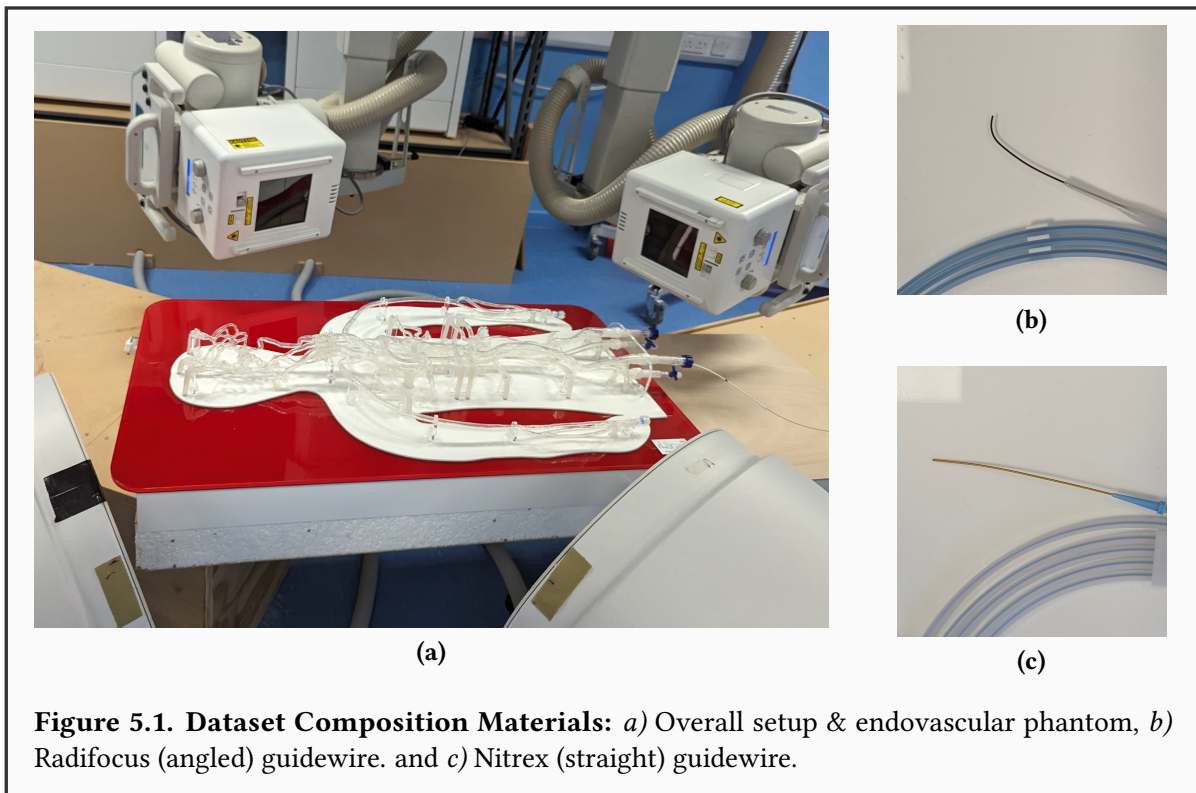


**Figure 5.1. Dataset Composition Materials:** *a)* Overall setup & endovascular phantom, *b)* Radifocus (angled) guidewire, and *c)* Nitrex (straight) guidewire.

### 5.3.1 Data Collection Setup

**X-ray System.** The setup utilized a Bi-planar X-ray system (Fig. 5.1a) with 60kW Epsilon X-ray Generators from EMD Technologies Ltd. and 16-inch Image Intensifier Tubes by Thales, featuring dual focal spot Variant X-ray tubes for high-definition imaging. The setup included Ralco Automatic Collimators for precise alignment and exposure, with calibration achieved through acrylic mirrors and geometric alignment grids.

**Anatomical Models.** The study utilized the half-body vascular phantom model from Elastrat Sarl Ltd., Switzerland (Fig. 5.1a). This model is enclosed in a transparent box and integrated into a closed water circuit to simulate blood flow. Constructed from soft silicone and incorporating compact continuous flow pumps with a slippery liquid, it replicates human blood flow dynamics. The design is based on detailed postmortem vascular casts, ensuring anatomical accuracy reflective of human vasculature as documented in seminal works [150, 151]. The utilization of this anatomically accurate model facilitated the realistic simulation of vascular scenarios.

**Surgical Tools.** The dataset was enhanced by navigating complex vascular structures using two distinct types of guidewires that are widely used in real-world endovascular surgery.

**Table 5.2.** Dataset Composition Overview.

| Sample Type | Radifocus™ Guide Wire (Angled) | Nitrex Guidewire (Straight) | Total |
|-------------|--------------------------------|-----------------------------|-------|
| w fluid     | 3,664                          | 484                         | 4,148 |
| wo fluid    | 2,472                          | 2,126                       | 4,598 |
| Total       | 6,136                          | 2,610                       | 8,746 |

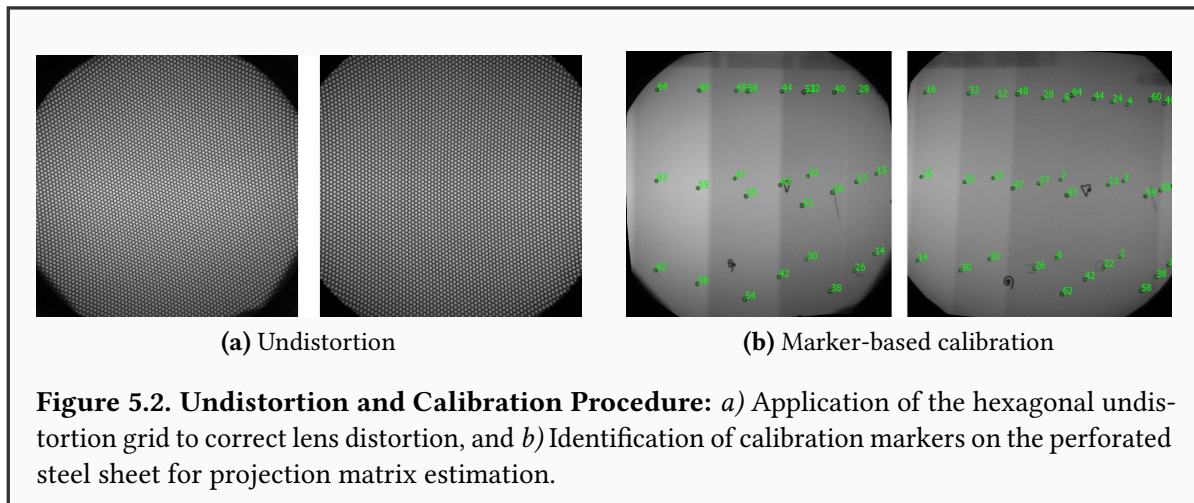
The first, the Radifocus™ Guide Wire M Stiff Type (Terumo Ltd.) (Fig. 5.1c), is manufactured from nitinol and coated in polyurethane-tungsten. It features a diameter of 0.89mm, a length of 260cm, and a 3cm angled tip. This guidewire is commonly used for seeking, dissecting, and crossing lesions. The second, the Nitrex Guidewire (Nitrex Metal Inc.) (Fig. 5.1b), is also composed of nitinol and offers a gold-tungsten straight tip. It measures 0.89mm in diameter and approximately 300cm in length, with a 15cm straight tip, making it suitable for navigating tortuous vascular paths.

### 5.3.2 Data Acquisition, Labelling, and Statistics

Utilizing the materials described in Subsection 5.3.1, a dataset of 8,746 high-resolution samples ( $1,024 \times 1,024$  pixels) was compiled. This dataset includes 4,373 paired instances with and without a simulated blood flow medium. Specifically, it comprises 6,136 samples from the Radifocus Guidewire and 2,610 from the Nitrex guidewire, establishing a robust foundation for automated guidewire tracking in bi-planar scanner images. Manual annotation was performed using the Computer Vision Annotation Tool (CVAT) [209], where polylines were created to accurately track the dynamic path of the guidewire. The decision to represent the guidewire as a polyline was due to the inherent structure of a guidewire, where certain parts would inevitably overlap, making a segmentation mask an unsuitable representation. In contrast, a polyline can effectively represent a looping guidewire, providing better accuracy. As detailed in Table 5.2, the dataset includes 3,664 instances of angled guidewires with fluid and 484 without, while straight guidewires are represented by 2,472 instances with fluid and 2,126 without. This distribution illustrates a variety of procedural contexts. It is noted that all 8,746 images in the dataset are equipped with *manual segmentation ground truth*, hence supporting the development of algorithms that need segmentation maps as the reference.

### 5.3.3 Camera Calibration and Distortion Correction

The camera parameters were extracted by following the traditional undistortion and calibration method. Initially, undistortion was achieved using a Local Weighted Mean (LWM) algorithm, applying a perforated steel sheet with a hexagonal pattern (from McMaster-Carr Ltd., part



number 9255T645) as the framing reference, and employing a blob detection algorithm for precise identification of distortion points [210]. This setup established correspondences between distorted and undistorted positions, enabling accurate distortion correction as per Verdonck *et al.* [211]. A subsequent calibration step was undertaken utilizing a semi-automatic approach for marker identification and a Random Sampling Consensus (RANSAC) method to ensure robustness in computing the projection matrix and deriving intrinsic and extrinsic camera parameters. The calibration process was refined through Direct Linear Transformation (DLT) and non-linear optimization, considering multiple poses of the calibration object to optimize the entire camera setup [212]. Figure 5.2 illustrates two key stages of the calibration procedure. Panel (a) shows the application of the hexagonal undistortion grid used to correct lens distortion. Panel (b) depicts the subsequent step of identifying calibration markers on the reference sheet, which enables the computation of projection matrices.

### 5.3.4 Guidewire Reconstruction

Given polyline representations of a curve in both planes, the reconstruction process is initiated by parameterizing these curves using B-Spline interpolation. This is achieved by expressing each curve as a function of the cumulative distance along the curve. Specifically, let  $C_A(\mathbf{u}_A)$  and  $C_B(\mathbf{u}_B)$  be the parameterized B-Spline curves in their respective planes, where  $\mathbf{u}_A$  and  $\mathbf{u}_B$  are the normalized arc-length parameters. Next, the corresponding  $\mathbf{u}_B$  for a given  $\mathbf{u}_A$  is found using epipolar geometry. Once the corresponding points  $C_A(\mathbf{u}_A^i)$  and  $C_B(\mathbf{u}_B^i)$  are identified, the 3D coordinates  $\mathbf{P}^i$  of these points are computed by triangulation. This results in a set of 3D points  $\{\mathbf{P}^i\}_{i=1}^M$ , where  $M$  is the total number of sampled points, effectively reconstructing the original curve in 3D space.

### 5.3.4.1 Retrieving the Fundamental Matrix $F$ .

The relationship between the points in Image A ( $I_A$ ) and Image B ( $I_B$ ) is described by the fundamental matrix  $F$ , which satisfies the condition  $\mathbf{x}_B^T F \mathbf{x}_A = 0$  for corresponding points  $\mathbf{x}_A$  in  $I_A$  and  $\mathbf{x}_B$  in  $I_B$ . Given the calibration steps undertaken in Subsection 5.3.3, the projection matrices  $\mathbf{P}_A$  and  $\mathbf{P}_B$  are now available. From these projection matrices, the fundamental matrix can be derived as follows:

$$\mathbf{F} = [\mathbf{e}_B]_{\times} \mathbf{P}_B \mathbf{P}_A^+, \quad (5.1)$$

where  $\mathbf{e}_B$  is the epipole in Image B, defined as  $\mathbf{e}_B = \mathbf{P}_B \mathbf{C}_A$ , with  $\mathbf{C}_A$  being the camera centre of  $\mathbf{P}_A$ . The notation  $[\mathbf{e}_B]_{\times}$  represents the skew-symmetric matrix of the epipole  $\mathbf{e}_B$ , which is given by:

$$[\mathbf{e}_B]_{\times} = \begin{bmatrix} 0 & -e_{B3} & e_{B2} \\ e_{B3} & 0 & -e_{B1} \\ -e_{B2} & e_{B1} & 0 \end{bmatrix} \quad (5.2)$$

Here,  $\mathbf{e}_B = (e_{B1}, e_{B2}, e_{B3})^T$ . The matrix  $\mathbf{P}_A^+$  is the pseudoinverse of the projection matrix  $\mathbf{P}_A$ . The fundamental matrix  $F$  encapsulates the epipolar geometry between the two views, ensuring that corresponding points  $\mathbf{x}_A$  and  $\mathbf{x}_B$  lie on their respective epipolar lines.

### 5.3.4.2 Epipolar Matching of Curve Representations

The matching phase begins with uniformly sampling points along the curve  $C_A(u_A)$  at intervals  $\Delta u_A$ . For each sampled point  $x_A = C_A(u_A)$ , the epiline  $l_B = Fx_A$  is projected into Image B. The intersection of the epiline  $l_B$  with the curve  $C_B(u_B)$  is then determined, thereby obtaining the corresponding parameter  $u_B$  for each  $u_A$ .

Due to errors in the projection matrices  $P_A$  and  $P_B$ , there are instances where the epiline  $l_B$  does not intersect with any part of the curve  $C_B$ . To address this, similar to the approach in [213], a monotonic function  $f_A(u_A) \rightarrow u_B$  is fitted using a Piecewise Cubic Hermite Interpolating Polynomial (PCHIP), thus interpolating the missing intersections. The matching can be visualized in Fig. 5.3.

### 5.3.4.3 Triangulation for 3D Point Recovery

Given the projections from both the first and second cameras, a system of linear equations can be constructed as:

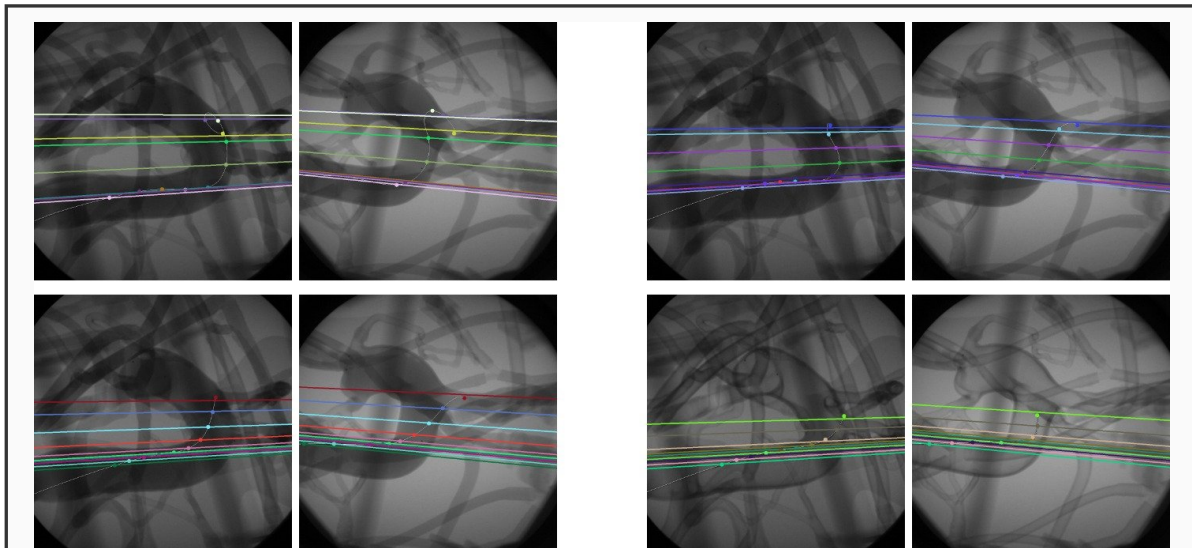


**Figure 5.3. Point Matching Process:** Sampled points from image  $I_A$  ( $C_A(u_A)$ ) and their corresponding epilines  $l_A$  on image  $I_B$  with their matches  $C_B(u_B)$ . The epilines for  $C_B(u_B)$  are then computed and displayed on the image  $I_A$ .

$$\begin{aligned} \mathbf{x}_1 \times (\mathbf{P}_1 \mathbf{X}) &= 0 \\ \mathbf{x}_2 \times (\mathbf{P}_2 \mathbf{X}) &= 0 \end{aligned} \tag{5.3}$$

Therefore, a system of linear equations of the form  $\mathbf{A}\mathbf{X} = 0$  is formed, wherein  $\mathbf{A}$  is a  $4 \times 4$  matrix composed of rows from the projection matrices  $\mathbf{P}_1$  and  $\mathbf{P}_2$  and the image coordinates  $\mathbf{x}_A$  and  $\mathbf{x}_B$ . By employing the Singular Value Decomposition (SVD) [214] on  $\mathbf{A}$ , the desired  $\mathbf{X}$  minimizing  $\|\mathbf{A}\mathbf{X}\|$  subject to  $\|\mathbf{X}\| = 1$  is determined. The solution corresponds to the eigenvector associated with  $\mathbf{A}$ 's smallest singular value, thereby deriving the homogeneous coordinates for the triangulated 3D point. Finally, all reprojections were verified to ensure geometric plausibility. Reconstructions with an average reprojection error greater than 25 pixels (approximately 2.5% of the  $1024 \times 1024$  image resolution) were considered inaccurate and discarded.

### 5.3.5 Utility of Guide3D Dataset for the Research Community

Guide3D advances endovascular imaging by offering a bi-planar fluoroscopic dataset for *segmentation* and *3D reconstruction*, serving as an open-source benchmark. It supports precise algorithm comparisons for segmentation [132, 200, 215, 216] and facilitates method development in 3D reconstruction with its use of bi-planar imagery [105, 108, 207, 217]. With video data, Guide3D enables *video*-based methods, leveraging temporal dimensions for dynamic analysis, which enriches the segmentation and reconstruction capabilities whilst also adhering to the nature of the procedure. This versatility underscores Guide3D's crucial role in advancing endovascular imaging [122].

## 5.4 Guidewire Shape Prediction

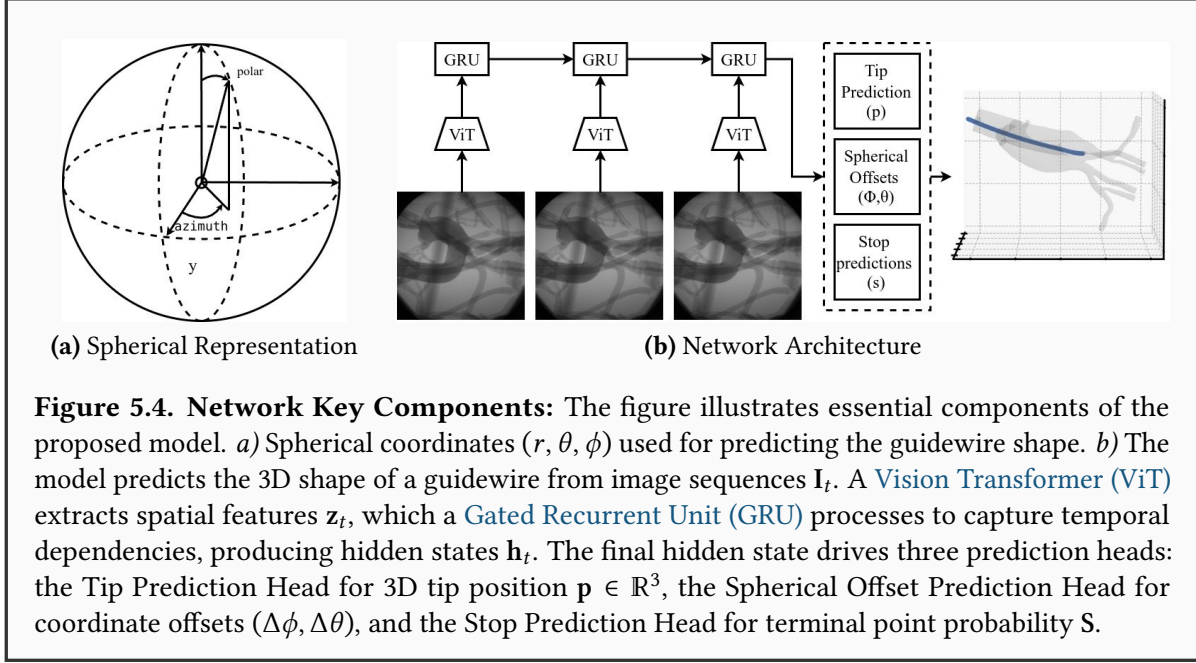
Utilizing the Guide3D dataset, this section builds a benchmark for the shape prediction task. Accurate shape prediction of the guidewire is essential for successful navigation and intervention. In particular, a novel shape prediction network is presented, aimed at predicting the guidewire shape from a sequence of monoplanar images. The motivation behind this approach lies in the potential of deep learning to learn spatio-temporal correlations from a static camera with a dynamic scene [218]. Unlike the conventional reconstruction methods requiring biplanar images [112], the network leverages a sequence of images to provide temporal information, enabling the network to learn a mapping from a single image  $I_A$  to the 3D guidewire curve  $C(\mathbf{u})$ . By adopting deep learning techniques, the aim is to simplify the shape prediction process while maintaining high accuracy. This method holds promise for enhancing endovascular navigation by providing real-time, accurate predictions of the guidewire shape, ultimately improving procedural outcomes and reducing reliance on specialized equipment.

**Task formulation.** Given a sequence of single-plane images  $\{I_{A,t}\}_{t=1}^T$ , the goal is to predict a 3D curve  $C(u)$  parameterized by arclength. For supervision, the curve is uniformly discretized at step  $\Delta u$  into  $M$  points  $\{u_j\}_{j=1}^M$ . The network outputs (i) a tip position  $\mathbf{p} \in \mathbb{R}^3$ , (ii) per-point angular offsets  $\{(\Delta\phi_j, \Delta\theta_j)\}_{j=1}^M$  under a fixed radius  $r$ , and (iii) a stop distribution  $S \in [0, 1]^M$  over the  $M$  positions indicating the terminal index. At inference, the 3D curve is reconstructed by integrating the angular offsets from the tip and truncating at  $\arg \max_j S_j$ .

### 5.4.1 Spherical Coordinates Representation

Predicting 3D points directly can be challenging due to the high degree of freedom. To mitigate this, spherical coordinates are used, which offer significant advantages over Cartesian coordinates for guidewire shape prediction. Spherical coordinates, as represented in Fig. 5.4a, defined by the radius  $r$ , polar angle  $\theta$ , and azimuthal angle  $\phi$ , provide a more natural representation for the position and orientation of points along the guidewire, which is typically elongated and curved. Mathematically, a point in spherical coordinates  $(r, \theta, \phi)$  can be converted to Cartesian coordinates  $(x, y, z)$  using the transformations  $x = r \sin \theta \cos \phi$ ,  $y = r \sin \theta \sin \phi$ , and  $z = r \cos \theta$ . This conversion simplifies the modelling of angular displacements and rotations, as spherical coordinates directly encode directional information.

Predicting angular displacements  $(\Delta\theta, \Delta\phi)$  relative to a known radius  $r$  aligns with the physical constraints of the guidewire, facilitating more accurate and interpretable shape predictions. By predicting an initial point (tip position) and representing subsequent points as offsets in  $\Delta\phi$  and  $\Delta\theta$  while keeping  $r$  fixed, this method simplifies shape comparison and reduces the parameter space. This approach enhances the model's ability to capture the guidewire's spatial configuration and improves overall prediction performance.



## 5.4.2 Network Architecture

The proposed model (shown in Fig. 5.4b) addresses the problem of predicting the 3D shape of a guidewire from a sequence of images. Each image sequence captures the guidewire from different time steps ( $I_{A,t}$ ), and the goal is to infer the continuous 3D shape  $C_t(\mathbf{u}_t)$ . This many-to-one prediction task is akin to generating a variable-length sequence from variable-length input sequences, a technique commonly utilized in fields such as machine translation [219] and video analysis.

To achieve this, the input pipeline consists of a sequence of images depicting the guidewire. A ViT [54], pre-trained on ImageNet, is employed to extract high-dimensional spatial feature representations from these images. The output embeddings of the ViT are subsequently passed through a **Multi-Layered Perceptron (MLP)**, producing the feature maps  $z_t \in \mathbb{R}^{512}$ . These feature maps are then fed into a GRU to capture the temporal dependencies across the image sequence. The GRU processes the feature maps  $z_t$  from consecutive time steps, producing a sequence of hidden states  $h_t$ . Formally, the GRU operation at time step  $t$  is defined as:

$$\mathbf{h}_t = \text{GRU}(z_t, \mathbf{h}_{t-1}), \quad (5.4)$$

where  $h_t \in \mathbb{R}^H$  denotes the final hidden state dimension. *Module details:* the ViT-to- $z_t$  projection is a lightweight MLP (single hidden layer, GELU, dropout  $p=0.1$ ) to 512 dimensions; the GRU uses a single recurrent layer with hidden size  $H$  (512 in our implementation) and dropout  $p=0.1$  between time steps.

The final hidden state  $h_t$  from the GRU is used by three distinct prediction heads. Each head is implemented as a lightweight MLP with a single hidden layer (width 256), GELU activation,

and dropout  $p = 0.1$ :

- **Tip Prediction Head:** an [MLP](#) maps  $\mathbf{h}_t$  to a 3D Cartesian anchoring point.
- **Spherical Offset Prediction Head:** an [MLP](#) outputs angular offsets  $(\Delta\phi, \Delta\theta)$  for a discretized curve.
- **Stop Prediction Head:** an [MLP](#) outputs logits over the same discretization; a softmax is applied to obtain the terminal-point probability vector  $\mathbf{S}$ .

*Softmax length ( $M$ ).* The number of positions  $M$  is set by a uniform arclength discretization with step  $\Delta u$  and fixed to the maximum sequence length observed across the training set under this sampling. Shorter sequences are right-padded to length  $M$  and masked in the loss; the target stop label is a one-hot vector of length  $M$  indicating the terminal index.

### 5.4.3 Loss Function

The custom loss function for training the model combines multiple components to handle the point-wise tip error, variable guidewire length (stop criteria), and tip position predictions. The overall loss function  $\mathcal{L}_{\text{total}}$  is defined as:

$$\mathcal{L}_{\text{total}} = \frac{1}{N} \sum_{i=1}^N \left( \lambda_{\text{tip}} \|\hat{\mathbf{p}}_i - \mathbf{p}_i\|^2 + \lambda_{\text{offset}} ((\hat{\phi}_i - \phi_i)^2 + (\hat{\theta}_i - \theta_i)^2) + \lambda_{\text{stop}} (-\mathbf{s}_i \log(\hat{\mathbf{s}}_i) - (1 - \mathbf{s}_i) \log(1 - \hat{\mathbf{s}}_i)) \right), \quad (5.5)$$

where  $N$  is the number of samples, and  $\lambda_{\text{tip}}$ ,  $\lambda_{\text{offset}}$ , and  $\lambda_{\text{stop}}$  are weights that balance the contributions of each loss component. The tip prediction loss ( $\mathcal{L}_{\text{tip}}$ ) uses [Mean Squared Error \(MSE\)](#) to ensure accurate 3D tip coordinates. The spherical offset loss ( $\mathcal{L}_{\text{offset}}$ ) also uses [MSE](#) to align predicted and ground truth angular offsets, capturing the guidewire’s shape. The stop prediction loss ( $\mathcal{L}_{\text{stop}}$ ) employs [Binary Cross-Entropy \(BCE\)](#) to accurately predict the guidewire’s endpoint.

**Stop criterion (variable length).** Each guidewire curve is uniformly sampled along arclength into  $M$  positions (step  $\Delta u$ ). For sample  $i$ , a one-hot vector  $\mathbf{s}_i \in \{0, 1\}^M$  marks the terminal index  $j_i^*$ . The network outputs  $\hat{\mathbf{s}}_i \in [0, 1]^M$  over these positions. We fix  $M$  to the maximum length observed in the training set under this discretization; shorter sequences are right-padded and a binary mask excludes padded indices from the loss. At inference, the terminal index is  $\hat{j}_i = \arg \max_j \hat{s}_{i,j}$ , and the predicted curve is truncated at  $\hat{j}_i$ .

#### 5.4.4 Training Details

The model was trained end-to-end using the loss from Eq. 5.5. The NAdam [220] optimizer was used with an initial learning rate of  $1 \times 10^{-4}$ . Additionally, a learning rate scheduler was employed to adjust the learning rate dynamically based on the validation loss. Specifically, the ReduceLROnPlateau scheduler was configured to reduce the learning rate by a factor of 0.1 if the validation loss did not improve for 10 epochs. The model was trained for 400 epochs, with early stopping based on the validation loss to further prevent overfitting. In all experiments, data were partitioned into train/validation/test sets in an 80/10/10 ratio at the acquisition-sequence level to avoid temporal leakage, with all frames from the same sequence – and their bi-planar counterparts (cameras A/B) and with/without-flow pairs – kept within the same split (a fixed random seed ensured reproducibility).

#### 5.4.5 Shape Prediction Network

The task is formulated as a supervised regression problem: given a 2D image  $I \in \mathbb{R}^{80 \times 80}$  of the guidewire, the network predicts a set of 3D coordinates  $\hat{y} = \{\hat{y}_1, \dots, \hat{y}_n\}$  corresponding to the reconstructed guidewire shape. Each sample thus maps from a single-channel image input to a variable-length sequence of 3D spatial positions in  $\mathbb{R}^3$  that represent the underlying geometry of the guidewire.

After deriving the reconstruction of the guidewire shape, [3D Fluoroscopy Guidewire Reconstruction Network \(3D-FGRN\)](#) is trained to approximate the instrument shapes from 2D images. [3D-FGRN](#) is composed of two main parts: a convolutional feature extraction module and a linear classification module. The convolutional module consists of three convolutional layers with kernel sizes of  $3 \times 3$  and filter depths of 32, 64, and 128, respectively. Each convolutional layer is followed by a [Rectified Linear Unit \(ReLU\)](#) [190] activation function, which introduces non-linear transformations essential for intricate pattern delineation. Max-pooling layers [221] with a window size of  $2 \times 2$  are interspersed after each activation, aiming to reduce spatial dimensionality and enhance the representational potency of the extracted feature maps.

The linear classification module, following the convolutional block, consists of two fully connected layers of sizes 256 and 128, each followed by a [ReLU](#) activation and a dropout layer [222] with dropout rate  $p = 0.3$  as a regularization technique. The final output layer maps to the predicted 3D positions of the guidewire points.

The training dataset is composed of image observations of shape  $80 \times 80$  paired with the derived 3D positions,  $p$ , of the guidewire bodies, enabling the model to learn the mapping from 2D images to the reconstructed 3D shapes. The [Convolutional Neural Network \(CNN\)](#) is optimized using the NAdam [220] optimizer, with a refined loss function that combines the Huber Loss and a regularization term to ensure both the accuracy of the predictions and the

preservation of the geometric structure of the guidewire.

The Huber Loss,  $\mathcal{L}_{\text{Huber}}$ , is defined as:

$$\mathcal{L}_{\text{Huber}}(y, \hat{y}) = \begin{cases} \frac{1}{2}(y - \hat{y})^2 & \text{if } |y - \hat{y}| < 1 \\ |y - \hat{y}| - \frac{1}{2} & \text{otherwise} \end{cases} \quad (5.6)$$

Here,  $y$  represents the ground truth, the derived 3D positions of the guidewire bodies, and  $\hat{y}$  represents the predicted positions by the model.

To maintain the geometric integrity of the guidewire, a regularization term,  $\mathcal{L}_{\text{reg}}$ , is introduced, which penalizes the deviation of the interbody spacing from  $s = 0.002$  m. This spacing value was chosen to match the simulation configuration, ensuring consistency between the physical model and its simulated counterpart and allowing for direct comparison of deformation behaviour.

$$\mathcal{L}_{\text{reg}} = \frac{1}{n-1} \sum_{i=1}^{n-1} \left| \|\hat{y}_{i+1} - \hat{y}_i\|_2 - s \right| \quad (5.7)$$

The final loss function,  $\mathcal{L}$ , is a weighted sum of the Huber Loss and the regularization term, ensuring both accurate predictions and preservation of the guidewire's geometric structure:

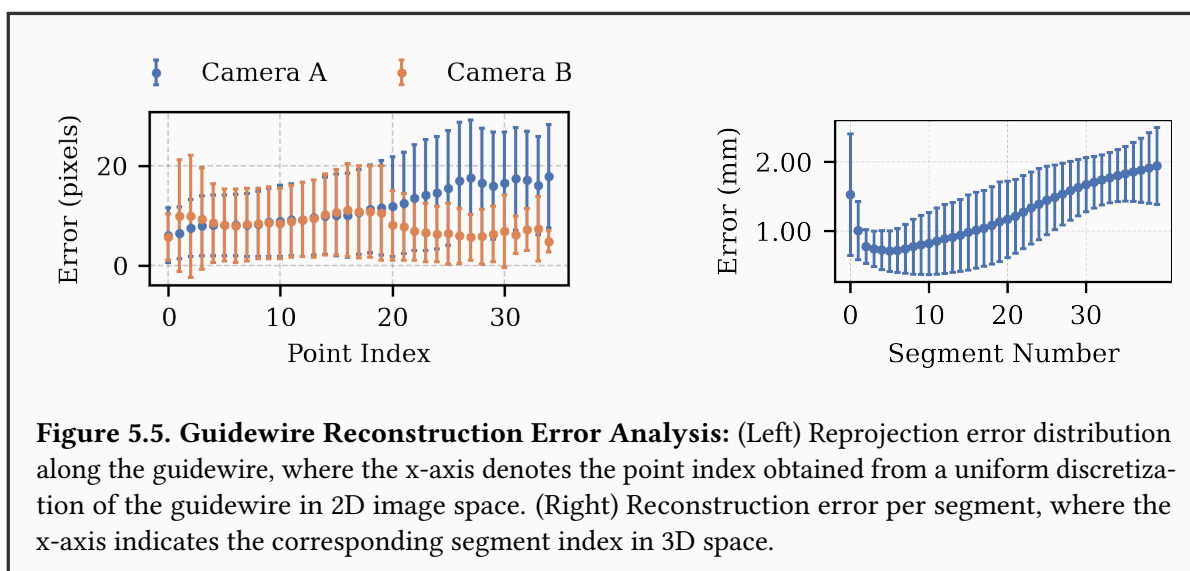
$$\mathcal{L} = \alpha \mathcal{L}_{\text{Huber}}(y, \hat{y}) + \beta \mathcal{L}_{\text{reg}} \quad (5.8)$$

Similarly to the 3D reconstruction, a univariate spline interpolation [223] is applied to the 3D points, thus getting a smooth representation of the guidewire.

## 5.5 Experiments

The proposed dataset, Guide3D, is evaluated through a structured experimental analysis, focusing on three key aspects. First, the dataset’s validity is assessed by analysing reprojection errors and their distribution to evaluate its accuracy and reliability (Subsection 5.5.1). Next, the applicability of Guide3D in the context of a 3D reconstruction task is investigated, examining its effectiveness in accurately modelling 3D shapes (Subsection 5.5.2). Finally, multiple segmentation algorithms are benchmarked to evaluate their performance on Guide3D, providing a comprehensive understanding of the dataset’s utility for segmentation tasks (Section 5.5.3).

### 5.5.1 Dataset Validation



The analysis revealed a non-uniform distribution of reprojection errors across the dataset, with the highest variability and errors concentrated at the proximal end of the guidewire reconstructions. As shown in Figure 5.5, the reprojection error patterns differ significantly between Camera A and Camera B. For Camera A, mean errors increase progressively from approximately 6px to a peak of 20px, with standard deviations rising from 5px to 11px, indicating both growing inaccuracies and increasing variability over time. Notably, significant fluctuations around indices 25 to 27 correspond to periods of particularly high error. In contrast, Camera B demonstrates an initial peak in mean errors at 9px at index 1, followed by fluctuations that diminish towards the dataset’s end. The standard deviations for Camera B start at 11px and decrease over time, reflecting high initial variability that stabilizes later. These patterns align with the inherent flexibility of the guidewire, which is capable of forming complex shapes such as loops.

Additionally, a validation procedure was conducted using CathSim [123], incorporating the

aortic arch model detailed in Subsection 5.3.1 and a guidewire with comparable diameter and mechanical properties. For sampling, the **Soft Actor Critic (SAC)** algorithm was employed, leveraging segmented guidewire and kinematic data to generate realistic validation samples. Evaluation metrics revealed a **Maximum Euclidean Distance (MaxED)** of  $2.880 \pm 0.640\text{mm}$ , a **Mean Error in Tip Tracking (METE)** of  $1.527 \pm 0.877\text{mm}$ , and a **Mean Error related to the Robot's Shape (MERS)** of  $0.001 \pm 0.000\text{mm}$ . These results confirm the precision and reliability of the proposed methodology.

## 5.5.2 Guidewire Prediction Results

| Table 5.3. Shape Comparison (mm). |                  |                                   | Table 5.4. Segmentation Results. |              |              |              |
|-----------------------------------|------------------|-----------------------------------|----------------------------------|--------------|--------------|--------------|
|                                   | Cartesian        | Spherical                         |                                  | DiceM        | mIoU         | Jaccard      |
| MaxED ↓                           | $10.00 \pm 4.64$ | <b><math>6.88 \pm 5.23</math></b> | UNet [205]                       | 92.25        | 36.60        | 86.57        |
| METE ↓                            | $6.93 \pm 3.94$  | <b><math>3.28 \pm 2.59</math></b> | TransUnet [224]                  | <b>95.06</b> | <b>41.20</b> | <b>91.10</b> |
| MERS ↓                            | $5.33 \pm 2.73$  | <b><math>4.54 \pm 3.67</math></b> | SwinUnet [225]                   | 93.73        | 38.58        | 88.55        |

The capability of the network introduced in Section 5.4 is demonstrated, highlighting the importance of the proposed dataset. The network's predictions are evaluated through the following steps: 1) an analysis of the predicted versus reconstructed curves using piecewise metrics, and 2) an examination of the reprojection error.

### 5.5.2.1 Shape Prediction Errors

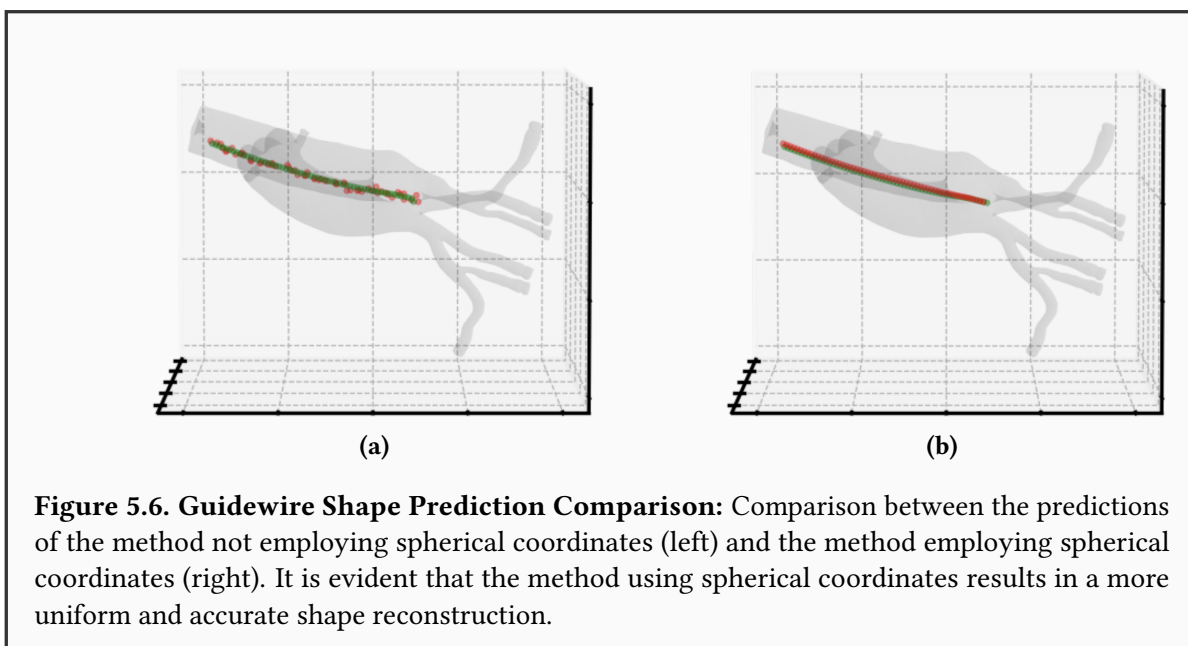
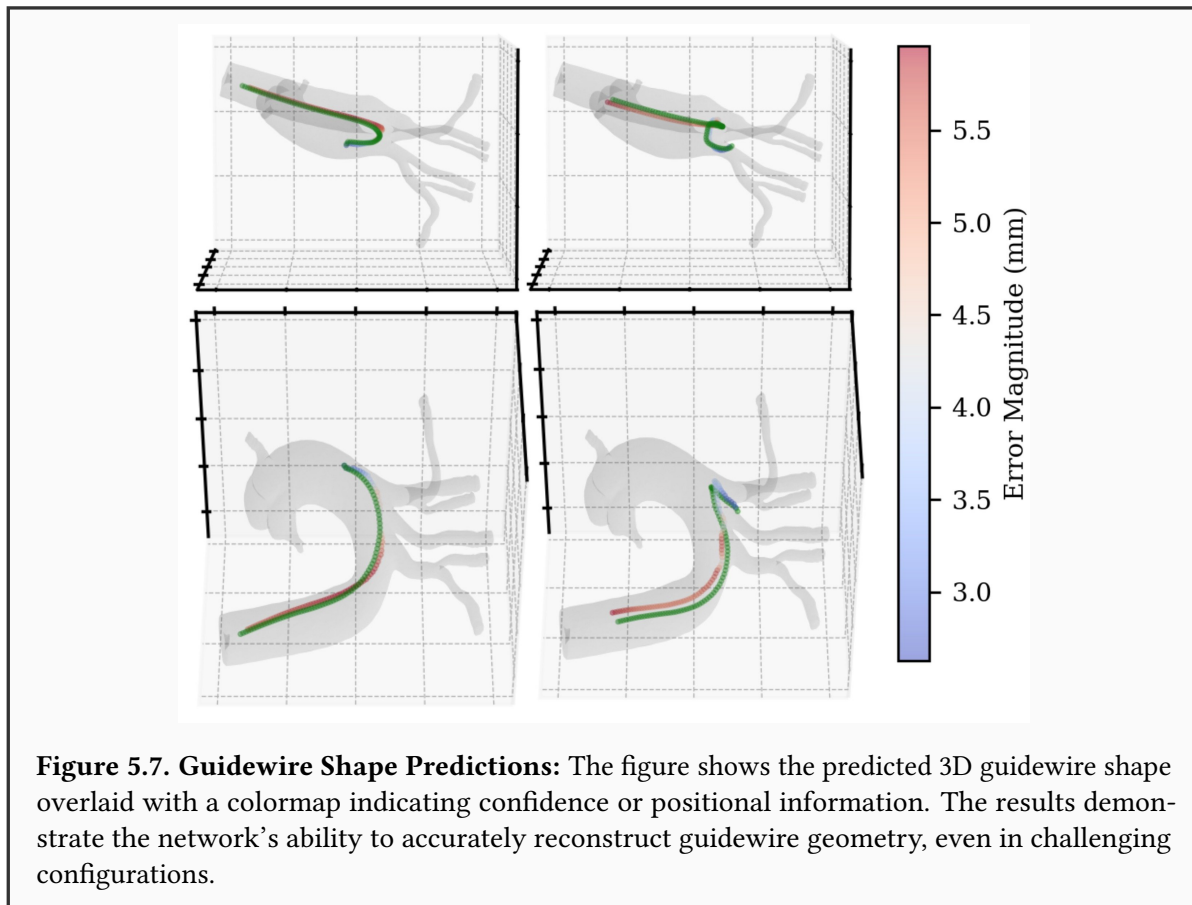


Table 5.3 presents a comparison of various metrics for shape prediction accuracy. As outlined in Subsection 5.5.1, the shape differences are quantified using the following metrics: 1) **Maximum**

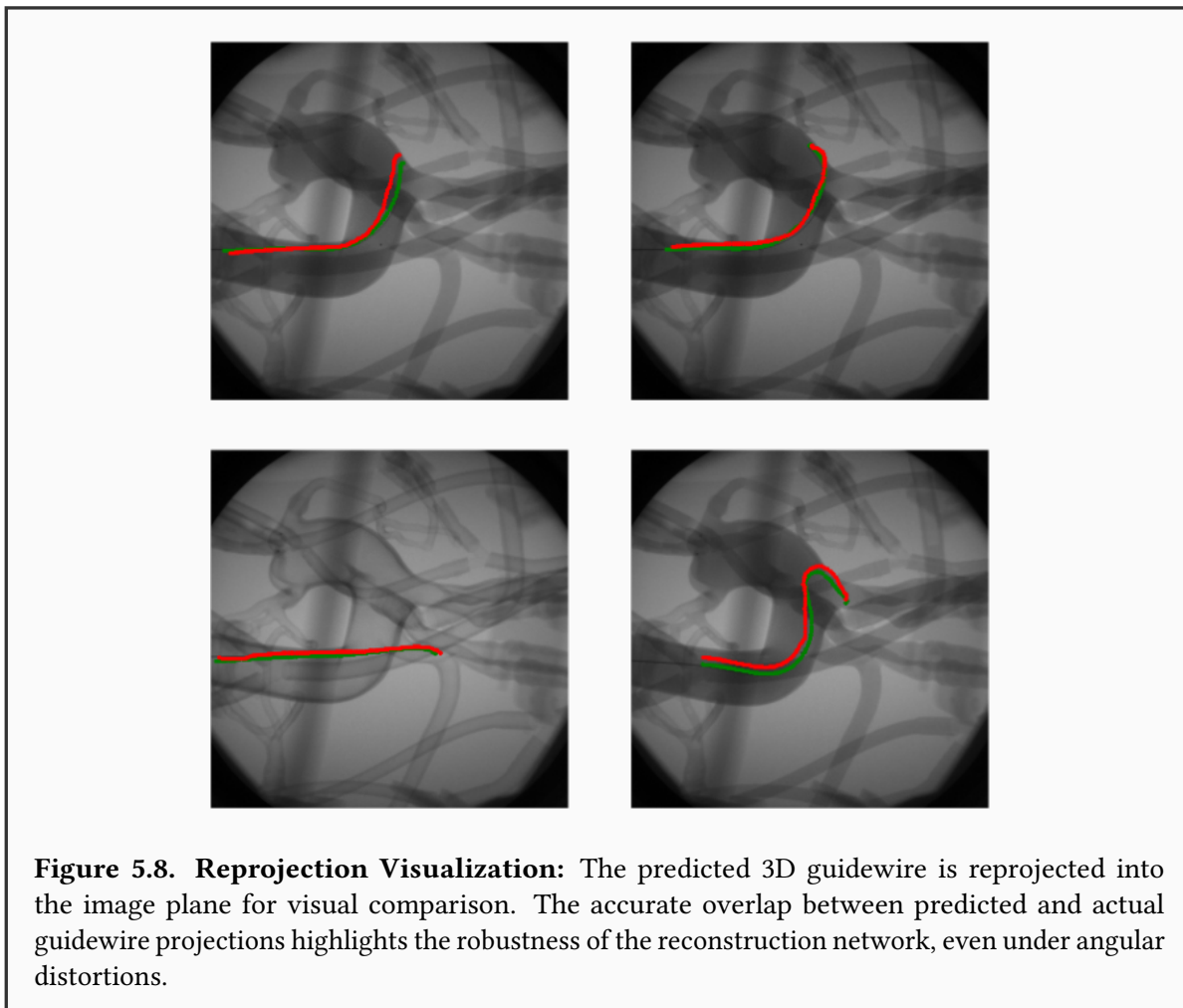


Euclidean Distance (MaxED), 2) Mean Error in Tip Tracking (METE), and 3) Mean Error related to the Robot's Shape (MERS). For consistency, the shape of the guidewire, represented as a 3D curve  $C(u)$ , is sampled at equidistant  $\Delta u$  intervals along the arclength parameter  $u$ . Consequently, these metrics reflect the pointwise discrepancies between the predicted and reconstructed shapes along the curve's arclength.

The results demonstrate that the Spherical representation consistently outperforms the Cartesian representation across all metrics. Specifically, the MaxED error is significantly lower for the Spherical representation ( $6.88 \pm 5.23\text{mm}$ ) compared to the Cartesian representation ( $10.00 \pm 4.64\text{mm}$ ). Similarly, the METE is reduced in the Spherical representation ( $3.28 \pm 2.59\text{mm}$ ) compared to the Cartesian representation ( $6.93 \pm 3.94\text{mm}$ ). For the MERS, the Spherical representation achieves a smaller error ( $4.54 \pm 3.67\text{mm}$ ) than the Cartesian representation ( $5.33 \pm 2.73\text{mm}$ ). Finally, the Fréchet distance further underscores the superiority of the Spherical representation, with a lower error ( $6.70 \pm 5.16\text{mm}$ ) compared to the Cartesian representation ( $8.95 \pm 4.37\text{mm}$ ). This can also be visually observed in Fig. 5.6.

### 5.5.2.2 Shape Comparison Visualization

Figure 5.7 presents two 3D plots from different angles, comparing the ground truth guidewire shape to the predicted shape generated by the network. The network demonstrates strong

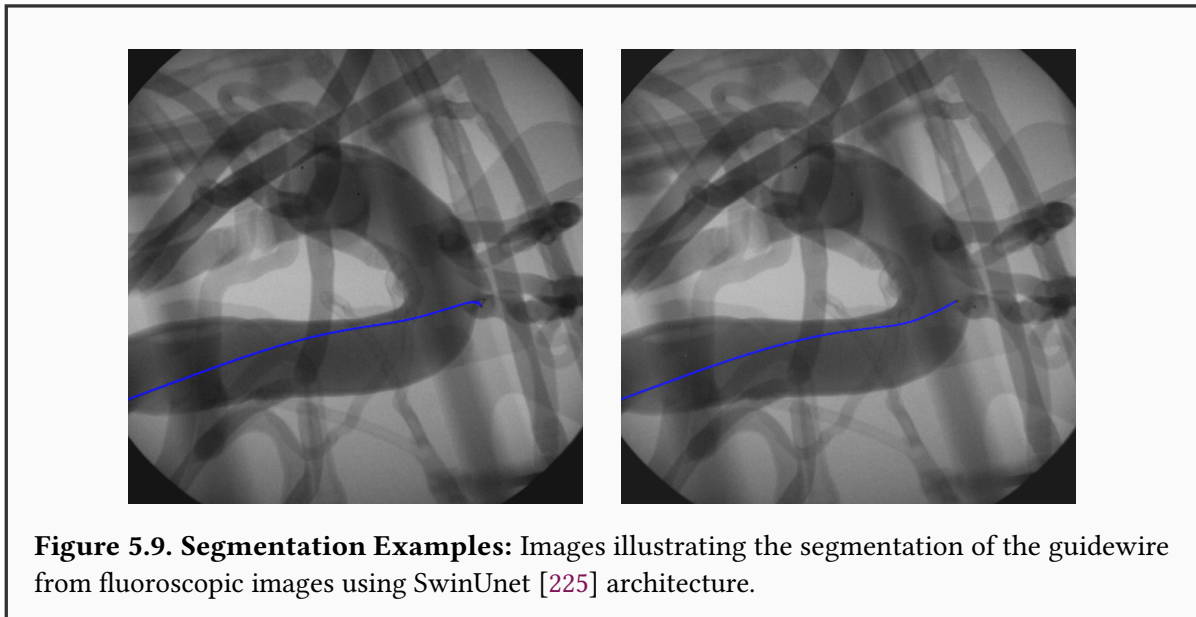


capability in accurately predicting the guidewire’s configuration, even in challenging scenarios involving loops and self-obstructions in the images. The predicted shape closely aligns with the ground truth, highlighting the effectiveness of the network in handling complex guidewire geometries.

Notably, the proximal end exhibits a greater deviation compared to the distal end, with discrepancies ranging from 2mm at the distal end to 5mm at the proximal end. These results underscore the network’s robustness in predicting the guidewire’s shape, leveraging only consecutive single-plane images. To validate the predictions further, the 3D points are reprojected onto the original images, as illustrated in Figure 5.8, demonstrating consistent alignment with the input data.

### 5.5.3 Segmentation Results

The potential of Guide3D to advance guidewire segmentation research is evaluated by assessing the performance of three state-of-the-art network architectures: 1) UNet [205], 2) TransUnet [224], and 3) SwinUnet [225]. The models were trained under the following configurations: UNet with a learning rate of  $1 \times 10^{-5}$  for 135 epochs, TransUnet incorporating ResNet50 and



Vision Transformer (ViT-B-16) with a learning rate of 0.01 for 199 epochs, and SwinUnet based on the Swin Transformer architecture with a learning rate of 0.01 for 299 epochs.

Performance metrics included the Dice Coefficient (DiceM), mean **Intersection over Union (mIoU)**, and Jaccard index, as summarized in Table 5.4. Among the models, TransUnet achieved the highest performance, with a **Dice Coefficient (DiceM)** of 95.06, an **mIoU** of 41.20, and a Jaccard index of 91.10. SwinUnet followed with a **DiceM** of 93.73, an **mIoU** of 38.58, and a Jaccard index of 88.55, while UNet achieved a **DiceM** of 92.25, an **mIoU** of 36.60, and a Jaccard index of 86.57. Fig. 5.9 presents example outputs from SwinUnet, illustrating its ability to segment the guidewire in fluoroscopic images.

These findings benchmark the dataset's performance and highlight the efficacy of modern transformer-based architectures, particularly TransUnet, for guidewire segmentation tasks. However, challenges such as loops and occlusions in the guidewire remain, suggesting that incorporating polyline prediction methods could significantly enhance the dataset's utility for complex scenarios.

## 5.6 Discussion and Conclusion

In this study, **Guide3D** is introduced, a publicly available bi-planar endovascular navigation dataset designed for the segmentation and 3D reconstruction of flexible, curved endovascular tools, addressing a significant gap in medical imaging research. While extensive experiments demonstrate the dataset's value, limitations are acknowledged, such as the absence of clinical real human data due to regulatory challenges and the focus on synthetic and experimental scenarios that may not fully capture the variability of real-world clinical environments. Nevertheless, the standardized platform accommodates both video and image-based approaches, providing a versatile resource to facilitate the translation of these technologies into clinical settings. By including complexities like the guidewire's flexibility and the presence of loops and occlusions, the aim is to push the boundaries of current methodologies, although further validation with clinical data is necessary to ensure robustness and generalizability. The objective is to bridge the disparity between research developments and clinical application by establishing a standardized framework for evaluating various methodologies.

The Guide3D dataset represents a significant contribution to the field by providing researchers with a high-quality, annotated resource that captures the complex dynamics of endovascular tools. With over 8,700 annotated images across varied flow conditions, it enables systematic evaluation and comparison of different reconstruction approaches. This comprehensive dataset not only facilitates algorithm development but also establishes benchmarks for performance metrics in the domain. The dataset introduced in this chapter provides the foundation for developing advanced geometric modelling techniques, which will be explored in the next chapter through the SplineFormer model for guidewire shape prediction.

## Chapter 6

---

# SplineFormer

*Endovascular navigation constitutes a critical component of minimally invasive procedures, where the precise manipulation of curvilinear instruments, such as guidewires, is essential for successful intervention. One of the primary challenges in this domain involves the accurate prediction of the guidewire’s evolving shape as it traverses the vascular system. This task is complicated by the complex deformations that result from continuous interaction with vessel walls. Traditional segmentation-based approaches often fail to deliver reliable real-time shape estimations, limiting their utility in highly dynamic clinical environments. To overcome these limitations, a novel transformer-based architecture, SplineFormer, is proposed for predicting the continuous and smooth shape of the guidewire in an interpretable manner. By leveraging the inherent attention mechanisms of transformers, the model effectively captures intricate patterns of bending and twisting, and represents the guidewire trajectory as a B-spline. This formulation enhances both the accuracy and smoothness of the predicted shape. The proposed SplineFormer model is integrated into an end-to-end robotic navigation framework, where its compact and informative representation contributes directly to autonomous decision-making. Experimental evaluations demonstrate that the SplineFormer enables autonomous endovascular navigation and achieves a success rate of 50% in cannulating the brachiocephalic artery using a real robotic platform.*

This chapter presents the work from the following publications:

**Jianu, T. et al.**, “Splineformer: An explainable transformer-based approach for autonomous endovascular navigation,” in *International Conference on Intelligent Robots and Systems (IROS)* - Under Review, IEEE, 2025

## 6.1 Introduction

Cardiovascular diseases remain the leading cause of mortality globally, accounting for over one million deaths annually. Among these, coronary heart disease and cerebrovascular disease represent the most prevalent contributors [2]. To address these conditions, endovascular interventions—such as [Percutaneous Coronary Intervention \(PCI\)](#), [Pulmonary Vein Isolation \(PVI\)](#), and [Mechanical Thrombectomy \(MT\)](#)—have become essential clinical procedures [3, 4, 5, 227]. These minimally invasive techniques involve the insertion and navigation of guidewires and catheters through the vascular system to reach target anatomical sites, guided by real-time intraoperative fluoroscopy. Upon reaching the destination, therapeutic actions such as thrombus removal, stent deployment, or tissue ablation are carried out to restore vascular function [6].

Despite their efficacy, the success of these procedures is highly time-sensitive. In the case of acute ischaemic stroke, for example, delays beyond approximately 7.3 hours significantly reduce the effectiveness of [MT](#) [10]. However, only a limited proportion of eligible patients receive treatment within the optimal therapeutic window, primarily due to logistical delays and procedural inefficiencies [228]. These limitations underscore the need for technologies that can enhance both the speed and precision of endovascular navigation.

Fluoroscopic imaging remains central to these interventions, providing real-time visualization of the vasculature to guide instruments accurately. However, this reliance introduces several risks, including cumulative radiation exposure to patients and clinicians, and potential nephrotoxicity from contrast agents [8]. In addition, the manual manipulation of guidewires and catheters requires a high degree of surgical dexterity and experience, contributing to the potential for complications such as vessel perforation, distal embolization, or loss of device control [9]. These challenges point to a clear need for advanced robotic assistance and automation strategies capable of reducing operator dependency and improving procedural safety and consistency.

Recent advances in [Machine Learning \(ML\)](#) have demonstrated considerable potential to overcome many of the aforementioned limitations [229]. Among these, [Reinforcement Learning \(RL\)](#) has emerged as a particularly promising approach for enabling precise and efficient navigation in endovascular settings. These algorithms are capable of learning complex control policies in highly dynamic and constrained environments [86, 89, 90, 91, 103]. Nonetheless, the application of [RL](#) to real-world clinical settings remains limited, due in part to its reliance on controlled environments, specialized robotic platforms, and the absence of haptic feedback [16, 17]. Moreover, considerations related to safety, explainability, and ethical implementation remain critical as these technologies progress toward clinical deployment [230].

In response to these challenges, a novel transformer-based model—**SplineFormer**—is in-

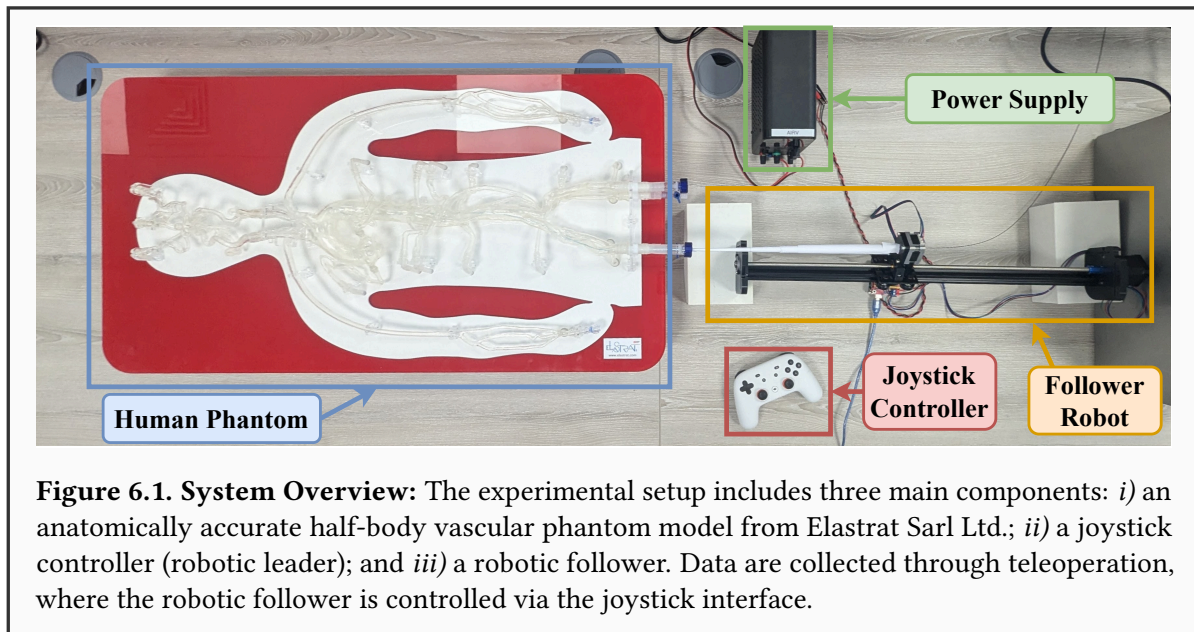


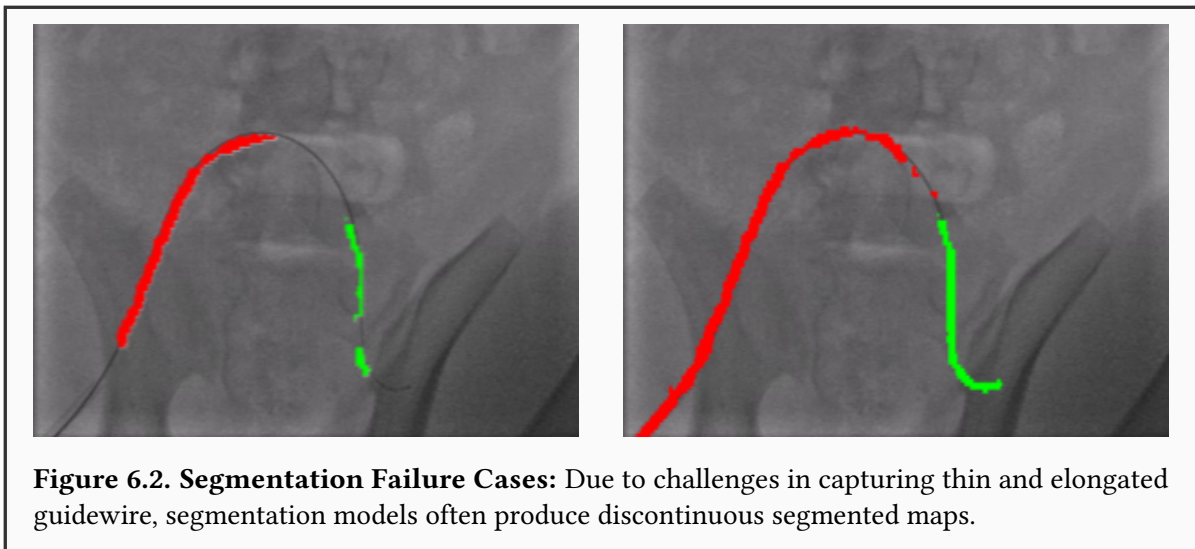
**Figure 6.1. System Overview:** The experimental setup includes three main components: *i*) an anatomically accurate half-body vascular phantom model from Elastrat Sarl Ltd.; *ii*) a joystick controller (robotic leader); and *iii*) a robotic follower. Data are collected through teleoperation, where the robotic follower is controlled via the joystick interface.

troduced. This architecture is designed to exploit the geometrical structure of guidewires through the use of B-spline representations. In contrast to conventional segmentation-based methods for navigation [88, 130, 231], SplineFormer provides an interpretable and continuous representation that is directly compatible with robotic navigation systems for endovascular procedures. The proposed approach is validated experimentally using a high-fidelity human vascular phantom and robotic setup (see Fig. 6.1), demonstrating the feasibility of autonomous guidewire navigation in a physical environment.

The main contributions of this work are summarized as follows:

- A transformer-based architecture, **SplineFormer**, is proposed for learning B-spline representations of guidewire shapes, enabling smooth and geometrically constrained modelling of instrument trajectories.
- A training framework is designed to optimize SplineFormer for *(i)* learning compact, semantically meaningful representations of guidewire shapes and *(ii)* generating control actions for autonomous navigation through complex vascular anatomies.

## 6.2 Related Works



**Guidewire and Catheter Segmentation.** Accurate modelling of guidewires and catheters is a critical challenge in endovascular interventions, as it directly impacts the precision of robotic navigation. Traditional approaches have predominantly relied on segmentation-based methods, wherein the guidewire is identified from fluoroscopic images using classical image processing techniques such as pixel intensity analysis, texture feature extraction, and histogram-based methods [232], [233], [234], [235], [236]. More advanced methodologies, including the Hough transform and curvature-based techniques, have been employed to enhance detection accuracy [237], [238], [239]. However, these approaches often exhibit limitations in the presence of low contrast, occlusions, and imaging artefacts, thereby reducing their reliability for real-time navigation in dynamic clinical environments.

Deep learning methods have introduced more robust solutions for guidewire detection and segmentation. [Convolutional Neural Network \(CNN\)](#)s have been widely adopted for surgical tool localization, demonstrating significant improvements in accuracy [110], [240], [241], [242], [243]. In particular, U-Net-based architectures [205] have achieved state-of-the-art performance in segmenting guidewires from X-ray images, with refinements such as [Recurrent Neural Network \(RNN\)](#)s and adaptive binarization further improving accuracy [200], [244]. However, these methods primarily operate on pixel-wise segmentations, which fail to provide a structured, continuous representation of the guidewire’s geometry. One common failure mode is fragmentation, where discontinuities appear in the predicted segmentation mask (Fig. 6.2), making it unsuitable for stable robotic navigation [245].

Unlike segmentation-based methods, B-spline representations offer a structured and interpretable formulation of the guidewire’s geometry. By parameterizing the guidewire as a set of control points, B-splines inherently enforce smoothness and geometric consistency,

thereby reducing sensitivity to noise and enhancing navigation stability. This parametric representation is particularly advantageous for robotic applications, where compact, continuous state encodings are preferable to high-dimensional, pixel-wise outputs. Building upon this principle, the proposed approach leverages SplineFormer to directly predict B-spline parameters, enabling seamless integration into downstream robotic navigation policies.

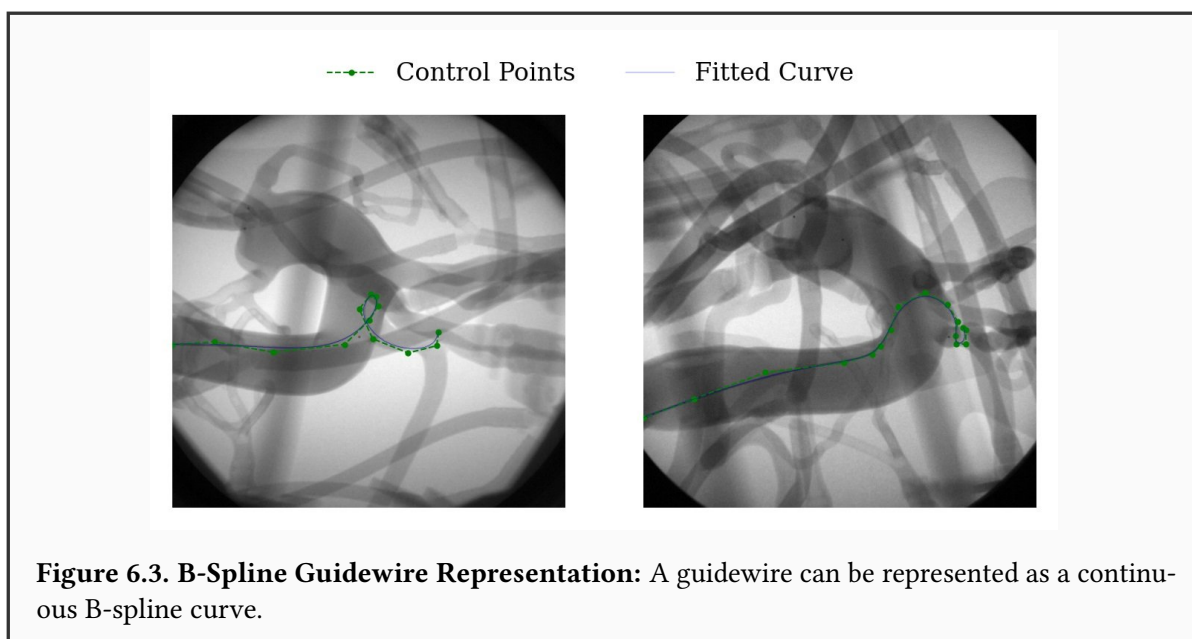
**Autonomous Navigation.** Autonomous navigation of guidewires within the vasculature is a highly complex task that has garnered significant attention due to its potential benefits, including reduced operative times, minimized radiation exposure, and improved procedural success rates. Recent advancements have increasingly focused on learning-based approaches to enhance the autonomous control of surgical tools, leveraging data-driven models to improve precision, adaptability, and robustness in dynamic clinical environments. [Reinforcement Learning \(RL\)](#) has been extensively explored in endovascular navigation, demonstrating the capability to learn complex control policies [86], [88], [89], [90], [91], [174], [231]. Various RL-based approaches have been proposed to train agents for autonomous guidewire navigation. However, their performance is highly contingent on the quality of the state representation. Many existing methods rely on raw image-based observations, which are inherently high-dimensional and lack an explicit geometric structure, posing challenges for interpretability and efficient decision-making.

To mitigate these challenges, several studies have integrated [Learning from Demonstration \(LfD\)](#) techniques, such as [Generative Adversarial Imitation Learning \(GAIL\)](#) [88] and [Behavioural Cloning \(BC\)](#) [231], where expert trajectories serve as supervisory signals to guide learning. These approaches have demonstrated potential in reducing the sample complexity of RL algorithms by incorporating expert knowledge. However, existing methods often suffer from poor generalization due to the absence of structured state representations. In contrast, the proposed approach employs B-spline representations to construct a compact and structured state space, facilitating more stable and interpretable endovascular navigation.

## 6.3 B-Spline Representation for Autonomous Endovascular Navigation

Accurate geometric modelling of curvilinear guidewires and catheters is essential for precise navigation and control in interventional procedures. Conventional approaches primarily rely on dense image-based representations [107], which capture the tool’s shape at the pixel level but lack an intrinsic parametric structure suitable for real-time navigation. To overcome these limitations, SplineFormer (Fig. 6.4) is developed, adopting a B-spline-based representation to encode the guidewire’s shape in a compact, continuous, and structured form. By directly parameterizing the guidewire’s geometry, this approach eliminates the need for post-processing steps required by segmentation-based methods, facilitating seamless integration into downstream robotic navigation policies.

### 6.3.1 B-Spline Representation for Guidewire Modelling



A B-spline curve represents the guidewire’s shape using a set of control points and a non-decreasing sequence of knots, providing a smooth and flexible parametric formulation (Fig. 6.3). This structured encoding inherently enforces continuity and geometric consistency, enabling stable and anatomically realistic trajectory adjustments during navigation. A B-spline curve  $C(t)$  of degree  $p$  is defined as:

$$C(t) = \sum_{i=0}^n P_i B_{i,p}(t), \quad (6.1)$$

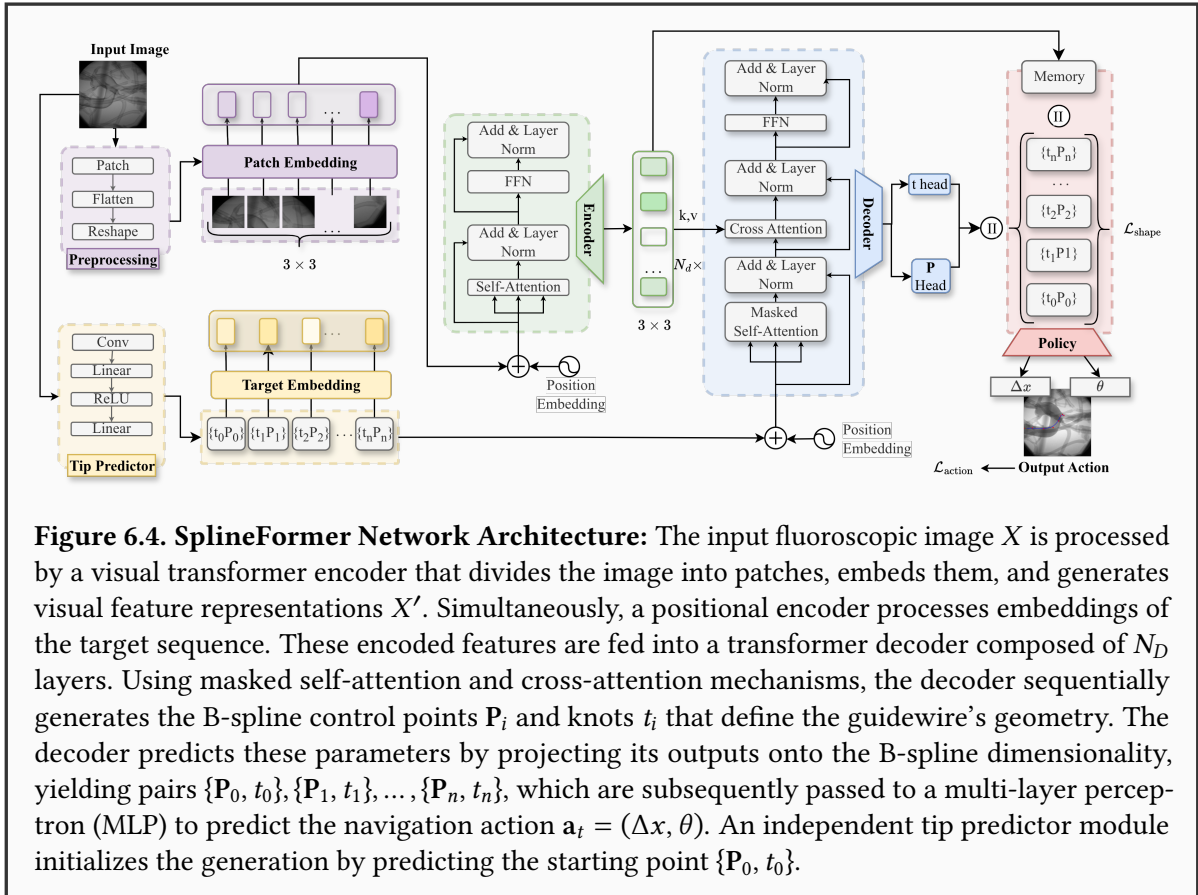
where  $P_i$  denotes the control points, and  $B_{i,p}(t)$  represents the B-spline basis functions of

degree  $p$ , defined over the knot vector  $t_0, t_1, \dots, t_m$ . The basis functions  $B_{i,p}(t)$  are computed recursively as follows:

$$B_{i,0}(t) = \begin{cases} 1, & \text{if } t_i \leq t < t_{i+1}, \\ 0, & \text{otherwise.} \end{cases} \quad (6.2)$$

$$B_{i,p}(t) = \frac{t - t_i}{t_{i+p} - t_i} B_{i,p-1}(t) + \frac{t_{i+p+1} - t}{t_{i+p+1} - t_{i+1}} B_{i+1,p-1}(t) \quad (6.3)$$

Additionally, the constraint  $\sum_{i=0}^{m-p-1} B_{i,p}(t) = 1$  ensures that the guidewire's shape remains consistent across varying imaging conditions, enabling real-time inference. To balance smoothness and computational efficiency, the B-spline degree is set to  $p = 3$ . The number of control points  $n$  is dynamically selected based on the guidewire's length, optimizing flexibility while maintaining model stability. The knot vector follows a uniform non-decreasing sequence, ensuring numerical robustness during optimization.



### 6.3.2 SplineFormer Network Architecture

SplineFormer (Fig. 6.4) is built upon a **Vision Transformer (ViT)** backbone [54] with  $N_e = 12$  encoder layers and  $N_D = 6$  decoder layers. Each encoder layer employs  $H = 8$  attention heads

with a hidden dimension of  $d_k = 512$ . Input fluoroscopic images are resized to  $224 \times 224$  pixels and tokenized into  $16 \times 16$  patches. The model is trained using the Adam optimizer on an NVIDIA A100 GPU with a batch size of 32, reaching convergence after 120K iterations.

**Encoder.** Two encoders are employed to extract structured features from fluoroscopic images, enabling precise guidewire representation for downstream navigation. The first encoder follows a ViT, where the input image  $X \in \mathbb{R}^{H \times W}$  is divided into  $N_p$  patches, computed as:

$$N_p = \frac{H}{|P|} \times \frac{W}{|P|}, \quad (6.4)$$

where  $|P|$  denotes the patch size. These patches are flattened into a 1D tensor and embedded into a latent feature space via a linear projection layer. The second encoder is a sinusoidal positional encoder [48], applied to both the image patches  $P$  and the target sequence  $Y_{\text{TGT}} \in \mathbb{R}^{S \times E}$ , where  $S$  and  $E$  denote the sequence length and embedding dimension, respectively. This dual encoding mechanism ensures that the extracted features capture both local and global information, essential for accurately predicting the guidewire's shape.

The transformer encoder consists of  $N_e$  stacked identical layers, each comprising a **Multi-Head Self-Attention (MHA)** module followed by a positional **Feed-Forward Network (FFN)**. The **MHA** module contains  $H$  parallel attention heads, each computing a scaled dot-product attention function. This architecture enables the network to attend to both local and global contextual information, which is critical for capturing the intricate bending and twisting of the guidewire during navigation. The outputs from all heads are aggregated via a learnable linear transformation  $W^O$ , formulated as:

$$\text{MHA}(Q, K, V) = \text{Concat}(h_1, h_2, \dots, h_H)W^O, \quad (6.5)$$

where the scaled dot-product attention for each head is computed as:

$$\text{Attention}(Q, K, V) = \text{Softmax}\left(\frac{QK^T}{\sqrt{d_k}}\right)V, \quad (6.6)$$

where  $\{Q, K, V\} \in \mathbb{R}^{N_q \times d_k}$  represent the query, key, and value matrices, respectively.

Following the **MHA** module, the positional **FFN** is implemented using two fully connected layers with GELU activation and dropout regularization:

$$\text{FFN}(x) = \text{FC}_2(\text{Dropout}(\text{GELU}(\text{FC}_1(x)))) \quad (6.7)$$

To enhance stability, each sublayer is equipped with a residual connection, followed by layer

normalization:

$$x^{\text{out}} = \text{LayerNorm}(x^{\text{in}} + \text{Sublayer}(x^{\text{in}})) \quad (6.8)$$

**Decoder.** The decoder consists of  $N_D$  transformer layers that sequentially generate the B-spline control points and corresponding knots, defining the guidewire’s smooth representation. Each layer comprises masked self-attention, multi-head cross-attention, and a FFN [48]. This hierarchical structure enables the model to iteratively refine the predicted guidewire shape while capturing its curvature and spatial relationships in a compact form. The decoder’s final output is projected onto the B-spline parameter space, yielding the structured representation:

$$\{\mathbf{P}_0, t_0\}, \{\mathbf{P}_1, t_1\}, \dots, \{\mathbf{P}_n, t_n\}, \quad (6.9)$$

where  $\mathbf{P}_i$  are the control points and  $t_i$  are the associated knot values. This formulation defines the guidewire’s geometry as a continuous parametric curve  $C(t)$ , enabling accurate and interpretable navigation. By leveraging a structured and smooth state representation, this approach ensures both robust real-time inference and geometrically consistent trajectory estimation.

**Tip Predictor.** The tip predictor module establishes a geometrically consistent anchor for guidewire shape prediction by estimating the initial tip position in the image. It consists of a series of convolutional layers with Rectified Linear Unit (ReLU) activations, followed by linear transformations that regress the tip coordinates. Given an input image  $I$ , the module predicts the tip location:

$$\mathbf{P}_0 = (x_0, y_0), \quad (6.10)$$

which serves as the initial token for autoregressive guidewire prediction, ensuring that the generated trajectory remains spatially coherent and well-anchored.

The encoder and tip predictor interact in a complementary manner: the encoder extracts hierarchical guidewire features from the fluoroscopic image, while the tip predictor directly predicts the initial tip position from these encoder derived feature representations. By leveraging the multiscale contextual information captured by the encoder, such as vessel boundaries, local intensity patterns, and structural cues, the tip predictor gains a richer understanding of vessel topology, allowing it to produce a more precise and anatomically valid starting point. This is crucial, as an inaccurate tip estimation could introduce propagation errors in the subsequent trajectory prediction. The estimated tip  $\mathbf{P}_0$  is then passed to the decoder, which

generates the full guidewire trajectory based on this initialization.

### 6.3.3 Loss Function

The shape loss function  $\mathcal{L}_{\text{shape}}$  combines three weighted components, each scaled by a corresponding hyperparameter  $\lambda$ : (i) A [Mean Squared Error \(MSE\)](#) loss applied to the predicted and target sequences of control points and knots. (ii) A [Binary Cross-Entropy \(BCE\)](#) loss for the End-of-Sequence (EOS) prediction. (iii) A curvature consistency loss, computed by sampling the predicted B-spline curve at  $n$  parameter values  $t_k$ , uniformly distributed over the valid parameter range  $[t_p, t_{m-p}]$ .

The sampled parameter values are defined as:

$$t_k = t_p + \frac{k}{n-1}(t_{m-p} - t_p), \quad k = 0, 1, \dots, n-1 \quad (6.11)$$

The complete loss function is:

$$\begin{aligned} \mathcal{L}_{\text{shape}} = \frac{1}{N} \sum_{i=1}^N \left( \lambda_a (\|t_i - \hat{t}_i\|^2 + \|\mathbf{P}_i - \hat{\mathbf{P}}_i\|^2) + \right. \\ \lambda_b (-s_i \log(\hat{s}_i) - (1 - s_i) \log(1 - \hat{s}_i)) + \\ \left. \lambda_c \|\mathbf{C}(t_k) - \hat{\mathbf{C}}(t_k)\|^2 \right) \end{aligned} \quad (6.12)$$

The output of SplineFormer is a predicted sequence of control points and knots. This sequence serves not only as a shape descriptor but also as the input state for downstream action prediction. By coupling shape inference directly to action generation, the model forms a single cohesive pipeline from image to navigation decision.

### 6.3.4 Policy Training

The predicted control points and knots from Eq. 6.9 are directly passed to a [Multi-Layered Perceptron \(MLP\)](#) that predicts the next navigation action. The MLP processes these inputs—along with derived curvature features—through fully connected layers with [ReLU](#) activations, producing:

$$\mathbf{a}_t = (\Delta x, \theta), \quad (6.13)$$

where  $\Delta x$  denotes the translation step and  $\theta$  denotes the rotation angle. This policy network is trained by minimizing the mean squared error between predicted and expert actions:

$$\mathcal{L}_{\text{action}} = \sum_t \|\mathbf{a}_t - \mathbf{a}_t^*\|^2 \quad (6.14)$$

This direct dependence between the predicted guidewire shape and the navigation action ensures that every control decision is grounded in the current estimate of the guidewire's geometry, providing both physical consistency and a structured link between perception and control.

## 6.4 Experiments

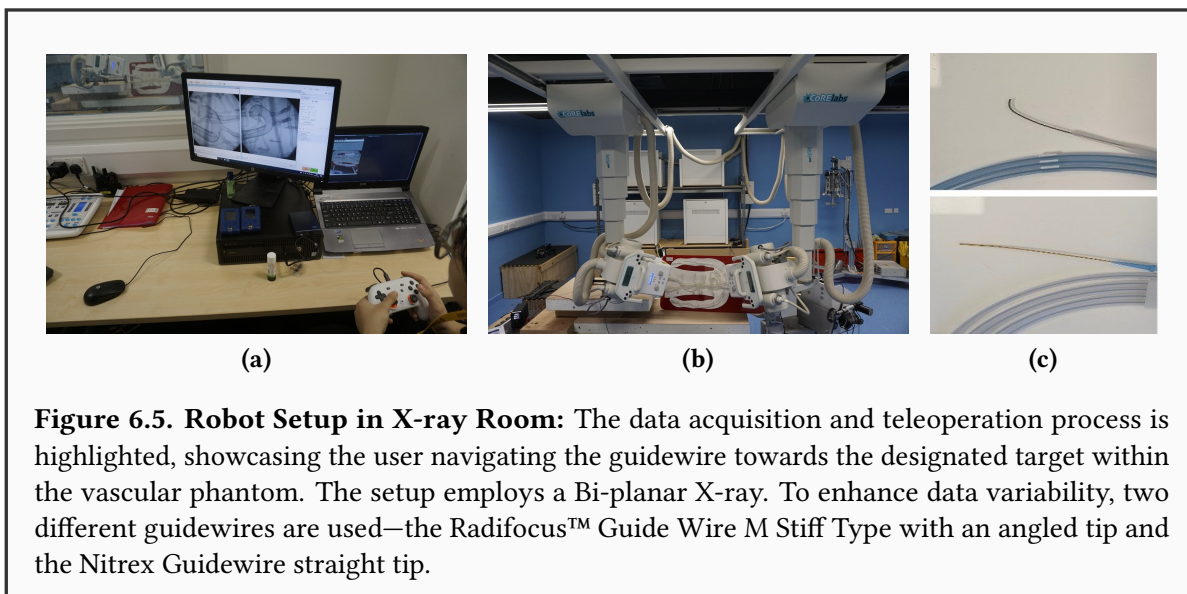


**Figure 6.5. Robot Setup in X-ray Room:** The data acquisition and teleoperation process is highlighted, showcasing the user navigating the guidewire towards the designated target within the vascular phantom. The setup employs a Bi-planar X-ray. To enhance data variability, two different guidewires are used—the Radifocus™ Guide Wire M Stiff Type with an angled tip and the Nitrex Guidewire straight tip.

To evaluate the effectiveness of SplineFormer, the real endovascular robot was set up and data were collected to train the network. After training, the learned policy was evaluated on state-action pairs within the endovascular robotic system to assess how effectively the predicted B-spline representation supports autonomous guidewire navigation. All experiments were conducted on a computer equipped with an NVIDIA RTX 4080 GPU, 128 GB RAM, and an Intel Core i9-13900 processor, implemented using PyTorch.

### 6.4.1 Endovascular Robot Setup

**Robot Setup.** Endovascular robotic systems commonly utilize a leader-follower (master-slave) architecture, where the leader device—operated by a clinician—translates input commands to a follower robot that manipulates the catheter [246]. These systems typically offer up to six Degree of Freedom (DoF), enabling precise translation and rotation control [247]. Human-Machine Interfaces (HMIs), such as multi-DoF joysticks or handheld controllers, convert operator movements into electromechanical actions, facilitating accurate catheter navigation [247], [248]. In the present system, since only a guidewire is used, the robotic setup is streamlined to focus solely on translation and rotation movements. This simplification reduces mechanical complexity, making the design more accessible and easier to replicate compared to multi-DoF systems. The actuation mechanism comprises a NEMA 17 Bipolar stepper motor (59 N cm, 2 A) for linear motion, along with an additional motor for rotational control. System control is managed by an Arduino Uno Rev3 with a CNC shield and two A4988 drivers, powered by a 12 V DC power supply. Teleoperation input is provided via a Google Stadia joystick for intuitive manual control.

**Data Collection.** The experiments utilize a Bi-planar X-ray system (Fig. 6.5) equipped with 60 kW Epsilon X-ray Generators (EMD Technologies Ltd.) and 16-inch Image Intensifier Tubes (Thales), incorporating dual focal spot Variant X-ray tubes for high-definition imaging. System calibration is achieved using acrylic mirrors and geometric alignment grids. To simulate human vascular anatomy, a half-body vascular phantom model (Elastrat Sarl Ltd., Switzerland) is employed, enclosed in a transparent box and integrated into a closed water circuit to replicate blood flow. The model, constructed from soft silicone and featuring continuous flow pumps, was derived from detailed postmortem vascular casts, ensuring anatomical accuracy consistent with human vasculature [150], [151]. A Radifocus™ Guide Wire M Stiff Type (Terumo Ltd.), a 0.89 mm nitinol wire with a 3 cm angled tip, and a Nitrex Guidewire with a straight tip were utilized.

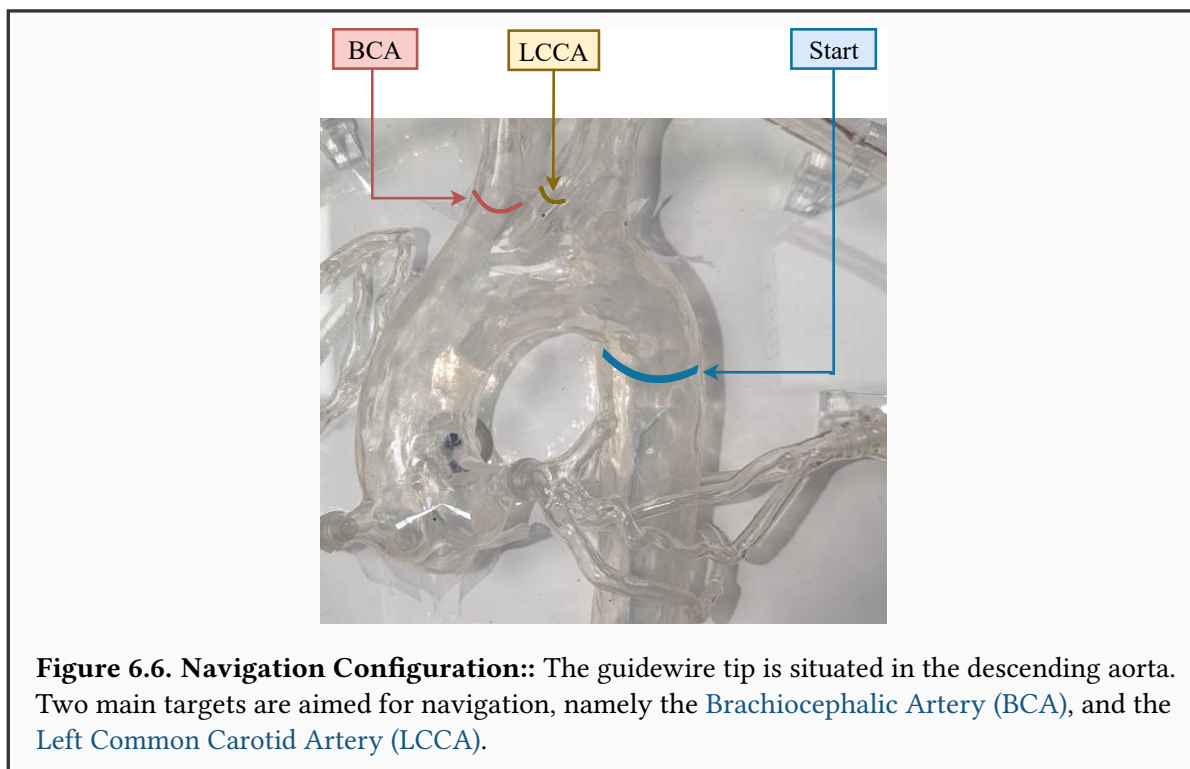
**Dataset.** A dataset of 8,746 high-resolution samples ( $1,024 \times 1,024$  pixels) was collected, consisting of 4,373 paired instances with and without a simulated blood flow medium. Specifically, the dataset includes 6,136 samples from the Radifocus Guidewire and 2,610 from the Nitrex Guidewire, establishing a foundation for automated guidewire tracking in bi-planar X-ray images. Manual annotation was performed using the CVAT tool [209], where polylines were meticulously created to capture the dynamic trajectory of the guidewire with high precision. To ensure balanced representation across different guidewire types and imaging conditions, the dataset was partitioned using a stratified sampling method.

## 6.4.2 Autonomous Navigation Results

SplineFormer was evaluated in a *fully autonomous* guidewire navigation task. The objective was to navigate from a predefined position in the descending aorta toward two distinct arterial targets: the **Brachiocephalic Artery (BCA)** and the **Left Common Carotid Artery (LCCA)**, as illustrated in Fig. 6.6. For each target, the system performed 20 trials, recording trajectories to construct datasets of state-action pairs. The agent operated using fluoroscopic image observations, with an action space defined by translation within  $\pm 2\text{mm}$  and rotation within  $\pm 15^\circ$ .

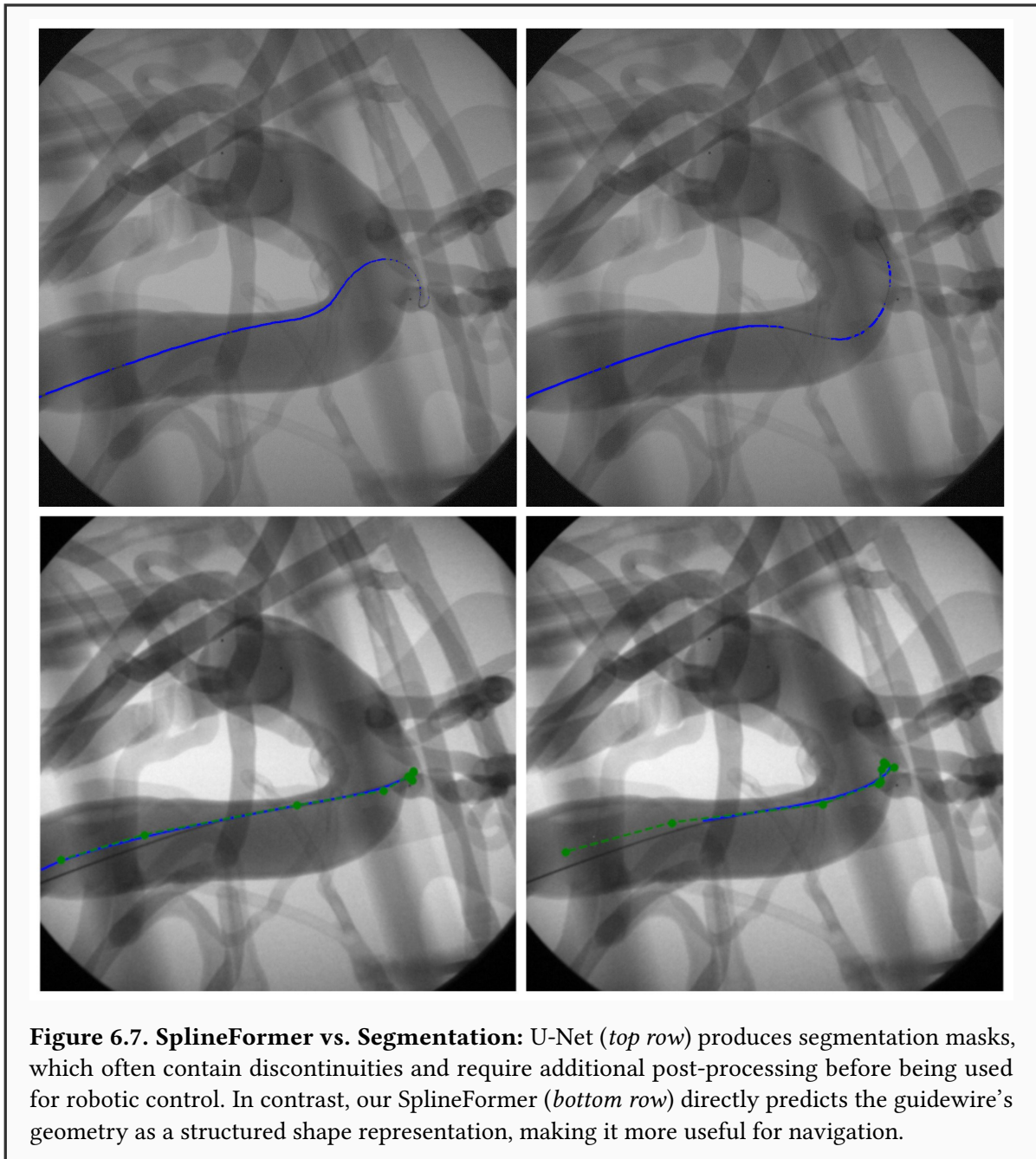
Following training, SplineFormer was deployed on the robotic platform for fully autonomous navigation. The system achieved a 50% success rate in reaching the **BCA**, with a mean completion time of  $2.50 \pm 0.76$  min. This represents a substantial improvement over the baseline **BCA** method, which achieved only 5.6% success under identical autonomous conditions. The semi-autonomous GAIL-PPO approach, which incorporates human demonstrations, performed better with success rates of 69.4% for the **BCA** and 72.2% for the **LCCA**, but unlike SplineFormer, it still required human intervention.

While this method did not surpass GAIL-PPO [88], a semi-autonomous approach, in success rate, it offers the advantage of full autonomy. Moreover, the B-spline representation provides

**Table 6.1.** Endovascular navigation results.

| Method                     | Setup            | Explainable? | BCA         |            | LCCA        |          |
|----------------------------|------------------|--------------|-------------|------------|-------------|----------|
|                            |                  |              | Success (%) | Time (s)   | Success (%) | Time (s) |
| Expert Teleoperation       | Fully Manual     | —            | 100.0       | 32.1       | 100.0       | 25.0     |
| GAIL-PPO[88]               | Semi-Autonomous  | No           | 69.4        | 52.1       | 72.2        | 76.5     |
| Behavior Cloning[88]       | Fully Autonomous | No           | 5.6         | $\geq 200$ | —           | —        |
| <b>Splineformer (Ours)</b> | Fully Autonomous | Yes          | 50.0        | 150.0      | —           | —        |

an explainable and structured state space, improving model interpretability. However, neither SplineFormer nor BC successfully cannulated the LCCA, highlighting challenges in navigating more complex vascular geometries. The failure in LCCA navigation can be attributed to its sharper curvature, narrower diameter, and more abrupt bifurcation angle compared to the BCA. As reflected in the success rates in Table 6.1, the guidewire was generally able to advance into the aortic arch and perform rotational manoeuvres, but it failed to align with and enter the ostium of the target branch. Instead, it bypassed the branch and continued within the arch, underscoring that the main limitation was branch cannulation rather than forward progression.



**Navigation Behaviour and Failure Modes.** Throughout the autonomous trials, successful navigation typically exhibited smooth and gradual trajectory adjustments, with the guidewire tip remaining aligned with the vessel centreline. In contrast, failure cases primarily involved two distinct behaviours: *i*) premature turning into an incorrect vessel branch due to ambiguous visual cues near bifurcations, and *ii*) overshooting, where the guidewire tip failed to decelerate or rotate sufficiently to align with and enter the ostium of the target vessel. These failures were particularly prevalent in the [LCCA](#) navigation task, where the vessel geometry presents sharper curvature, narrower diameters, and more abrupt branching angles compared to the [BCA](#). In most such cases, the guidewire continued advancing along the aortic

arch without successfully cannulating the intended branch, indicating that failure was due to spatial misalignment rather than mechanical instability. These observations highlight the need for improved spatial reasoning or the integration of geometric priors in future autonomous navigation models.

### 6.4.3 Qualitative Results

---

SplineFormer was trained for 300 epochs on the annotated dataset from Section 6.4.1 using the Adam optimizer with an initial learning rate of  $1 \times 10^{-5}$  and the loss function from Eq. 6.14. As illustrated in Fig. 6.7, the model effectively predicts the global guidewire shape within a compressed feature space, ensuring a compact and structured geometric representation. A key strength of SplineFormer is its ability to localize key guidewire points precisely. By leveraging a B-spline-based formulation, the model maintains smoothness and structural integrity, ensuring a continuous representation that aligns well with the guidewire’s physical properties.

### 6.4.4 Attention Visualization

---

To better understand how the model processes fluoroscopic images, attention maps were generated from SplineFormer’s transformer layers. Using maximal fusion across the final layer, with a discard factor to isolate key features, the resulting visualizations in Fig. 6.8 highlight the critical regions where the model concentrates its predictions. These attention maps reveal a strong focus on the guidewire tip and essential anatomical landmarks, including the central portion of the aortic arch and the [BCA](#) cannulation site.

Unlike traditional segmentation methods, where attention is often dispersed across large areas of the image, SplineFormer exhibits highly localized attention, refining its focus on the most relevant regions for navigation. This precise attention mechanism enhances stability and accuracy in guidewire positioning, improving the reliability of autonomous navigation.

However, not all attention outputs are ideal. In some cases, the attention maps highlight regions that do not correspond directly to anatomical structures or the guidewire. This behaviour is largely attributed to distortions inherent in X-ray imaging, such as noise, non-uniform contrast, and overlapping anatomical features, which may cause the model to attend to visually prominent but semantically irrelevant regions. These artefacts can reduce the reliability of attention interpretation in some frames. Addressing this limitation by incorporating domain-specific priors or preprocessing techniques remains an important direction for future work.

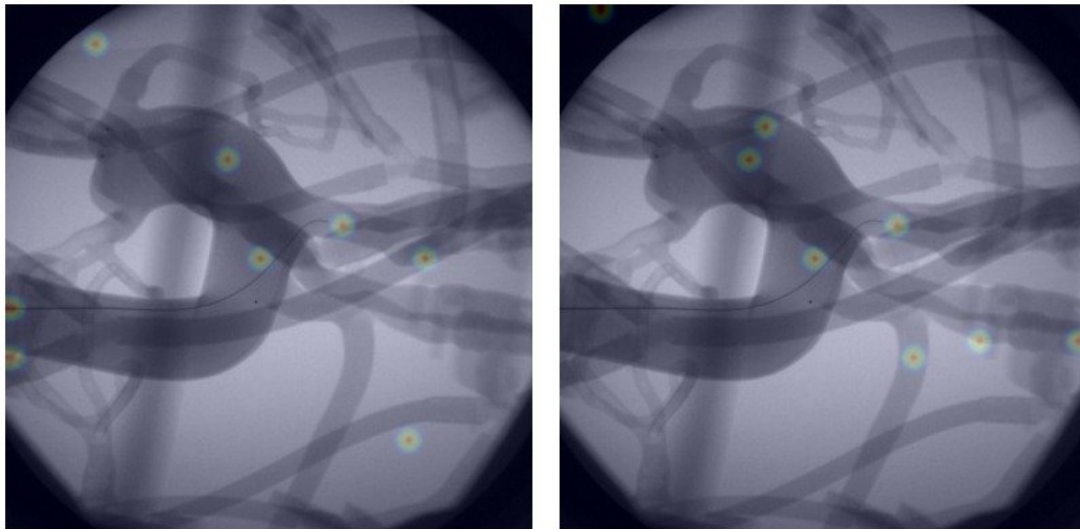


**Figure 6.8. Attention visualization:** Attention maps highlight regions where SplineFormer focuses its predictions, including the guidewire tip and key vascular landmarks. This localized attention improves interpretability and facilitates precise autonomous navigation.

### 6.4.5 Discussion

SplineFormer is presented as a new transformer network for predicting continuous guidewire geometries using a B-spline representation, enabling efficient encoding for real-time navigation. By parameterizing the guidewire with control points and knots, this approach ensures geometric consistency and provides a compact state representation for downstream robotic control. However, small variations in B-spline parameters can introduce spatial misalignment, affecting trajectory accuracy. In robotic experiments, SplineFormer successfully cannulated the [BCA](#) but failed in the [LCCA](#), consistent with prior findings [88], [123]. The [LCCA](#)'s sharper turns, narrower lumen, and abrupt bifurcation angle increase resistance and the risk of collision, challenging model generalization. These findings highlight the need for improved adaptability in high-curvature vascular structures.

### 6.4.6 Limitations

While SplineFormer provides a structured and interpretable representation for autonomous navigation, its reliance on B-spline parameterization makes it sensitive to perturbations, which can affect trajectory stability. Additionally, its failure in [LCCA](#) navigation reinforces the well-documented challenges of traversing high-curvature vascular regions [88]. The [LCCA](#)'s complex morphology makes navigation inherently more difficult than in the [BCA](#), limiting policy generalization. Addressing these challenges will require adaptive trajectory optimization, uncertainty-aware planning, and biomechanical modelling to improve robustness. Despite these constraints, SplineFormer demonstrates the viability of shape-driven navigation

strategies, motivating further research into learning-based autonomous interventions.

The contributions of SplineFormer represent a significant advancement in geometric modelling for endovascular navigation, offering a novel approach that complements the earlier components of this thesis. While CathSim provided the simulation environment, the Expert Navigation Network demonstrated multimodal learning capabilities, and Guide3D addressed data scarcity, SplineFormer introduces an innovative geometric representation that directly enhances navigation accuracy and interpretability. Together, these integrated contributions establish a comprehensive framework that addresses multiple facets of the autonomous endovascular navigation challenge, from simulation and data availability to perception and control.

## 6.5 Conclusions

SplineFormer is introduced as a spline-based framework for autonomous endovascular navigation that encodes guidewire geometry in a compact and structured latent representation. The method enhances trajectory planning and real-time decision-making, providing a foundation for precision-driven robotic control. While SplineFormer performs well in structured environments, addressing its limitations in high-curvature navigation is essential for real-world deployment. Future work will focus on adaptive learning strategies, biomechanical modelling, and preclinical validation to enhance generalization. By leveraging explainable curvilinear representations, SplineFormer shows the potential for fully autonomous endovascular interventions, contributing to safer and more efficient vascular navigation.

## Chapter 7

---

# Conclusions

This thesis presents a comprehensive framework to advance autonomy in endovascular navigation, addressing key technical, procedural, and data-centric challenges that hinder current robotic-assisted interventions. Through the development of the CathSim simulation environment, the [Expert Navigation Network \(ENN\)](#), the Guide3D dataset, and the SplineFormer model, this work introduces novel solutions that integrate high-fidelity simulation, multimodal sensory processing, and geometric learning to enable precise and adaptable catheter navigation. Together, these contributions lay a robust foundation for future autonomous surgical systems that are scalable, safe, and clinically relevant. The outlined future directions—including enhanced simulation realism, multimodal sensing, adaptive learning, and clinical validation—highlight a roadmap toward translating these innovations from controlled settings to real-world interventional medicine, promising to improve patient outcomes and broaden access to minimally invasive procedures.

## 7.1 Summary

This thesis provides a robust framework to advance autonomy in endovascular navigation, addressing key technical and procedural challenges associated with robotic-assisted interventions in complex vascular environments. By leveraging advancements in simulation-based [Reinforcement Learning \(RL\)](#) [20, 21], multimodal sensory integration [18], and geometric modelling [249], the proposed solutions overcome existing limitations in heuristic-based systems, enabling precise, adaptable, and scalable solutions for minimally invasive procedures.

The primary contributions are summarized as follows:

- 1. CathSim Simulation Framework:** A novel high-fidelity simulation environment was developed to address the bottleneck in reinforcement learning for autonomous catheter navigation. CathSim integrates anatomically accurate vascular models, precise catheter dynamics, and modular simulation tools optimized for RL algorithms. Leveraging MuJoCo's rigid body dynamics [250], CathSim ensures realistic frictional forces and collision interactions while maintaining computational efficiency. This framework enables high-throughput sampling and training in simulated environments that closely replicate clinical conditions.
- 2. Expert Navigation Network (ENN):** A multimodal learning framework, the [Expert Navigation Network \(ENN\)](#), was introduced to improve autonomous catheterization accuracy. ENN integrates diverse sensory modalities, including guidewire tip position, joint velocity, fluoroscopic imaging, and force feedback, through a [Soft Actor Critic \(SAC\)](#) policy [74]. The network's architecture is optimized for high-dimensional input processing, leveraging convolutional neural networks [Convolutional Neural Network \(CNN\)](#) for imaging data and [Multi-Layered Perceptrons \(MLPs\)](#) for kinematic and force data. ENN demonstrated superior navigation accuracy and robustness, reducing reliance on manual operator intervention [21].
- 3. Guide3D Dataset and Deep Learning Framework:** The Guide3D dataset was developed as the first high-resolution, open-source dataset for endovascular segmentation and 3D reconstruction. It incorporates over 8,700 annotated biplanar X-ray images with detailed calibration parameters for accurate 3D guidewire geometry estimation. In addition to the dataset, the chapter introduced a [Deep Learning \(DL\)](#) framework based on a [Gated Recurrent Unit \(GRU\)](#) architecture and a spherical coordinate representation, enabling accurate and efficient guidewire shape prediction. Together, these contributions address the scarcity of annotated datasets and robust methods for dynamic endovascular imaging, providing a benchmark for the development of RL and DL-based algorithms.
- 4. SplineFormer Model:** A transformer-based B-spline parameterization model, Spline-

Former, was introduced for real-time guidewire navigation. SplineFormer predicts guidewire shapes as continuous parametric splines, enabling dimensionally compact, interpretable representations of vascular trajectories. This approach eliminates the reliance on pixel-wise segmentation [205] and enhances robustness against imaging artefacts. Experimental validation demonstrated that SplineFormer achieves high prediction accuracy across diverse vascular configurations, even under noisy or partially occluded imaging conditions [48].

## 7.2 Future Work

While this thesis introduces substantial advancements, it also reveals critical paths for further research and development. Future work can be categorized into the following key areas:

- 1. Advanced Simulation-to-Reality Transfer (Sim2Real):** The realism of CathSim, while high, cannot fully replicate the complexities of real-world clinical environments, including patient-specific vascular anomalies, biological variability, and imaging artefacts. Future work should focus on minimizing domain discrepancies through techniques such as adversarial domain adaptation, physics-informed neural networks, and [Generative Adversarial Imitation Learning \(GAIL\)](#). Additionally, incorporating stochastic variability into CathSim's vascular models (e.g., dynamic wall compliance or blood flow dynamics) could enhance its utility for simulating real-world scenarios.
- 2. Expansion of Multimodal Sensing Frameworks:** The current implementation of ENN leverages fluoroscopy-based imaging and synthetic force feedback. Future work should expand these sensory modalities by integrating advanced imaging techniques such as [Intravascular Ultrasound \(IVUS\)](#), [Optical Coherence Tomography \(OCT\)](#), and electromagnetic field sensors. Such multimodal fusion would provide richer contextual information for autonomous systems, improving the robustness of catheter navigation in highly tortuous or occluded vessels.
- 3. Scalable Annotated Data Generation:** Although Guide3D addresses a critical gap in annotated datasets, its scope is limited by the labour-intensive nature of manual annotation and calibration. Future work should focus on developing scalable synthetic data generation pipelines using procedural modelling of vascular anatomy and automated annotation algorithms. Additionally, incorporating domain-specific data augmentation methods (e.g., vascular deformation, occlusions, or contrast variations) could improve algorithm generalization.
- 4. Adaptive Reinforcement Learning for Dynamic Environments:** The RL algorithms employed in this thesis rely on pre-defined simulation environments with fixed anatomical models. However, real-world scenarios involve dynamically changing conditions, such as blood flow variations, vessel deformation, or patient movement. Future research should explore meta-reinforcement learning and curriculum learning techniques to enable adaptive policies that generalize across unseen vascular anatomies and procedural conditions. Additionally, hierarchical RL could be employed to break down complex tasks, such as multi-target cannulation, into sub-goals, improving learning efficiency.
- 5. High-Fidelity Modelling of Tissue-Catheter Interactions:** Current simulation models assume simplified rigid body dynamics for catheter-vessel interactions. Future developments

should incorporate high-fidelity biomechanical models, including tissue elasticity, shear stress, and endothelial damage thresholds. Such enhancements would enable more realistic simulations of catheterization risks, such as vessel perforation or thrombosis, allowing for safer and more accurate training.

6. **Real-Time Control Optimization:** The computational demands of SplineFormer and ENN, while suitable for simulated environments, may pose challenges in real-time clinical applications. Future research should focus on optimizing these architectures through neural network pruning, quantization, and hardware acceleration (e.g., FPGA or TPU deployment). Moreover, incorporating Model Predictive Control (MPC) frameworks could enable real-time trajectory adjustments based on environmental feedback, improving navigation safety and precision.
7. **Expanding Applications to Other Interventional Domains:** The methodologies developed in this thesis have the potential to be extended beyond endovascular navigation. Applications in bronchoscopic navigation, neurosurgical interventions, and gastrointestinal endoscopy could leverage the same principles of RL, multimodal sensing, and geometric modelling. Future work could explore domain-specific modifications to adapt these frameworks for other minimally invasive procedures.
8. **Clinical Validation and Workflow Integration:** The ultimate goal of autonomous systems is safe and effective deployment in clinical settings. Future research should prioritize clinical validation through multicentre trials, focusing on metrics such as procedural success rates, time savings, and safety outcomes. Additionally, integrating these systems into existing surgical workflows requires user-friendly interfaces and intuitive controls that align with clinicians' expertise and preferences.

## 7.3 Final Reflections

This thesis represents a significant advancement in the field of autonomous endovascular navigation, combining state-of-the-art simulation, [Artificial Intelligence \(AI\)](#), and robotics to address key challenges in [Minimally Invasive Surgery \(MIS\)](#). By bridging gaps in simulation fidelity, multimodal data integration, and geometric modelling, this work lays the foundation for the next generation of autonomous surgical systems. Future developments, informed by the directions outlined above, hold the potential to revolutionize interventional medicine, reducing risks, enhancing precision, and expanding accessibility to life-saving procedures.

Beyond the immediate technical contributions, the broader significance of this research lies in its potential to transform endovascular robotics into a domain characterized by greater autonomy, reproducibility, and procedural efficiency. The structured and interpretable approaches developed here address a key clinical need: ensuring that autonomous systems remain transparent and auditable, which is critical for both physician trust and regulatory approval. Regulatory pathways, such as those governed by the FDA in the United States or the EMA in Europe, will require rigorous pre-clinical validation in phantoms and large-animal models, followed by clinical trials that demonstrate safety, reliability, and clinician override mechanisms. Integration into existing workflows must prioritize user-centric design, ensuring that automation enhances rather than disrupts established clinical practice.

Looking ahead, the rapid evolution of foundation models opens promising directions for advancing autonomy in surgical robotics. [Large Language Models \(LLMs\)](#) can provide procedural priors and context-aware policy guidance, while [Large Vision Models \(LVMs\)](#) can enhance perception under noisy and variable imaging conditions. Recent work on combining [LLMs](#) with fuzzy reinforcement learning for cooperative endovascular navigation [251] demonstrates how these models can contribute higher-level reasoning while maintaining safety constraints through adaptive uncertainty management. Integrating such models into future iterations of SplineFormer and related frameworks could enable systems that generalize more effectively across patient anatomies, dynamically adapt to intraoperative variability, and remain aligned with clinical safety requirements.

In summary, this thesis provides both a technical foundation and a translational perspective for autonomous endovascular navigation. By addressing regulatory considerations and pointing to the integration of [LLMs](#) and [LVMs](#) as part of future development, it charts a pathway toward clinically viable systems that combine intelligence, interpretability, and safety, key prerequisites for eventual adoption in real-world interventional medicine.

---

## References

- [1] Robinson, R. D., “Reliable machine learning for medical imaging data through automated quality control and data harmonization,” Jul. 2020 (cit. on p. 4).
- [2] Townsend, N., Wilson, L., Bhatnagar, P., Wickramasinghe, K., Rayner, M., and Nichols, M., “Cardiovascular disease in europe: Epidemiological update 2016,” *European heart journal*, vol. 37, no. 42, pp. 3232–3245, 2016 (cit. on pp. 15, 114).
- [3] Thukkani, A. K. and Kinlay, S., “Endovascular intervention for peripheral artery disease,” *Circulation research*, vol. 116, no. 9, pp. 1599–1613, 2015 (cit. on pp. 15, 114).
- [4] Goyal, M., Menon, B. K., Van Zwam, W. H., Dippel, D. W., Mitchell, P. J., Demchuk, A. M., Dávalos, A., Majoie, C. B., Der Lugt, A. van, De Miquel, M. A., *et al.*, “Endovascular thrombectomy after large-vessel ischaemic stroke: A meta-analysis of individual patient data from five randomised trials,” *The Lancet*, vol. 387, no. 10029, pp. 1723–1731, 2016 (cit. on pp. 15, 114).
- [5] Giacoppo, D., Colleran, R., Cassese, S., Frangieh, A. H., Wiebe, J., Joner, M., Schunkert, H., Kastrati, A., and Byrne, R. A., “Percutaneous coronary intervention vs coronary artery bypass grafting in patients with left main coronary artery stenosis: A systematic review and meta-analysis,” *JAMA Cardiology*, vol. 2, no. 10, pp. 1079–1088, 2017 (cit. on pp. 15, 114).
- [6] Brilakis, E., *Manual of percutaneous coronary interventions: a step-by-step approach*. Academic Press, 2020 (cit. on pp. 15, 114).
- [7] Klein, L. W., Miller, D. L., Balter, S., Laskey, W., Haines, D., Norbash, A., Mauro, M. A., and Goldstein, J. A., “Occupational health hazards in the interventional laboratory: Time for a safer environment,” *Radiology*, vol. 250, no. 2, pp. 538–544, 2009 (cit. on p. 15).
- [8] Rudnick, M. R., Goldfarb, S., Wexler, L., Ludbrook, P. A., Murphy, M. J., Halpern, E. F., Hill, J. A., Winniford, M., Cohen, M. B., VanFossen, D. B., *et al.*, “Nephrotoxicity of ionic and nonionic contrast media in 1196 patients: A randomized trial,” *Kidney international*, vol. 47, no. 1, pp. 254–261, 1995 (cit. on pp. 15, 114).
- [9] Hausegger, K. A., Schedlbauer, P., Deutschmann, H. A., and Tiesenhausen, K., “Complications in endoluminal repair of abdominal aortic aneurysms,” *European Journal of Radiology*, vol. 39, no. 1, pp. 22–33, 2001 (cit. on pp. 15, 114).
- [10] Saver, J. L., Goyal, M., Van der Lugt, A., Menon, B. K., Majoie, C. B., Dippel, D. W., Campbell, B. C., Nogueira, R. G., Demchuk, A. M., Tomasello, A., *et al.*, “Time to

- treatment with endovascular thrombectomy and outcomes from ischemic stroke: A meta-analysis,” *Jama*, vol. 316, no. 12, pp. 1279–1289, 2016 (cit. on pp. 15, 114).
- [11] Ho, P., Cheng, S. W., Wu, P., Ting, A. C., Poon, J. T., Cheng, C. K., Mok, J. H., and Tsang, M., “Ionizing radiation absorption of vascular surgeons during endovascular procedures,” *Journal of vascular surgery*, vol. 46, no. 3, pp. 455–459, 2007 (cit. on p. 15).
- [12] Madder, R. D., VanOosterhout, S., Mulder, A., Elmore, M., Campbell, J., Borgman, A., Parker, J., and Wohns, D., “Impact of robotics and a suspended lead suit on physician radiation exposure during percutaneous coronary intervention,” *Cardiovascular Revascularization Medicine*, vol. 18, no. 3, pp. 190–196, 2017 (cit. on p. 15).
- [13] Duran, C., Lumsden, A. B., and Bismuth, J., “A randomized, controlled animal trial demonstrating the feasibility and safety of the magellan™ endovascular robotic system,” *Annals of Vascular Surgery*, vol. 28, no. 2, pp. 470–478, 2014 (cit. on p. 15).
- [14] Nogueira, R. G., Sachdeva, R., Al-Bayati, A. R., Mohammaden, M. H., Frankel, M. R., and Haussen, D. C., “Robotic assisted carotid artery stenting for the treatment of symptomatic carotid disease: Technical feasibility and preliminary results,” *Journal of NeuroInterventional Surgery*, vol. 12, no. 4, pp. 341–344, 2020 (cit. on p. 15).
- [15] Monaco, M. G. L., Carta, A., Tamhid, T., and Porru, S., “Anti-x apron wearing and musculoskeletal problems among healthcare workers: A systematic scoping review,” *International Journal of Environmental Research and Public Health (IJERPH)*, vol. 17, no. 16, p. 5877, 2020 (cit. on p. 15).
- [16] Mofatteh, M., “Neurosurgery and artificial intelligence,” *AIMS neuroscience*, vol. 8, no. 4, p. 477, 2021 (cit. on pp. 15, 114).
- [17] Crinnion, W., Jackson, B., Sood, A., Lynch, J., Bergeles, C., Liu, H., Rhode, K., Pereira, V. M., and Booth, T. C., “Robotics in neurointerventional surgery: A systematic review of the literature,” *Journal of neurointerventional surgery*, vol. 14, no. 6, pp. 539–545, 2022 (cit. on pp. 15, 46, 114).
- [18] Sarker, I. H., “Machine learning: Algorithms, real-world applications and research directions,” *SN computer science*, vol. 2, no. 3, p. 160, 2021 (cit. on pp. 16, 133).
- [19] Fatima, M. and Pasha, M., “Survey of machine learning algorithms for disease diagnostic,” *Journal of Intelligent Learning Systems and Applications*, vol. 9, no. 01, pp. 1–16, 2017 (cit. on p. 16).
- [20] Sutton, R. S. and Barto, A. G., *Reinforcement learning: An introduction*. MIT press, 2018 (cit. on pp. 16, 35, 38, 133).
- [21] Arulkumaran, K., Deisenroth, M. P., Brundage, M., and Bharath, A. A., “Deep reinforcement learning: A brief survey,” *IEEE Signal Processing Magazine*, vol. 34, no. 6, pp. 26–38, 2017 (cit. on pp. 16, 45, 133).
- [22] Faure, F., Duriez, C., Delingette, H., Allard, J., Gilles, B., Marchesseau, S., Talbot, H., Courtecuisse, H., Bousquet, G., Peterlik, I., *et al.*, “Sofa: A multi-model framework

- for interactive physical simulation,” *Soft tissue biomechanical modeling for computer assisted surgery*, pp. 283–321, 2012 (cit. on p. 16).
- [23] Todorov, E., Erez, T., and Tassa, Y., “Mujoco: A physics engine for model-based control,” in *International Conference on Intelligent Robots and Systems (IROS)*, IEEE, 2012, pp. 5026–5033 (cit. on p. 20).
- [24] LeCun, Y., Bengio, Y., and Hinton, G., “Deep learning,” *Nature*, 2015 (cit. on pp. 27, 30).
- [25] Schmidhuber, J., “Deep learning in neural networks: An overview,” *Neural networks*, vol. 61, pp. 85–117, 2015 (cit. on p. 27).
- [26] Goodfellow, I., Bengio, Y., Courville, A., and Bengio, Y., *Deep learning*. MIT Press, 2016, vol. 1 (cit. on pp. 27, 30).
- [27] Rosenblatt, F., “The perceptron: A probabilistic model for information storage and organization in the brain,” *Psychological review*, vol. 65, no. 6, p. 386, 1958 (cit. on p. 28).
- [28] Minsky, M. L. and Papert, S. A., *Perceptrons: Expanded edition*, 1988 (cit. on p. 28).
- [29] Cybenko, G., “Approximation by superpositions of a sigmoidal function,” *Mathematics of control, signals and systems*, vol. 2, no. 4, pp. 303–314, 1989 (cit. on p. 28).
- [30] Hornik, K., “Approximation capabilities of multilayer feedforward networks,” *Neural networks*, vol. 4, no. 2, pp. 251–257, 1991 (cit. on p. 28).
- [31] LeCun, Y., Bottou, L., Bengio, Y., and Haffner, P., “Gradient-based learning applied to document recognition,” *Proceedings of the IEEE*, vol. 86, no. 11, pp. 2278–2324, 1998 (cit. on p. 30).
- [32] Krizhevsky, A., Sutskever, I., and Hinton, G. E., “Imagenet classification with deep convolutional neural networks,” *Advances in neural information processing systems*, vol. 25, 2012 (cit. on pp. 30, 31).
- [33] He, K., Zhang, X., Ren, S., and Sun, J., “Deep residual learning for image recognition,” in *Conference on Computer Vision and Pattern Recognition (CVPR)*, 2016 (cit. on pp. 30, 31).
- [34] Rawat, W. and Wang, Z., “Deep convolutional neural networks for image classification: A comprehensive review,” *Neural computation*, vol. 29, no. 9, pp. 2352–2449, 2017 (cit. on p. 30).
- [35] Dumoulin, V. and Visin, F., “A guide to convolution arithmetic for deep learning,” *arXiv preprint arXiv:1603.07285*, 2016 (cit. on p. 30).
- [36] Nair, V. and Hinton, G. E., “Rectified linear units improve restricted boltzmann machines,” in *Proceedings of the 27th international conference on machine learning (ICML-10)*, 2010, pp. 807–814 (cit. on p. 30).
- [37] Glorot, X., Bordes, A., and Bengio, Y., “Deep sparse rectifier neural networks,” in *Proceedings of the fourteenth international conference on artificial intelligence and statistics, JMLR Workshop and Conference Proceedings*, 2011, pp. 315–323 (cit. on p. 30).

- [38] Maas, A. L., Hannun, A. Y., Ng, A. Y., *et al.*, “Rectifier nonlinearities improve neural network acoustic models,” in *Proc. icml*, Atlanta, GA, vol. 30, 2013, p. 3 (cit. on p. 30).
- [39] Ramachandran, P., Zoph, B., and Le, Q. V., “Searching for activation functions,” *arXiv preprint arXiv:1710.05941*, 2017 (cit. on p. 30).
- [40] Boureau, Y.-L., Ponce, J., and LeCun, Y., “A theoretical analysis of feature pooling in visual recognition,” in *Proceedings of the 27th international conference on machine learning (ICML-10)*, 2010, pp. 111–118 (cit. on p. 30).
- [41] Scherer, D., Müller, A., and Behnke, S., “Evaluation of pooling operations in convolutional architectures for object recognition,” in *International conference on artificial neural networks*, Springer, 2010, pp. 92–101 (cit. on p. 30).
- [42] Zeiler, M. D. and Fergus, R., “Visualizing and understanding convolutional networks,” in *European Conference on Computer Vision (ECCV)*, Springer, 2014, pp. 818–833 (cit. on p. 31).
- [43] Huang, G., Liu, Z., Van Der Maaten, L., and Weinberger, K. Q., “Densely connected convolutional networks,” in *Proceedings of the IEEE conference on computer vision and pattern recognition*, 2017, pp. 4700–4708 (cit. on p. 31).
- [44] Tan, M. and Le, Q., “Efficientnet: Rethinking model scaling for convolutional neural networks,” in *International conference on machine learning*, PMLR, 2019, pp. 6105–6114 (cit. on p. 31).
- [45] Russakovsky, O., Deng, J., Su, H., Krause, J., Satheesh, S., Ma, S., Huang, Z., Karpathy, A., Khosla, A., Bernstein, M., *et al.*, “Imagenet large scale visual recognition challenge,” *International journal of computer vision*, vol. 115, pp. 211–252, 2015 (cit. on p. 31).
- [46] Graves, A., Mohamed, A.-r., and Hinton, G., “Speech recognition with deep recurrent neural networks,” in *2013 IEEE international conference on acoustics, speech and signal processing*, Ieee, 2013, pp. 6645–6649 (cit. on pp. 31, 33).
- [47] Bahdanau, D., “Neural machine translation by jointly learning to align and translate,” *arXiv preprint arXiv:1409.0473*, 2014 (cit. on p. 31).
- [48] Vaswani, A., “Attention is all you need,” *Advances in Neural Information Processing Systems*, 2017 (cit. on pp. 31, 34, 120, 121, 134).
- [49] Cho, K., “On the properties of neural machine translation: Encoder-decoder approaches,” *arXiv preprint arXiv:1409.1259*, 2014 (cit. on pp. 31, 33).
- [50] Elman, J. L., “Finding structure in time,” *Cognitive science*, vol. 14, no. 2, pp. 179–211, 1990 (cit. on p. 32).
- [51] Bengio, Y., Simard, P., and Frasconi, P., “Learning long-term dependencies with gradient descent is difficult,” *IEEE transactions on neural networks*, vol. 5, no. 2, pp. 157–166, 1994 (cit. on p. 32).
- [52] Devlin, J., “Bert: Pre-training of deep bidirectional transformers for language understanding,” *arXiv preprint arXiv:1810.04805*, 2018 (cit. on p. 35).

- [53] Radford, A., “Improving language understanding by generative pre-training,” 2018 (cit. on p. 35).
- [54] Dosovitskiy, A., Beyer, L., Kolesnikov, A., Weissenborn, D., Zhai, X., Unterthiner, T., Dehghani, M., Minderer, M., Heigold, G., Gelly, S., *et al.*, “An image is worth 16x16 words: Transformers for image recognition at scale,” *arXiv preprint arXiv:2010.11929*, 2020 (cit. on pp. 35, 103, 119).
- [55] Hatamizadeh, A., Tang, Y., Nath, V., Yang, D., Myronenko, A., Landman, B., Roth, H. R., and Xu, D., “Unetr: Transformers for 3d medical image segmentation,” in *Proceedings of the IEEE/CVF winter conference on applications of computer vision*, 2022, pp. 574–584 (cit. on p. 35).
- [56] Valanarasu, J. M. J., Oza, P., Hacihaliloglu, I., and Patel, V. M., “Medical transformer: Gated axial-attention for medical image segmentation,” in *International Conference on Medical Image Computing and Computer-Assisted Intervention (MICCAI)*, Springer, 2021, pp. 36–46 (cit. on p. 35).
- [57] Liu, Z., Lin, Y., Cao, Y., Hu, H., Wei, Y., Zhang, Z., Lin, S., and Guo, B., “Swin transformer: Hierarchical vision transformer using shifted windows,” in *Conference on Computer Vision and Pattern Recognition (CVPR)*, 2021, pp. 10 012–10 022 (cit. on p. 35).
- [58] Gao, Y., Zhou, M., and Metaxas, D. N., “Utnet: A hybrid transformer architecture for medical image segmentation,” in *International Conference on Medical Image Computing and Computer-Assisted Intervention (MICCAI)*, Springer, 2021, pp. 61–71 (cit. on p. 35).
- [59] Rumelhart, D. E., Hinton, G. E., and Williams, R. J., “Learning representations by back-propagating errors,” *nature*, vol. 323, no. 6088, pp. 533–536, 1986 (cit. on p. 35).
- [60] Kingma, D. P. and Ba, J., “Adam: A method for stochastic optimization,” *arXiv preprint arXiv:1412.6980*, 2014 (cit. on pp. 35, 89).
- [61] Tieleman, T. and Hinton, G., “Rmsprop: Divide the gradient by a running average of its recent magnitude. coursera: Neural networks for machine learning,” *COURSERA Neural Networks Mach. Learn*, vol. 17, 2012 (cit. on p. 35).
- [62] Kaelbling, L. P., Littman, M. L., and Moore, A. W., “Reinforcement learning: A survey,” *Journal of artificial intelligence research*, vol. 4, pp. 237–285, 1996 (cit. on pp. 35, 38).
- [63] Mnih, V., Kavukcuoglu, K., Silver, D., Rusu, A. A., Veness, J., Bellemare, M. G., Graves, A., Riedmiller, M., Fidjeland, A. K., Ostrovski, G., *et al.*, “Human-level control through deep reinforcement learning,” *nature*, vol. 518, no. 7540, pp. 529–533, 2015 (cit. on pp. 35, 38, 39, 82).
- [64] Puterman, M. L., *Markov decision processes: discrete stochastic dynamic programming*. John Wiley & Sons, 2014 (cit. on p. 36).
- [65] Kaelbling, L. P., Littman, M. L., and Cassandra, A. R., “Planning and acting in partially observable stochastic domains,” *Artificial intelligence*, vol. 101, no. 1-2, pp. 99–134, 1998 (cit. on p. 36).

- [66] Silver, D., Huang, A., Maddison, C. J., Guez, A., Sifre, L., Van Den Driessche, G., Schrittwieser, J., Antonoglou, I., Panneershelvam, V., Lanctot, M., *et al.*, “Mastering the game of go with deep neural networks and tree search,” *Nature*, vol. 529, no. 7587, pp. 484–489, 2016 (cit. on pp. 37, 38).
- [67] Lillicrap, T. P., Hunt, J. J., Pritzel, A., Heess, N., Erez, T., Tassa, Y., Silver, D., and Wierstra, D., “Continuous control with deep reinforcement learning,” *arXiv preprint arXiv:1509.02971*, 2015 (cit. on pp. 37, 38, 41, 55).
- [68] Schulman, J., Wolski, F., Dhariwal, P., Radford, A., and Klimov, O., “Proximal policy optimization algorithms,” *arXiv preprint arXiv:1707.06347*, 2017 (cit. on pp. 37, 40, 64).
- [69] Silver, D., Lever, G., Heess, N., Degris, T., Wierstra, D., and Riedmiller, M., “Deterministic policy gradient algorithms,” in *ICML*, Pmlr, 2014, pp. 387–395 (cit. on pp. 38, 41).
- [70] Bellman, R., “A markovian decision process,” *JMM*, pp. 679–684, 1957 (cit. on p. 39).
- [71] Watkins, C. J. and Dayan, P., “Q-learning,” *Machine learning*, vol. 8, pp. 279–292, 1992 (cit. on p. 39).
- [72] Sutton, R. S., McAllester, D., Singh, S., and Mansour, Y., “Policy gradient methods for reinforcement learning with function approximation,” *Conference on Neural Information Processing Systems (NeurIPS)*, vol. 12, 1999 (cit. on p. 40).
- [73] Williams, R. J., “Simple statistical gradient-following algorithms for connectionist reinforcement learning,” *Machine learning*, vol. 8, pp. 229–256, 1992 (cit. on p. 40).
- [74] Haarnoja, T., Zhou, A., Abbeel, P., and Levine, S., “Soft actor-critic: Off-policy maximum entropy deep reinforcement learning with a stochastic actor,” in *International Conference on Machine Learning*, 2018 (cit. on pp. 40, 41, 64, 81, 83, 133).
- [75] Kober, J., Bagnell, J. A., and Peters, J., “Reinforcement learning in robotics: A survey,” *The International Journal of Robotics Research*, vol. 32, no. 11, pp. 1238–1274, 2013 (cit. on p. 41).
- [76] Levine, S., Finn, C., Darrell, T., and Abbeel, P., “End-to-end training of deep visuomotor policies,” *Journal of Machine Learning Research (JMLR)*, vol. 17, no. 39, pp. 1–40, 2016 (cit. on p. 41).
- [77] Deisenroth, M. P., Neumann, G., Peters, J., *et al.*, “A survey on policy search for robotics,” *Foundations and Trends® in Robotics*, vol. 2, no. 1–2, pp. 1–142, 2013 (cit. on p. 41).
- [78] Recht, B., “A tour of reinforcement learning: The view from continuous control,” *Annual Review of Control, Robotics, and Autonomous Systems (ARCRAS)*, vol. 2, no. 1, pp. 253–279, 2019 (cit. on p. 41).
- [79] Chua, K., Calandra, R., McAllister, R., and Levine, S., “Deep reinforcement learning in a handful of trials using probabilistic dynamics models,” *Conference on Neural Information Processing Systems (NeurIPS)*, vol. 31, 2018 (cit. on p. 42).
- [80] Cheng, R., Orosz, G., Murray, R. M., and Burdick, J. W., “End-to-end safe reinforcement learning through barrier functions for safety-critical continuous control tasks,” in

- Association for the Advancement of Artificial Intelligence (AAAI)*, vol. 33, 2019, pp. 3387–3395 (cit. on p. 42).
- [81] Zhu, Y., Mottaghi, R., Kolve, E., Lim, J. J., Gupta, A., Fei-Fei, L., and Farhadi, A., “Target-driven visual navigation in indoor scenes using deep reinforcement learning,” in *International Conference on Robotics and Automation (ICRA)*, IEEE, 2017, pp. 3357–3364 (cit. on p. 42).
- [82] Nachum, O., Gu, S. S., Lee, H., and Levine, S., “Data-efficient hierarchical reinforcement learning,” *Conference on Neural Information Processing Systems (NeurIPS)*, vol. 31, 2018 (cit. on p. 42).
- [83] James, S., Wohlhart, P., Kalakrishnan, M., Kalashnikov, D., Irpan, A., Ibarz, J., Levine, S., Hadsell, R., and Bousmalis, K., “Sim-to-real via sim-to-sim: Data-efficient robotic grasping via randomized-to-canonical adaptation networks,” in *Conference on Computer Vision and Pattern Recognition (CVPR)*, 2019, pp. 12 627–12 637 (cit. on p. 43).
- [84] Haidegger, T., “Autonomy for surgical robots: Concepts and paradigms,” *IEEE Transactions on Medical Robotics and Bionics*, vol. 1, no. 2, pp. 65–76, Apr. 2019, ISSN: 2576-3202 (cit. on p. 44).
- [85] Robertshaw, H., Karstensen, L., Jackson, B., Sadati, H., Rhode, K., Ourselin, S., Grados, A., and Booth, T. C., “Artificial intelligence in the autonomous navigation of endovascular interventions: A systematic review,” *Frontiers in Human Neuroscience*, vol. 17, p. 1 239 374, Aug. 2023, ISSN: 1662-5161 (cit. on p. 45).
- [86] Behr, T., Pusch, T. P., Siegfarth, M., Hü sener, D., Mörschel, T., and Karstensen, L., “Deep Reinforcement Learning for the Navigation of Neurovascular Catheters,” *Current Directions in Biomedical Engineering*, vol. 5, no. 1, pp. 5–8, Sep. 2019, ISSN: 2364-5504 (cit. on pp. 45, 47, 55, 62, 79, 114, 117).
- [87] Schwein, A., Kramer, B., Chinnadurai, P., Walker, S., O’Malley, M., Lumsden, A., and Bismuth, J., “Flexible robotics with electromagnetic tracking improves safety and efficiency during in vitro endovascular navigation,” *Journal of vascular surgery*, vol. 65, no. 2, pp. 530–537, 2017 (cit. on pp. 45, 46).
- [88] Chi, W., Dagnino, G., Kwok, T. M., Nguyen, A., Kundrat, D., Abdelaziz, M. E., Riga, C., Bicknell, C., and Yang, G.-Z., “Collaborative robot-assisted endovascular catheterization with generative adversarial imitation learning,” in *International Conference on Robotics and Automation (ICRA)*, IEEE, 2020, pp. 2414–2420 (cit. on pp. 45, 46, 52, 67, 79, 115, 117, 125, 126, 129).
- [89] Cho, Y., Park, J.-H., Choi, J., and Chang, D. E., “Sim-to-real transfer of image-based autonomous guidewire navigation trained by deep deterministic policy gradient with behavior cloning for fast learning,” in *International Conference on Robotic Systems and Automation (IROS)*, IEEE, 2022, pp. 3468–3475 (cit. on pp. 45, 114, 117).
- [90] Karstensen, L., Ritter, J., Hatzl, J., P ätz, T., Langejürgen, J., Uhl, C., and Mathis-Ullrich, F., “Learning-based autonomous vascular guidewire navigation without human demon-

- stration in the venous system of a porcine liver,” *International Journal of Computer Assisted Radiology and Surgery (IJCARS)*, vol. 17, no. 11, pp. 2033–2040, 2022 (cit. on pp. 45, 114, 117).
- [91] Kweon, J., Kim, K., Lee, C., Kwon, H., Park, J., Song, K., Kim, Y. I., Park, J., Back, I., Roh, J.-H., *et al.*, “Deep reinforcement learning for guidewire navigation in coronary artery phantom,” *IEEE Access*, 2021 (cit. on pp. 45, 47, 55, 79, 114, 117).
- [92] Ionita, C. N., Mokin, M., Varble, N., Bednarek, D. R., Xiang, J., Snyder, K. V., Siddiqui, A. H., Levy, E. I., Meng, H., and Rudin, S., “Challenges and limitations of patient-specific vascular phantom fabrication using 3d polyjet printing,” in *Proceedings of SPIE—the International Society for Optical Engineering*, NIH Public Access, vol. 9038, 2014, p. 90380M (cit. on p. 46).
- [93] Nesbitt, C. I., Birdi, N., Mafeld, S., and Stansby, G., “The role of simulation in the development of endovascular surgical skills,” *Perspect Med Educ*, vol. 5, no. 1, pp. 8–14, Feb. 2016, ISSN: 2212-277X (cit. on pp. 46, 55).
- [94] Dequidt, J., Duriez, C., Cotin, S. p., and Kerrien, E., “Towards interactive planning of coil embolization in brain aneurysms,” in *International Conference on Medical Image Computing and Computer-Assisted Intervention (MICCAI)*, Springer Berlin/Heidelberg, vol. 5761, 2009, pp. 377–385 (cit. on pp. 46, 55).
- [95] Talbot, H., Spadoni, F., Duriez, C., Sermesant, M., Cotin, S., and Delingette, H., “Interactive training system for interventional electrocardiology procedures,” in *Biomedical Simulation: 6th International Symposium, ISBMS 2014, Strasbourg, France, October 16-17, 2014. Proceedings 6*, Springer, 2014, pp. 11–19 (cit. on pp. 46, 55).
- [96] Molinero, M. B., Dagnino, G., Liu, J., Chi, W., Abdelaziz, M. E., Kwok, T. M., Riga, C., and Yang, G.-Z., “Haptic guidance for robot-assisted endovascular procedures: Implementation and evaluation on surgical simulator,” in *International Conference on Robotic Systems and Automation (IROS)*, IEEE, 2019 (cit. on pp. 46, 52, 55, 57).
- [97] Wei, Y., Cotin, S., Dequidt, J., Duriez, C., Allard, J., Kerrien, E., *et al.*, “A (near) real-time simulation method of aneurysm coil embolization,” *Aneurysm*, vol. 8, no. 29, pp. 223–248, 2012 (cit. on pp. 46, 55, 62).
- [98] Yang, G.-Z., Cambias, J., Clearly, K., Daimler, E., Drake, J., Dupont, P. E., Hata, N., Kazanzides, P., Martel, S., Patel, R. V., *et al.*, *Medical robotics—regulatory, ethical, and legal considerations for increasing levels of autonomy*, 2017 (cit. on pp. 46, 55, 79).
- [99] Dijkstra, E. W., “A note on two problems in connection with graphs,” *Numerische mathematik*, vol. 1, no. 1, pp. 269–271, 1959 (cit. on pp. 47, 79).
- [100] Fischer, C., Boehler, Q., and Nelson, B. J., “Using magnetic fields to navigate and simultaneously localize catheters in endoluminal environments,” *Robotics and Automation Letters (RA-L)*, vol. 7, no. 3, pp. 7217–7223, 2022 (cit. on pp. 47, 79).
- [101] Ho, J. and Ermon, S., “Generative adversarial imitation learning,” *Advances in neural information processing systems*, vol. 29, 2016 (cit. on pp. 47, 79).

- [102] Rafii-Tari, H., Liu, J., Payne, C. J., Bicknell, C., and Yang, G.-Z., “Hierarchical hmm based learning of navigation primitives for cooperative robotic endovascular catheterization,” in *International Conference on Medical Image Computing and Computer-Assisted Intervention (MICCAI)*, Springer, 2014, pp. 496–503 (cit. on pp. 47, 79).
- [103] Chi, W., Liu, J., Abdelaziz, M. E., Dagnino, G., Riga, C., Bicknell, C., and Yang, G.-Z., “Trajectory optimization of robot-assisted endovascular catheterization with reinforcement learning,” in *International Conference on Robotic Systems and Automation (IROS)*, IEEE, 2018, pp. 3875–3881 (cit. on pp. 47, 79, 114).
- [104] Dupont, P. E., Nelson, B. J., Goldfarb, M., Hannaford, B., Menciassi, A., O’Malley, M. K., Simaan, N., Valdastrì, P., and Yang, G.-Z., “A decade retrospective of medical robotics research from 2010 to 2020,” *Science Robotics*, vol. 6, no. 60, eabi8017, 2021 (cit. on pp. 47, 79).
- [105] Ma, Y., King, A. P., Gogin, N., Rinaldi, C. A., Gill, J., Razavi, R., and Rhode, K. S., “Real-time respiratory motion correction for cardiac electrophysiology procedures using image-based coronary sinus catheter tracking,” in *International Conference on Medical Image Computing and Computer-Assisted Intervention (MICCAI)*, 2010 (cit. on pp. 47, 95, 101).
- [106] Wu, X., Housden, J., Varma, N., Ma, Y., Rueckert, D., and Rhode, K., “Catheter tracking in 3d echocardiographic sequences based on tracking in 2d x-ray sequences for cardiac catheterization interventions,” in *2013 IEEE 10th International Symposium on Biomedical Imaging*, IEEE, 2013, pp. 25–28 (cit. on p. 47).
- [107] Wu, X., Housden, J., Ma, Y., Rhode, K., and Rueckert, D., “A fast catheter segmentation and tracking from echocardiographic sequences based on corresponding x-ray fluoroscopic image segmentation and hierarchical graph modelling,” in *ISBI*, 2014 (cit. on pp. 48, 94, 95, 118).
- [108] Baur, C., Milletari, F., Belagiannis, V., Navab, N., and Fallavollita, P., “Automatic 3d reconstruction of electrophysiology catheters from two-view monoplane c-arm image sequences,” *International Journal of Computer Assisted Radiology and Surgery (IJCARS)*, 2016 (cit. on pp. 48, 93, 95, 101).
- [109] Milletari, F., Navab, N., and Fallavollita, P., “Automatic detection of multiple and overlapping ep catheters in fluoroscopic sequences,” in *International Conference on Medical Image Computing and Computer-Assisted Intervention (MICCAI)*, Berlin, Germany: Springer, 2013, pp. 371–379, ISBN: 978-3-642-40760-4 (cit. on pp. 48, 49).
- [110] Pauly, O., Heibel, H., and Navab, N., “A machine learning approach for deformable guide-wire tracking in fluoroscopic sequences,” in *International Conference on Medical Image Computing and Computer-Assisted Intervention (MICCAI)*, 2010 (cit. on pp. 48, 116).
- [111] Baur, C., Albarqouni, S., Demirci, S., Navab, N., and Fallavollita, P., “Cathnets: Detection and single-view depth prediction of catheter electrodes,” in *Medical Imaging and*

- Augmented Reality*, Cham, Switzerland: Springer, Aug. 2016, pp. 38–49, ISBN: 978-3-319-43775-0 (cit. on p. 48).
- [112] Burgner, J., Herrell, S. D., and Webster III, R. J., “Toward fluoroscopic shape reconstruction for control of steerable medical devices,” in *Dynamic Systems and Control Conference*, vol. 54761, 2011, pp. 791–794 (cit. on pp. 49, 93, 96, 102).
- [113] Wagner, M., Schafer, S., Strother, C., and Mistretta, C., “4d interventional device reconstruction from biplane fluoroscopy,” *Medical physics*, vol. 43, no. 3, pp. 1324–1334, 2016 (cit. on pp. 50, 93, 95, 96).
- [114] Hoffmann, M., Brost, A., Koch, M., Bourier, F., Maier, A., Kurzidim, K., Strobel, N., and Hornegger, J., “Electrophysiology catheter detection and reconstruction from two views in fluoroscopic images,” *Transactions on Medical Imaging*, vol. 35, no. 2, pp. 567–579, 2015 (cit. on pp. 50, 93, 95, 96).
- [115] Hoffmann, M., Brost, A., Jakob, C., Bourier, F., Koch, M., Kurzidim, K., Hornegger, J., and Strobel, N., “Semi-automatic catheter reconstruction from two views,” in *International Conference on Medical Image Computing and Computer-Assisted Intervention (MICCAI)*, Springer, 2012, pp. 584–591 (cit. on pp. 50, 95, 96).
- [116] Hoffmann, M., Brost, A., Jakob, C., Koch, M., Bourier, F., Kurzidim, K., Hornegger, J., and Strobel, N., “Reconstruction method for curvilinear structures from two views,” in *Medical Imaging 2013: Image-Guided Procedures, Robotic Interventions, and Modeling*, Spie, vol. 8671, 2013, pp. 630–637 (cit. on pp. 50, 93, 96).
- [117] Lobaton, E. J., Fu, J., Torres, L. G., and Alterovitz, R., “Continuous shape estimation of continuum robots using x-ray images,” in *2013 IEEE international conference on robotics and automation*, Ieee, 2013, pp. 725–732 (cit. on pp. 50, 96).
- [118] Vandini, A., Giannarou, S., Lee, S.-L., and Yang, G.-Z., “3d robotic catheter shape reconstruction and localisation using appearance priors and adaptive c-arm positioning,” in *International Workshop on Medical Imaging and Virtual Reality*, Springer, 2013, pp. 172–181 (cit. on pp. 50, 96).
- [119] Vandini, A., Bergeles, C., Lin, F.-Y., and Yang, G.-Z., “Vision-based intraoperative shape sensing of concentric tube robots,” in *International Conference on Robotic Systems and Automation (IROS)*, Ieee, 2015, pp. 2603–2610 (cit. on pp. 50, 96).
- [120] Otake, Y., Murphy, R. J., Kutzer, M., Taylor, R. H., and Armand, M., “Piecewise-rigid 2d-3d registration for pose estimation of snake-like manipulator using an intraoperative x-ray projection,” in *Medical Imaging 2014: Image-Guided Procedures, Robotic Interventions, and Modeling*, Spie, 2014, pp. 185–190 (cit. on pp. 50, 96).
- [121] Papalazarou, C., Rongen, P. M., *et al.*, “3d catheter reconstruction using non-rigid structure-from-motion and robotics modeling,” in *Medical Imaging 2012: Image-Guided Procedures, Robotic Interventions, and Modeling*, Spie, vol. 8316, 2012, pp. 622–629 (cit. on pp. 50, 96).

- [122] Ramadani, A., Bui, M., Wendler, T., Schunkert, H., Ewert, P., and Navab, N., “A survey of catheter tracking concepts and methodologies,” *Med Image Anal*, 2022 (cit. on pp. 50, 93, 101).
- [123] **Jianu, T.**, Huang, B., Vu, M. N., Abdelaziz, M. E., Fichera, S., Lee, C.-Y., Berthet-Rayne, P., Baena, F. R. y, and Nguyen, A., “Cathsim: An open-source simulator for endovascular intervention,” *IEEE Transactions on Medical Robotics and Bionics*, 2024, Code available at: <https://airvlab.github.io/cathsim> (cit. on pp. 51, 80, 107, 129).
- [124] Wamala, I., Roche, E. T., and Pigula, F. A., “The use of soft robotics in cardiovascular therapy,” *Expert Review of Cardiovascular Therapy*, vol. 15, no. 10, pp. 767–774, 2017 (cit. on pp. 52, 78).
- [125] Omisore, O. M., Han, S., Xiong, J., Li, H., Li, Z., and Wang, L., “A review on flexible robotic systems for minimally invasive surgery,” *IEEE Transactions on Systems, Man, and Cybernetics: Systems*, 2020 (cit. on pp. 52, 79).
- [126] Kundrat, D., Dagnino, G., Kwok, T. M., Abdelaziz, M. E., Chi, W., Nguyen, A., Riga, C., and Yang, G.-Z., “An mr-safe endovascular robotic platform: Design, control, and ex-vivo evaluation,” *IEEE Transactions on Biomedical Engineering*, vol. 68, no. 10, pp. 3110–3121, 2021 (cit. on pp. 52, 57, 58, 67, 78, 87, 88).
- [127] Pereira, V. M., Cancelliere, N. M., Nicholson, P., Radovanovic, I., Drake, K. E., Sungur, J.-M., Krings, T., and Turk, A., “First-in-human, robotic-assisted neuroendovascular intervention,” *Journal of neurointerventional surgery*, vol. 12, no. 4, pp. 338–340, 2020 (cit. on p. 52).
- [128] Burgner-Kahrs, J., Rucker, D. C., and Choset, H., “Continuum robots for medical applications: A survey,” *IEEE Transactions on Robotics*, vol. 31, no. 6, pp. 1261–1280, 2015 (cit. on p. 52).
- [129] Heidt, T., Reiss, S., Krafft, A. J., Özen, A. C., Lottner, T., Hehrlein, C., Galmbacher, R., Kayser, G., Hilgendorf, I., Stachon, P., *et al.*, “Real-time magnetic resonance imaging-guided coronary intervention in a porcine model,” *Scientific reports*, vol. 9, no. 1, pp. 1–10, 2019 (cit. on p. 52).
- [130] Abdelaziz, M. E. M. K., Kundrat, D., Pupillo, M., Dagnino, G., *et al.*, “Toward a versatile robotic platform for fluoroscopy and mri-guided endovascular interventions: A pre-clinical study,” in *IEEE/RSJ International Conference on Intelligent Robots and Systems*, 2019 (cit. on pp. 52, 57, 115).
- [131] Konstantinova, J., Jiang, A., Althoefer, K., Dasgupta, P., and Nanayakkara, T., “Implementation of tactile sensing for palpation in robot-assisted minimally invasive surgery: A review,” *IEEE Sensors Journal*, vol. 14, no. 8, pp. 2490–2501, 2014 (cit. on p. 52).
- [132] Nguyen, A., Kundrat, D., Dagnino, G., Chi, W., Abdelaziz, M. E., Guo, Y., Ma, Y., Kwok, T. M., Riga, C., and Yang, G.-Z., “End-to-end real-time catheter segmentation with optical flow-guided warping during endovascular intervention,” in *International*

- Conference on Robotics and Automantion (ICRA)*, IEEE, 2020, pp. 9967–9973 (cit. on pp. 52, 57, 94, 95, 101).
- [133] Attanasio, A., Scaglioni, B., De Momi, E., Fiorini, P., and Valdastri, P., “Autonomy in surgical robotics,” *Annual Review of Control, Robotics, and Autonomous Systems*, vol. 4, pp. 651–679, 2021 (cit. on p. 52).
- [134] Simaan, N., Yasin, R. M., and Wang, L., “Medical technologies and challenges of robot-assisted minimally invasive intervention and diagnostics,” *Annual Review of Control, Robotics, and Autonomous Systems*, vol. 1, pp. 465–490, 2018 (cit. on p. 52).
- [135] Towers, M., Kwiatkowski, A., Terry, J., Balis, J. U., De Cola, G., Deleu, T., Goulão, M., Kallinteris, A., Krimmel, M., KG, A., *et al.*, “Gymnasium: A standard interface for reinforcement learning environments,” *arXiv preprint arXiv:2407.17032*, 2024 (cit. on p. 53).
- [136] Todorov, E., Erez, T., and Tassa, Y., “Mujoco: A physics engine for model-based control,” in *International Conference on Robotic Systems and Automation (IROS)*, 2012 (cit. on pp. 53, 55, 56, 58–60).
- [137] Juliani, A., Berges, V.-P., Teng, E., Cohen, A., Harper, J., Elion, C., Goy, C., Gao, Y., Henry, H., Mattar, M., *et al.*, “Unity: A general platform for intelligent agents,” *arXiv preprint arXiv:1809.02627*, 2018 (cit. on p. 55).
- [138] Karstensen, L., Behr, T., Pusch, T. P., Mathis-Ullrich, F., and Stallkamp, J., “Autonomous guidewire navigation in a two dimensional vascular phantom,” *Current Directions in Biomedical Engineering*, vol. 6, no. 1, 2020 (cit. on pp. 55, 62, 79).
- [139] Faure, F., Duriez, C., Delingette, H., Allard, J., Gilles, B., Marchesseau, S., Talbot, H., Courtecuisse, H., Bousquet, G., Peterlik, I., and Cotin, S., “Sofa: A multi-model framework for interactive physical simulation,” in *Soft Tissue Biomechanical Modeling for Computer Assisted Surgery*, 2012 (cit. on p. 55).
- [140] Omisore, O. M., Akinyemi, T., Duan, W., Du, W., and Wang, L., “A novel sample-efficient deep reinforcement learning with episodic policy transfer for pid-based control in cardiac catheterization robots,” *arXiv preprint arXiv:2110.14941*, 2021 (cit. on pp. 55, 79).
- [141] Rohmer, E., Singh, S. P., and Freese, M., “V-rep: A versatile and scalable robot simulation framework,” in *International Conference on Robotic Systems and Automation (IROS)*, 2013 (cit. on p. 55).
- [142] Schegg, P., Dequidt, J., Coevoet, E., Leurent, E., Sabatier, R., Preux, P., and Duriez, C., “Automated planning for robotic guidewire navigation in the coronary arteries,” in *2022 IEEE 5th International Conference on Soft Robotics (RoboSoft)*, IEEE, 2022, pp. 239–246 (cit. on pp. 55, 79).
- [143] Davis, R., Henshell, R., and Warburton, G., “A timoshenko beam element,” *Journal of Sound and Vibration*, 1972 (cit. on p. 55).

- [144] Sinceri, S., Carbone, M., Marconi, M., Moglia, A., Ferrari, M., and Ferrari, V., “Basic endovascular skills trainer: A surgical simulator for the training of novice practitioners of endovascular procedures,” in *2015 37th Annual International Conference of the IEEE Engineering in Medicine and Biology Society (EMBC)*, 2015 (cit. on p. 55).
- [145] Cho, Y., Park, J.-H., Choi, J., and Chang, D. E., “Image processing based autonomous guidewire navigation in percutaneous coronary intervention,” in *International Conference on Consumer Electronics-Asia (ICCE-Asia)*, IEEE, 2021, pp. 1–6 (cit. on pp. 55, 79, 81).
- [146] Schegg, P., Ménager, E., Khairallah, E., Marchal, D., Dequidt, J., Preux, P., and Duriez, C., “Sofagym: An open platform for reinforcement learning based on soft robot simulations,” *Soft Robotics*, vol. 10, no. 2, pp. 410–430, Apr. 2023, ISSN: 2169-5172 (cit. on p. 56).
- [147] Scheickl, P. M., Gyenes, B. z., Younis, R., Haas, C., Neumann, G., Wagner, M., and Mathis-Ullrich, F., “Lapgyim – an open source framework for reinforcement learning in robot-assisted laparoscopic surgery,” *ArXiv e-prints*, Feb. 2023. eprint: [2302.09606](https://arxiv.org/abs/2302.09606) (cit. on p. 56).
- [148] Towers, M., Terry, J. K., Kwiatkowski, A., Balis, J. U., Cola, G. d., Deleu, T., Goulão, M., Kallinteris, A., KG, A., Krimmel, M., Perez-Vicente, R., Pierré, A., Schulhoff, S., Tai, J. J., Shen, A. T. J., and Younis, O. G., *Gymnasium*, Mar. 2023 (cit. on p. 56).
- [149] Gailloud, P., Pray, J., Muster, M., Piotin, M., Fasel, J., and Rüfenacht, D., “An in vitro anatomic model of the human cerebral arteries with saccular arterial aneurysms,” *Surgical and Radiologic Anatomy*, 1997 (cit. on p. 58).
- [150] Martin, J.-B., Sayegh, Y., Gailloud, P., Sugiou, K., Khan, H. G., Fasel, J. H., and Rüfenacht, D. A., *In-vitro models of human carotid atheromatous disease*. International Course Book of Peripheral Vascular Intervention, 1998 (cit. on pp. 58, 97, 125).
- [151] Gailloud, P., Muster, M., Piotin, M., Mottu, F., Murphy, K. J., Fasel, J. H., and Rüfenacht, D. A., “In vitro models of intracranial arteriovenous fistulas for the evaluation of new endovascular treatment materials,” *American Journal of Neuroradiology (AJNR)*, 1999 (cit. on pp. 58, 97, 125).
- [152] Silcowitz, M., Niebe, S., and Erleben, K., “Interactive rigid body dynamics using a projected gauss–seidel subspace minimization method,” in *International Conference on Computer Vision, Imaging and Computer Graphics*, Springer, 2010, pp. 218–229 (cit. on p. 58).
- [153] Mamou, K. and Ghorbel, F., “A simple and efficient approach for 3d mesh approximate convex decomposition,” in *2009 16th IEEE international conference on image processing (ICIP)*, 2009 (cit. on p. 58).
- [154] Jastrzebski, Z. D., “Nature and properties of engineering materials,” 1976 (cit. on p. 60).
- [155] Featherstone, R., *Rigid body dynamics algorithms*. Springer, 2014 (cit. on p. 61).

- [156] Todorov, E., “A convex, smooth and invertible contact model for trajectory optimization,” in *International Conference on Robotics and Automantion (ICRA)*, IEEE, 2011, pp. 1071–1076 (cit. on p. 61).
- [157] Dreyfus, R., Boehler, Q., and Nelson, B. J., “A simulation framework for magnetic continuum robots,” *RAL*, vol. 7, no. 3, pp. 8370–8376, 2022 (cit. on p. 61).
- [158] Yi, X., Adams, S., Babyn, P., and Elnajmi, A., “Automatic catheter detection in pediatric x-ray images using a scale-recurrent network and synthetic data,” *arXiv:1806.00921*, 2018 (cit. on p. 62).
- [159] Dalal, G., Dvijotham, K., Vecerik, M., Hester, T., Paduraru, C., and Tassa, Y., “Safe exploration in continuous action spaces,” *arXiv preprint arXiv:1801.08757*, 2018 (cit. on p. 64).
- [160] Mnih, V., Kavukcuoglu, K., Silver, D., Graves, A., Antonoglou, I., Wierstra, D., and Riedmiller, M., *Playing atari with deep reinforcement learning*, 2013. arXiv: [1312.5602](https://arxiv.org/abs/1312.5602) [cs.LG] (cit. on p. 64).
- [161] Hart, P. E., Nilsson, N. J., and Raphael, B., “A formal basis for the heuristic determination of minimum cost paths,” *IEEE Transactions on Systems Science and Cybernetics*, vol. 4, no. 2, pp. 100–107, 1968 (cit. on p. 65).
- [162] Raffin, A., Hill, A., Gleave, A., Kanervisto, A., Ernestus, M., and Dormann, N., “Stable-baselines3: Reliable reinforcement learning implementations,” *Journal of Machine Learning Research*, vol. 22, no. 268, pp. 1–8, 2021 (cit. on pp. 66, 81).
- [163] Rafii-Tari, H., Payne, C. J., Bicknell, C., Kwok, K.-W., Cheshire, N. J. W., Riga, C., and Yang, G.-Z., “Objective assessment of endovascular navigation skills with force sensing,” *Annals of Biomedical Engineering*, vol. 45, no. 5, pp. 1315–1327, May 2017, ISSN: 1573-9686 (cit. on p. 67).
- [164] Likert, R., “A technique for the measurement of attitudes,” *Archives of psychology*, 1932 (cit. on p. 68).
- [165] Li, P., Feng, J., Zhang, X., Fang, D., Zhang, J., and Liang, C., “Modeling and experimental study of the intervention forces between the guidewire and blood vessels,” *Medical Engineering & Physics*, vol. 127, p. 104 166, 2024 (cit. on p. 70).
- [166] **Jianu, T.**, Huang, B., Vo, T., Vu, M. N., Kang, J., Nguyen, H., Omisore, O., Berthet-Rayne, P., Fichera, S., and Nguyen, A., “Autonomous catheterization with open-source simulator and expert trajectory,” in *Handbook of Robotic and Image-Guided Surgery, 2nd Edition*, Nasab, M. H. A., Ed., 2nd ed., Elsevier, 2025, ISBN: 9780443139123 (cit. on p. 77).
- [167] Padsalgikar, A., “Cardiovascular system: Structure, assessment, and diseases,” *Plastics in medical devices for cardiovascular applications. William Andrew Publishing*, pp. 103–132, 2017 (cit. on p. 78).
- [168] Omisore, O. M., Han, S., Ren, L., Wang, G., Ou, F., Li, H., and Wang, L., “Towards characterization and adaptive compensation of backlash in a novel robotic catheter

- system for cardiovascular interventions,” *IEEE Transactions on Biomedical Circuits and Systems*, vol. 12, no. 4, pp. 824–838, 2018 (cit. on p. 78).
- [169] Mahmud, E., Schmid, F., Kalmar, P., Deutschmann, H., Hafner, F., Rief, P., and Brodmann, M., “Feasibility and safety of robotic peripheral vascular interventions: Results of the rapid trial,” *Cardiovascular Interventions*, vol. 9, no. 19, pp. 2058–2064, 2016 (cit. on p. 78).
- [170] Püschel, A., Schafmayer, C., and Groß, J., “Robot-assisted techniques in vascular and endovascular surgery,” *Langenbeck’s Archives of Surgery*, vol. 407, no. 5, pp. 1789–1795, 2022 (cit. on pp. 78, 80, 93).
- [171] Jara, R. D., Guerrón, A. D., and Portenier, D., “Complications of robotic surgery,” *Surgical Clinics*, vol. 100, no. 2, pp. 461–468, 2020 (cit. on p. 78).
- [172] Kiran, B. R., Sobh, I., Talpaert, V., Mannion, P., Al Sallab, A. A., Yogamani, S., and Pérez, P., “Deep reinforcement learning for autonomous driving: A survey,” *IEEE Transactions on Intelligent Transportation Systems*, vol. 23, no. 6, pp. 4909–4926, 2021 (cit. on pp. 78, 80).
- [173] Li, B., Wei, R., Xu, J., Lu, B., Yee, C. H., Ng, C. F., Heng, P.-A., Dou, Q., and Liu, Y.-H., “3d perception based imitation learning under limited demonstration for laparoscope control in robotic surgery,” in *International Conference on Robotics and Automation (ICRA)*, IEEE, 2022, pp. 7664–7670 (cit. on p. 78).
- [174] You, H., Bae, E., Moon, Y., Kweon, J., and Choi, J., “Automatic control of cardiac ablation catheter with deep reinforcement learning method,” *Journal of Mechanical Science and Technology*, vol. 33, pp. 5415–5423, 2019 (cit. on pp. 79, 117).
- [175] Athiniotis, S., Srivatsan, R., and Choset, H., “Deep q reinforcement learning for autonomous navigation of surgical snake robot in confined spaces,” in *Proceedings of the The Hamlyn Symposium on Medical Robotics, London, UK*, 2019, pp. 23–26 (cit. on p. 79).
- [176] Ji, C., Hou, Z.-G., and Xie, X.-L., “An image-based guidewire navigation method for robot-assisted intravascular interventions,” in *2011 Annual International Conference of the IEEE Engineering in Medicine and Biology Society*, IEEE, 2011, pp. 6680–6685 (cit. on p. 79).
- [177] Qian, H., Lin, X., Wu, Z., Zeng, Q., Li, C., Pang, Y., Wang, C., and Zhou, S., “Towards rebuild the interventionist’s intra-operative natural behavior: A fully sensorized endovascular robotic system design,” in *2019 International Conference on Medical Imaging Physics and Engineering (ICMIPE)*, IEEE, 2019, pp. 1–7 (cit. on p. 79).
- [178] Tai, L., Zhang, J., Liu, M., and Burgard, W., “Socially compliant navigation through raw depth inputs with generative adversarial imitation learning,” in *International Conference on Robotics and Automation (ICRA)*, IEEE, 2018, pp. 1111–1117 (cit. on p. 79).

- [179] Finn, C., Levine, S., and Abbeel, P., “Guided cost learning: Deep inverse optimal control via policy optimization,” in *International Conference on Machine Learning*, PMLR, 2016, pp. 49–58 (cit. on p. 79).
- [180] Rafii-Tari, H., Liu, J., Lee, S.-L., Bicknell, C., and Yang, G.-Z., “Learning-based modeling of endovascular navigation for collaborative robotic catheterization,” in *International Conference on Medical Image Computing and Computer-Assisted Intervention (MICCAI)*, Springer, 2013, pp. 369–377 (cit. on p. 79).
- [181] Chi, W., Liu, J., Rafii-Tari, H., Riga, C., Bicknell, C., and Yang, G.-Z., “Learning-based endovascular navigation through the use of non-rigid registration for collaborative robotic catheterization,” *International Journal of Computer Assisted Radiology and Surgery (IJCARs)*, vol. 13, Apr. 2018 (cit. on p. 79).
- [182] Saveriano, M., Abu-Dakka, F. J., Kramberger, A., and Peternel, L., “Dynamic movement primitives in robotics: A tutorial survey,” *arXiv preprint arXiv:2102.03861*, 2021 (cit. on p. 79).
- [183] Kim, J. W., Zhang, P., Gehlbach, P., Iordachita, I., and Kobilarov, M., “Towards autonomous eye surgery by combining deep imitation learning with optimal control,” in *Conference on Robot Learning*, PMLR, 2021, pp. 2347–2358 (cit. on p. 80).
- [184] Zhao, W., Queraltá, J. P., and Westerlund, T., “Sim-to-real transfer in deep reinforcement learning for robotics: A survey,” in *2020 IEEE symposium series on computational intelligence (SSCI)*, IEEE, 2020, pp. 737–744 (cit. on p. 80).
- [185] Okamura, A. M., “Haptic feedback in robot-assisted minimally invasive surgery,” *Current opinion in urology*, vol. 19, no. 1, p. 102, 2009 (cit. on p. 80).
- [186] Shi, C., Luo, X., Qi, P., Li, T., Song, S., Najdovski, Z., Fukuda, T., and Ren, H., “Shape sensing techniques for continuum robots in minimally invasive surgery: A survey,” *IEEE Transactions on Biomedical Engineering*, vol. 64, no. 8, pp. 1665–1678, 2016 (cit. on p. 80).
- [187] Tassa, Y., Doron, Y., Muldal, A., Erez, T., Li, Y., Las Casas, D. de, Budden, D., Abdolmaleki, A., Merel, J., Lefrancq, A., Lillicrap, T., and Riedmiller, M., *Deepmind control suite*, 2018. arXiv: 1801.00690 [cs.AI] (cit. on p. 81).
- [188] Rafii-Tari, H., Payne, C. J., Riga, C., Bicknell, C., Lee, S.-L., and Yang, G.-Z., “Assessment of navigation cues with proximal force sensing during endovascular catheterization,” in *International Conference on Medical Image Computing and Computer-Assisted Intervention (MICCAI)*, Springer, 2012, pp. 560–567 (cit. on p. 81).
- [189] Song, H.-S., Yi, B.-J., Won, J. Y., and Woo, J., “Learning-based catheter and guidewire-driven autonomous vascular intervention robotic system for reduced repulsive force,” *Journal of Computational Design and Engineering*, vol. 9, no. 5, pp. 1549–1564, 2022 (cit. on pp. 81, 84).
- [190] Agarap, A. F., *Deep learning using rectified linear units (relu)*, 2019. arXiv: 1803.08375 [cs.NE] (cit. on pp. 82, 105).

- [191] Hussein, A., Gaber, M. M., Elyan, E., and Jayne, C., “Imitation learning: A survey of learning methods,” *ACM Computing Surveys (CSUR)*, vol. 50, no. 2, pp. 1–35, 2017 (cit. on p. 83).
- [192] Hou, Y., Ma, Z., Liu, C., and Loy, C. C., “Learning to steer by mimicking features from heterogeneous auxiliary networks,” in *Association for the Advancement of Artificial Intelligence (AAAI)*, vol. 33, 2019, pp. 8433–8440 (cit. on p. 84).
- [193] Yokoyama, K., Nakagawa, H., Shah, D. C., Lambert, H., Leo, G., Aeby, N., Ikeda, A., Pitha, J. V., Sharma, T., Lazzara, R., *et al.*, “Novel contact force sensor incorporated in irrigated radiofrequency ablation catheter predicts lesion size and incidence of steam pop and thrombus,” *Circulation: Arrhythmia and Electrophysiology*, vol. 1, no. 5, pp. 354–362, 2008 (cit. on p. 84).
- [194] Anderson, P., Chang, A., Chaplot, D. S., Dosovitskiy, A., Gupta, S., Koltun, V., Kosecka, J., Malik, J., Mottaghi, R., Savva, M., *et al.*, “On evaluation of embodied navigation agents,” *arXiv preprint arXiv:1807.06757*, 2018 (cit. on p. 88).
- [195] Dosovitskiy, A., Ros, G., Codevilla, F., Lopez, A., and Koltun, V., “Carla: An open urban driving simulator,” in *Proceedings of the 1st Annual Conference on Robot Learning*, 2017, pp. 1–16 (cit. on p. 91).
- [196] **Jianu, T.**, Huang, B., Nguyen, H., Bhattarai, B., Do, T., Tjiputra, E., Tran, Q., Berthet-Rayne, P., Le, N., Fichera, S., and Nguyen, A., “Guide3d: A bi-planar x-ray dataset for guidewire segmentation and 3d reconstruction,” in *Proceedings of the Asian Conference on Computer Vision (ACCV)*, Code available at: <https://airvlab.github.io/guide3d/>, Dec. 2024, pp. 1549–1565 (cit. on p. 92).
- [197] **Jianu, T.**, Huang, B., Nguyen, H., Berthet-Rayne, P., Fichera, S., and Nguyen, A., “Deepwire: Spherical coordinate-based deep learning for accurate guidewire shape reconstruction,” in *Proceedings of the 9th International Conference on Biomedical Signal and Image Processing (ICBIP 2024)*, Suzhou, China, 2024 (cit. on p. 92).
- [198] **Jianu, T.**, Huang, B., Berthet-Rayne, P., Fichera, S., and Nguyen, A., “3d guidewire shape reconstruction from monoplane fluoroscopic images,” in *International Conference on Robot Intelligence Technology and Applications*, Springer, 2023, pp. 84–94 (cit. on p. 92).
- [199] Rafii-Tari, H., Payne, C. J., and Yang, G.-Z., “Current and emerging robot-assisted endovascular catheterization technologies: A review,” *Ann Biomed Eng*, 2014 (cit. on p. 93).
- [200] Ambrosini, P., Ruijters, D., Niessen, W. J., Moelker, A., and Walsum, T. van, “Fully automatic and real-time catheter segmentation in x-ray fluoroscopy,” in *International Conference on Medical Image Computing and Computer-Assisted Intervention (MICCAI)*, Springer, 2017, pp. 577–585 (cit. on pp. 93–95, 101, 116).

- [201] Barbu, A., Athitsos, V., Georgescu, B., Boehm, S., Durlak, P., and Comaniciu, D., “Hierarchical learning of curves application to guidewire localization in fluoroscopy,” in *Conference on Computer Vision and Pattern Recognition (CVPR)*, 2007 (cit. on pp. 94, 95).
- [202] Yi, X., Adams, S., Babyn, P., and Elnajmi, A., “Automatic catheter and tube detection in pediatric x-ray images using a scale-recurrent network and synthetic data,” *Journal of digital imaging*, vol. 33, pp. 181–190, 2020 (cit. on pp. 94, 95).
- [203] Mastmeyer, A., Pernelle, G., Barber, L., Pieper, S., Fortmeier, D., Wells, S., Handles, H., and Kapur, T., “Model-based catheter segmentation in mri-images,” *arXiv*, 2017 (cit. on pp. 94, 95).
- [204] Danilov, V. V., Kolpashchikov, D. Y., Gerget, O. M., Laptev, N. V., Proutski, A., Gómez, L. A. H., Alvarez, F., and Ledesma-Carbayo, M. J., “Use of semi-synthetic data for catheter segmentation improvement,” *Computerized Medical Imaging and Graphics*, 2023 (cit. on pp. 94, 95).
- [205] Ronneberger, O., Fischer, P., and Brox, T., “U-net: Convolutional networks for biomedical image segmentation,” in *International Conference on Medical Image Computing and Computer-Assisted Intervention (MICCAI)*, Springer, 2015, pp. 234–241 (cit. on pp. 94, 108, 110, 116, 134).
- [206] Delmas, C., Berger, M.-O., Kerrien, E., Riddell, C., Troussel, Y., Anxionnat, R., and Bracard, S., “Three-dimensional curvilinear device reconstruction from two fluoroscopic views,” in *Medical Imaging 2015: Image-Guided Procedures, Robotic Interventions, and Modeling*, Spie, vol. 9415, 2015, pp. 100–110 (cit. on pp. 95, 96).
- [207] Brost, A., Wimmer, A., Liao, R., Hornegger, J., and Strobel, N., “Catheter tracking: Filter-based vs. learning-based,” in *Joint Pattern Recognition Symposium*, 2010 (cit. on pp. 95, 101).
- [208] Petković, T., Homan, R., and Lončarić, S., “Real-time 3d position reconstruction of guidewire for monoplane x-ray,” *Comput Med Imaging Graph*, 2014 (cit. on p. 96).
- [209] Corporation, C., *Computer vision annotation tool (cvat)*, version 2.8.2, Nov. 6, 2023 (cit. on pp. 98, 125).
- [210] Brainerd, E. L., Baier, D. B., Gatesy, S. M., Hedrick, T. L., Metzger, K. A., Gilbert, S. L., and Crisco, J. J., “X-ray reconstruction of moving morphology (xromm): Precision, accuracy and applications in comparative biomechanics research,” *Journal of Experimental Zoology Part A: Ecological Genetics and Physiology*, 2010 (cit. on p. 99).
- [211] Verdonck, B., Bourel, P., Coste, E., Gerritsen, F. A., and Rousseau, J., “Variations in the geometrical distortion of x-ray image intensifiers,” in *Physics of Medical Imaging*, 1999 (cit. on p. 99).
- [212] Zhang, Z., “A flexible new technique for camera calibration,” *IEEE Trans. Pattern Anal. Mach. Intell.*, 2000 (cit. on p. 99).

- [213] Altingövde, O., Mishchuk, A., Ganeeva, G., Oveisi, E., Hebert, C., and Fua, P., “3d reconstruction of curvilinear structures with stereo matching deep convolutional neural networks,” *Ultramicroscopy*, vol. 234, p. 113 460, 2022 (cit. on p. 100).
- [214] Klema, V. and Laub, A., “The singular value decomposition: Its computation and some applications,” *IEEE Transactions on automatic control*, vol. 25, no. 2, pp. 164–176, 1980 (cit. on p. 101).
- [215] Subramanian, V., Wang, H., Wu, J. T., Wong, K. C., Sharma, A., and Syeda-Mahmood, T., “Automated detection and type classification of central venous catheters in chest x-rays,” in *International Conference on Medical Image Computing and Computer-Assisted Intervention (MICCAI)*, 2019 (cit. on p. 101).
- [216] Zhou, Y.-J., Xie, X.-L., Zhou, X.-H., Liu, S.-Q., Bian, G.-B., and Hou, Z.-G., “A real-time multifunctional framework for guidewire morphological and positional analysis in interventional x-ray fluoroscopy,” *Trans. Cogn. Develop. Syst.*, 2020 (cit. on p. 101).
- [217] Ambrosini, P., Small, I., Ruijters, D., Niessen, W. J., Moelker, A., and Walsum, T. van, “3d catheter tip tracking in 2d x-ray image sequences using a hidden markov model and 3d rotational angiography,” in *Augmented Environments for Computer-Assisted Interventions*, 2015 (cit. on p. 101).
- [218] Sitzmann, V., Thies, J., Heide, F., Nießner, M., Wetzstein, G., and Zollhofer, M., “Deepvoxels: Learning persistent 3d feature embeddings,” in *Proceedings of the IEEE/CVF Conference on Computer Vision and Pattern Recognition*, 2019, pp. 2437–2446 (cit. on p. 102).
- [219] Sutskever, I., Vinyals, O., and Le, Q. V., “Sequence to sequence learning with neural networks,” *Advances in neural information processing systems*, vol. 27, 2014 (cit. on p. 103).
- [220] Dozat, T., “Incorporating nesterov momentum into adam,” *ICLR (Workshop)*, 2016 (cit. on p. 105).
- [221] Nagi, J., Ducatelle, F., Di Caro, G. A., Cireşan, D., Meier, U., Giusti, A., Nagi, F., Schmidhuber, J., and Gambardella, L. M., “Max-pooling convolutional neural networks for vision-based hand gesture recognition,” in *2011 IEEE international conference on signal and image processing applications (ICSIPA)*, Ieee, 2011, pp. 342–347 (cit. on p. 105).
- [222] Srivastava, N., Hinton, G., Krizhevsky, A., Sutskever, I., and Salakhutdinov, R., “Dropout: A simple way to prevent neural networks from overfitting,” *The journal of machine learning research*, vol. 15, no. 1, pp. 1929–1958, 2014 (cit. on p. 105).
- [223] Dierckx, P., *Curve and surface fitting with splines*. Oxford University Press, 1995 (cit. on p. 106).
- [224] Chen, J., Lu, Y., Yu, Q., Luo, X., Adeli, E., Wang, Y., Lu, L., Yuille, A. L., and Zhou, Y., “Transunet: Transformers make strong encoders for medical image segmentation,” *arXiv*, 2021 (cit. on pp. 108, 110).

- [225] Cao, H., Wang, Y., Chen, J., Jiang, D., Zhang, X., Tian, Q., and Wang, M., “Swin-unet: Unet-like pure transformer for medical image segmentation,” in *European Conference on Computer Vision (ECCV)*, 2022 (cit. on pp. 108, 110, 111).
- [226] **Jianu, T.**, Doust, S., Li, M., Huang, B., Do, T., Nguyen, H., Bates, K., Ta, T. D., Fichera, S., Berthet-Rayne, P., *et al.*, “Splineformer: An explainable transformer-based approach for autonomous endovascular navigation,” in *International Conference on Intelligent Robots and Systems (IROS) - Under Review*, IEEE, 2025 (cit. on p. 113).
- [227] Lindgren, A., Vergouwen, M. D., Schaaf, I. van der, Algra, A., Wermer, M., Clarke, M. J., and Rinkel, G. J., “Endovascular coiling versus neurosurgical clipping for people with aneurysmal subarachnoid haemorrhage,” *Cochrane Database of Systematic Reviews*, no. 8, 2018 (cit. on p. 114).
- [228] McMeekin, P., White, P., James, M. A., Price, C. I., Flynn, D., and Ford, G. A., “Estimating the number of uk stroke patients eligible for endovascular thrombectomy,” *European stroke journal*, vol. 2, no. 4, pp. 319–326, 2017 (cit. on p. 114).
- [229] Berthet-Rayne, P. and Yang, G.-Z., “Navigation with minimal occupation volume for teleoperated snake-like surgical robots: Move,” *Frontiers in Robotics and AI*, vol. 10, 2023, ISSN: 2296-9144 (cit. on p. 114).
- [230] Fosch-Villaronga, E. and Mahler, T., “Cybersecurity, safety and robots: Strengthening the link between cybersecurity and safety in the context of care robots,” *Computer Law & Security Review*, vol. 41, p. 105 528, 2021, ISSN: 0267-3649 (cit. on p. 114).
- [231] Chi, W., Liu, J., Rafii-Tari, H., Riga, C., Bicknell, C., and Yang, G.-Z., “Learning-based endovascular navigation through the use of non-rigid registration for collaborative robotic catheterization,” *International Journal of Computer Assisted Radiology and Surgery (IJCARS)*, vol. 13, pp. 855–864, 2018 (cit. on pp. 115, 117).
- [232] Brost, A., Liao, R., Hornegger, J., and Strobel, N., “3-d respiratory motion compensation during ep procedures by image-based 3-d lasso catheter model generation and tracking,” in *International Conference on Medical Image Computing and Computer-Assisted Intervention (MICCAI)*, 2009 (cit. on p. 116).
- [233] Brost, A., Liao, R., Strobel, N., and Hornegger, J., “Respiratory motion compensation by model-based catheter tracking during ep procedures,” *Medical Image Analysis*, vol. 14, no. 5, pp. 695–706, 2010 (cit. on p. 116).
- [234] Baert, S. A., Viergever, M. A., and Niessen, W. J., “Guide-wire tracking during endovascular interventions,” *IEEE Transactions on Medical Imaging*, 2003 (cit. on p. 116).
- [235] Wu, W., Chen, T., Wang, P., Zhou, S. K., Comaniciu, D., Barbu, A., and Strobel, N., “Learning-based hypothesis fusion for robust catheter tracking in 2d x-ray fluoroscopy,” in *Conference on Computer Vision and Pattern Recognition (CVPR)*, IEEE, 2011, pp. 1097–1104 (cit. on p. 116).
- [236] Ma, Y., Gogin, N., Cathier, P., Housden, R. J., Gijsbers, G., Cooklin, M., O’Neill, M., Gill, J., Rinaldi, C. A., Razavi, R., *et al.*, “Real-time x-ray fluoroscopy-based catheter

- detection and tracking for cardiac electrophysiology interventions,” *Medical Physics*, vol. 40, no. 7, p. 071 902, 2013 (cit. on p. 116).
- [237] Sheng, C., Li, L., and Pei, W., “Automatic detection of supporting device positioning in intensive care unit radiography,” *The International Journal of Medical Robotics and Computer Assisted Surgery*, vol. 5, no. 3, pp. 332–340, 2009 (cit. on p. 116).
- [238] Kao, E.-F., Jaw, T.-S., Li, C.-W., Chou, M.-C., and Liu, G.-C., “Automated detection of endotracheal tubes in paediatric chest radiographs,” *Computer Methods and Programs in Biomedicine*, 2015 (cit. on p. 116).
- [239] Bismuth, V., Vaillant, R., Talbot, H., and Najman, L., “Curvilinear structure enhancement with the polygonal path image-application to guide-wire segmentation in x-ray fluoroscopy,” in *International Conference on Medical Image Computing and Computer-Assisted Intervention (MICCAI)*, Springer, 2012, pp. 9–16 (cit. on p. 116).
- [240] Wang, P., Chen, T., Zhu, Y., Zhang, W., Zhou, S. K., and Comaniciu, D., “Robust guidewire tracking in fluoroscopy,” in *2009 IEEE Conference on Computer Vision and Pattern Recognition*, IEEE, 2009, pp. 691–698 (cit. on p. 116).
- [241] Wang, L., Xie, X.-L., Bian, G.-B., Hou, Z.-G., Cheng, X.-R., and Prasong, P., “Guide-wire detection using region proposal network for x-ray image-guided navigation,” in *International Joint Conference on Neural Networks (IJCNN)*, 2017 (cit. on p. 116).
- [242] Yang, H., Shan, C., Kolen, A. F., and With Peter, H. de, “Improving catheter segmentation & localization in 3d cardiac ultrasound using direction-fused fcn,” in *International Symposium on Biomedical Imaging (ISBI)*, IEEE, 2019, pp. 1122–1126 (cit. on p. 116).
- [243] Zaffino, P., Pernelle, G., Mastmeyer, A., Mehrtash, A., Zhang, H., Kikinis, R., Kapur, T., and Spadea, M. F., “Fully automatic catheter segmentation in mri with 3d convolutional neural networks: Application to mri-guided gynecologic brachytherapy,” *Physics in Medicine & Biology*, vol. 64, no. 16, p. 165 008, 2019 (cit. on p. 116).
- [244] Yi, X., Adams, S., Babyn, P., and Elnajmi, A., “Automatic catheter and tube detection in pediatric x-ray images using a scale-recurrent network and synthetic data,” *Journal of Digital Imaging*, 2019 (cit. on p. 116).
- [245] Zhang, B., Bui, M., Wang, C., Bourier, F., Schunkert, H., and Navab, N., “Real-time guidewire tracking and segmentation in intraoperative x-ray,” in *Medical Imaging 2022: Image-Guided Procedures, Robotic Interventions, and Modeling*, SPIE, vol. 12034, 2022, pp. 283–290 (cit. on p. 116).
- [246] Song, Y., Li, L., Tian, Y., Li, Z., and Yin, X., “A novel Master-Slave interventional surgery robot with force feedback and collaborative operation,” en, *Sensors (Basel)*, vol. 23, no. 7, Mar. 2023 (cit. on p. 124).
- [247] Saliba, W., Cummings, J. E., Oh, S., Zhang, Y., Mazgalev, T. N., Schweikert, R. A., Burkhardt, J. D., and Natale, A., “Novel robotic catheter remote control system: Feasibility and safety of transseptal puncture and endocardial catheter navigation,” *Journal of cardiovascular electrophysiology*, vol. 17, no. 10, pp. 1102–1105, 2006 (cit. on p. 124).

- [248] Khan, E. M., Frumkin, W., Ng, G. A., Neelagaru, S., Abi-Samra, F. M., Lee, J., Giudici, M., Gohn, D., Winkle, R. A., Sussman, J., *et al.*, “First experience with a novel robotic remote catheter system: Amigo™ mapping trial,” *Journal of Interventional Cardiac Electrophysiology*, vol. 37, pp. 121–129, 2013 (cit. on p. 124).
- [249] Wei, X., Liu, M., Ling, Z., and Su, H., “Approximate convex decomposition for 3d meshes with collision-aware concavity and tree search,” *ACM Transactions on Graphics (TOG)*, vol. 41, no. 4, pp. 1–18, 2022 (cit. on p. 133).
- [250] Todorov, E., “Convex and analytically-invertible dynamics with contacts and constraints: Theory and implementation in mujoco,” in *International Conference on Robotics and Automation (ICRA)*, IEEE, 2014, pp. 6054–6061 (cit. on p. 133).
- [251] Yao, T., Xu, Y., Wang, H., Qiu, X., Althoefer, K., and Qi, P., “Multi-agent fuzzy reinforcement learning with llm for cooperative navigation of endovascular robotics,” *IEEE Transactions on Fuzzy Systems*, 2025 (cit. on p. 137).